UC San Diego

UC San Diego Electronic Theses and Dissertations

Title

Synthesis and Fabrication of High Entropy Diborides, Fluorite Oxides, and Silicides

Permalink

https://escholarship.org/uc/item/02n7v31m

Author

Gild, Joshua

Publication Date

2019

Peer reviewed|Thesis/dissertation

eScholarship.org Powered by the California Digital Library
University of California

UNIVERSITY OF CALIFORNIA SAN DIEGO

Synthesis and Fabrication of High Entropy Diborides, Fluorite Oxides, and Silicides

A dissertation submitted in partial satisfaction of the

Requirements for the degree

Doctor of Philosophy

in

Materials Science & Engineering

by

Joshua Gild

Committee in charge:

Professor Jian Luo, Chair
Professor Renkun Chen
Professor Javier Garay
Professor Olivia Graeve
Professor Kenneth Vecchio

2019

Copyright

Joshua Gild, 2019

All Rights Reserved

The Dissertation of Joshua Gild is approved, and it is acceptable in quality and form for publication on microfilm and electronically:

_____

_____

_____

_____

_____

Chair

University of California San Diego

2019

DEDICATION

This dissertation is dedicated to my family and friends who, without their years of support, would not be possible.

TABLE OF CONTENTS

Signature Page iii

Dedication iv

Table of Contents v

List of Figures viii

List of Tables xv

Acknowledgements xvi

Vita xix

Abstract of Dissertation xx

Chapter 1. Introduction 1

1.1 Motivation 1

1.2 Objective and Overview 5

Chapter 2. High-Entropy Metal Diborides: A New Class of High-Entropy Materials and a New Type of Ultrahigh Temperature Ceramics 7

2.1 Introduction 7

2.2 Results 8

2.2.1 Phase Evolution and Formation of High-Entropy Ceramic Phases 8

2.2.2 Compositional Uniformity 10

2.2.3 Atomic-Resolution Structural Characterization 10

2.2.4 Nanoscale Compositional Mapping 11

2.2.5 Densification and Lattice Parameters 12

2.2.6 Hardness and Oxidation Resistance 12

2.3 Discussion 14

2.4 Methods 18

2.4.1 Synthesis of High-Entropy Metal Diboride Specimens 18

2.4.2 Characterization 19

2.4.3 Hardness and Oxidation Measurements 20

Chapter 3. Reactive flash Spark Plasma Sintering of High-Entropy Ultrahigh Temperature Ceramics 51

3.1 Introduction 51

3.2 Materials and Methods 52

3.2.1 Synthesis of High-Entropy Diborides and Carbides 52

3.2.2 Characterization....54
3.3 Results and Discussion....54
3.3.1 Phase Evolution and Formation of High Entropy Phases....54
3.3.2 Densities of Sintered Specimens....56
3.3.3 Estimation of Temperature during Flash Spark Plasma Sintering....56
3.3.4 Electron Backscatter Diffraction....57
3.4 Conclusion....58
Chapter 4. Borocarbothermal Synthesis of High Entropy Metal Diborides....72
4.1 Introduction....73
4.2 Materials and Methods....73
4.2.1 Borocarbothermal Reduction of Metal Oxides....73
4.2.2 Characterization....75
4.3 Results and Discussion....76
4.3.1 Borocarbothermal Synthesis Power Morphology....76
4.3.2 Phase formation and compositional uniformity....76
4.3.3 Density and Lattice Parameters....77
4.3.4 Hardness Data....77
4.3.5 Electron Backscatter Diffraction....78
4.4 Conclusion....78
Chapter 5. High-Entropy Fluorite Oxides....90
5.1 Introduction....90
5.2 Synthesis and Fabrication....92
5.3 Characterization....93
5.3.1 Thermal Conductivity....94
5.3.2 Electrical Conductivity....95
5.3.3 Hardness....95
5.4 Results and Discussion....95
5.4.1 Phase Formation and Compositional Uniformity....95
5.4.2 Sintered Densities....97
5.4.3 Thermal Conductivity....97
5.4.4 Ionic Conductivity....98
5.4.5 Hardness....99

5.5 Conclusion 100
Chapter 6. A High-Entropy Silicide: ($Mo_{0.2}Nb_{0.2}Ta_{0.2}Ti_{0.2}W_{0.2}$)$Si_2$ 123
6.1 Introduction 123
6.2 Experimental Procedure 124
6.3 Results and Discussion 126
6.4 Conclusion 129
Chapter 7. Summary and Future Work 141
References 144

LIST OF FIGURES

Figure 2.1 Schematic illustration of the atomic structure of the high-entropy metal diborides ...22

Figure 2.2 XRD patterns showing the phase evolution during the HEBM and SPS fabrication processes in (a) HEB #2 as an exemplar in an expanded scale and (b) six other specimens 23

Figure 2.3 XRD patterns of all seven specimens after SPS at 2000 °C, where the peaks of the primary hexagonal phase are indexed 24

Figure 2.4 Cross-sectional SEM image and the corresponding EDX compositional maps of three selected specimens after SPS, showing the formation of largely homogeneous high-entropy solid-solution phases except for the HEB #6 shown in (c). 25

Figure 2.5 Atomic-resolution STEM ABF and HAADF images of HEB #2 $(Hf_{0.2}Zr_{0.2}Ta_{0.2}Mo_{0.2}Ti_{0.2})B_2$. 26

Figure 2.6 STEM-HAADF image and the corresponding EDS compositional maps for HEB #2 $(Hf_{0.2}Zr_{0.2}Ta_{0.2}Mo_{0.2}Ti_{0.2})B_2$, showing the homogeneous chemical distribution at nanoscale.....27

Figure 2.7 Measured hardness of six single-phase high-entropy metal diborides, which are generally greater than the "rule-of-mixtures" averages of the hardness values measured from individual metal diborides that were fabricated via the same HEBM and SPS route 28

Figure 2.8 A snapshot of the relative oxidation performance of various high-entropy and individual metal diborides fabricated and tested with the same conditions.....29

Figure 2.9 Specimen #1 $(Hf_{0.2}Zr_{0.2}Ta_{0.2}Nb_{0.2}Ti_{0.2})B_2$: **(a)** XRD patterns showing phase evolution during the HEBM-SPS fabrication process. **(b)** Cross-sectional SEM image and the corresponding EDX compositional maps of the specimen after SPS 30

Figure 2.10 Specimen #2 $(Hf_{0.2}Zr_{0.2}Ta_{0.2}Mo_{0.2}Ti_{0.2})B_2$: **(a)** XRD patterns showing phase evolution during the HEBM-SPS fabrication process. **(b)** Cross-sectional SEM image and the corresponding EDX compositional maps of the specimen after SPS 31

Figure 2.11 Specimen #3 $(Hf_{0.2}Zr_{0.2}Mo_{0.2}Nb_{0.2}Ti_{0.2})B_2$: **(a)** XRD patterns showing phase evolution during the HEBM-SPS fabrication process. **(b)** Cross-sectional SEM image and the corresponding EDX compositional maps of the specimen after SPS. 32

Figure 2.12 Specimen #4 $(Hf_{0.2}Mo_{0.2}Ta_{0.2}Nb_{0.2}Ti_{0.2})B_2$: **(a)** XRD patterns showing phase evolution during the HEBM-SPS fabrication process. **(b)** Cross-sectional SEM image and the corresponding EDX compositional maps of the specimen after SPS 33

Figure 2.13 Specimen #5 $(Mo_{0.2}Hf_{0.2}Ta_{0.2}Nb_{0.2}Ti_{0.2})B_2$: **(a)** XRD patterns showing phase evolution during the HEBM-SPS fabrication process. **(b)** Cross-sectional SEM image and the corresponding EDX compositional maps of the specimen after SPS 34

Figure 2.14 Specimen #6 $(Zr_{0.2}Hf_{0.2}W_{0.2}Mo_{0.2}Ti_{0.2})B_2$: **(a)** XRD patterns showing phase evolution during the HEBM-SPS fabrication process. **(b)** Cross-sectional SEM image and the corresponding EDX compositional maps of the specimen after SPS 35

Figure 2.15 Specimen #7 $(Zr_{0.2}Hf_{0.2}Ta_{0.2}Cr_{0.2}Ti_{0.2})B_2$: **(a)** XRD patterns showing phase evolution during the HEBM-SPS fabrication process. **(b)** Cross-sectional SEM image and the corresponding EDX compositional maps of the specimen after SPS 36

Figure 2.16 STEM images at three different magnifications for Specimen #2 $(Hf_{0.2}Zr_{0.2}Ta_{0.2}Mo_{0.2}Ti_{0.2})B_2$ at a different location in the same specimen shown in Fig. 5. **(a)**, **(d)** and **(g)** are STEM-ABF images; **(b)**, **(e)** and **(h)** are STEM-HAADF images; **(c)**, **(f)** and **(i)** are STEM-MAADF images 37

Figure 2.17 STEM images at three different magnifications for Specimen #2 $(Hf_{0.2}Zr_{0.2}Ta_{0.2}Mo_{0.2}Ti_{0.2})B_2$ from a different grain in the same specimen shown in Fig. 5. **(a)**, **(d)** and **(g)** are STEM-ABF images; **(b)**, **(e)** and **(h)** are STEM-HAADF images; **(c)**, **(f)** and **(i)** are STEM-MAADF images 38

Figure 2.18 STEM images at three different magnifications for Specimen #1 $(Hf_{0.2}Zr_{0.2}Ta_{0.2}Nb_{0.2}Ti_{0.2})B_2$. **(a)**, **(d)** and **(g)** are STEM-ABF images; **(b)**, **(e)** and **(h)** are STEM-HAADF images; **(c)**, **(f)** and **(i)** are STEM-MAADF images 39

Figure 2.19 Digital analysis of the STEM ADF and HAADF images from Specimen #2 $(Hf_{0.2}Zr_{0.2}Ta_{0.2}Mo_{0.2}Ti_{0.2})B_2$, showing a narrow distribution of measured basal (0001) lattice spacings that is only ~0.6% of the mean, *i.e.*, a standard variation of ~0.02 Å 40

Figure 2.20 Nanoscale EDX compositional maps for Specimen #2 $(Hf_{0.2}Zr_{0.2}Ta_{0.2}Mo_{0.2}Ti_{0.2})B_2$ from a different location in the same specimen shown in Fig. 6, showing the homogeneous chemical distribution at nanoscale 41

Figure 2.21 (a) Weight gain per surface area and **(b)** percentage weight gain vs. oxidation temperature curves during isothermal oxidation experiments in flowing dry air at 1000°C, 1100°C, and 1200 °C (for one hour each) sequentially for six single-phase high-entropy metal diborides.....42

Figure 2.22 Optical images showing the changes of the specimen appearance during a sequential oxidation experiments at 800-1500°C for HEB #1 ($Hf_{0.2}Zr_{0.2}Ti_{0.2}Nb_{0.2}Ta_{0.2})B_2$ and HEB #7 ($Hf_{0.2}Zr_{0.2}Ti_{0.2}Cr_{0.2}Ta_{0.2})B_2$), along with six individual metal diborides that were fabricated via the same HEBM and SPS route. 43

Figure 2.23 Optical images showing the changes of the specimen appearance during a sequential oxidation experiments at 800-1500°C for four MoB_2-containing high-entropy diborides, which exhibited interesting, yet different, oxidation behaviors. Noting that MoO_3 is volatile in this temperature range.....44

Figure 3.1 Powder XRD of three ($Hf_{0.2}Zr_{0.2}Ta_{0.2}Nb_{0.2}Ti_{0.2})B_2$ specimens (Samples B1, B2, and B3) and one ($Hf_{0.2}Zr_{0.2}Ta_{0.2}Nb_{0.2}Ti_{0.2}$)C specimen (Sample C1) made by ReaFSPS 60

Figure 3.2 SEM micrograph of sintered ($Hf_{0.2}Zr_{0.2}Ta_{0.2}Nb_{0.2}Ti_{0.2})B_2$ (a) Sample B1 (no C, 100% power), (b) Sample B2 (3 wt. % C, 100% power), and (c) Sample B3 (3 wt. % C, 30% power), as well as (d) ($Hf_{0.2}Zr_{0.2}Ta_{0.2}Nb_{0.2}Ti_{0.2}$)C Sample C1 (1 wt. % C, 30% power).....61

Figure 3.3 SEM micrographs and EDX elemental maps of (a) Sample B3, ($Hf_{0.2}Zr_{0.2}Ta_{0.2}Nb_{0.2}Ti_{0.2})B_2$, and (b) Sample C1, ($Hf_{0.2}Zr_{0.2}Ta_{0.2}Nb_{0.2}Ti_{0.2}$)C, fabricated by ReaFSPS 62

Figure 3.4 EBSD maps of (a) Sample B2, (b) Sample B3, and (c) Sample C1, and (d) grain size distributions for all three single-phase specimens 63

Figure 3.5 Position and current output curves with respect to time during the ReaFSPS of (a) Sample B1, (b) Sample B2, (c) Sample B3, and (d) Sample C1 64

Figure 3.6 $Hf_{0.2}Zr_{0.2}Ta_{0.2}Nb_{0.2}Ti_{0.2})B_2$ + 3 wt. % C specimens fabricated by ReaFSPS using (a) 100% power (Sample B2) (b) 30% power (Sample B3). The darker outside edges indicate high reactivity and melting at high processing temperatures.....65

Figure 3.7 Powder XRD of milled diboride powder, the presintered sample (at 1600˚C for 5 min), and $(Hf_{0.2}Zr_{0.2}Ta_{0.2}Nb_{0.2}Ti_{0.2})B_2$ specimen fabricated by ReaFSPS using 30% power 66

Figure 3.8 Powder XRD of milled carbide powder, the presintered sample (at 1400˚C for 5 min), and $(Hf_{0.2}Zr_{0.2}Ta_{0.2}Nb_{0.2}Ti_{0.2})C$ specimen fabricated by ReaFSPS using 30% power 67

Figure 4.1 (a) XRD of $(Hf_{0.2}Zr_{0.2}Ti_{0.2}Ta_{0.2}Nb_{0.2})B_2$ powder, showing multiple phases and (b) SEM image of diboride powder post synthesis.....80

Figure 4.2 XRD patterns of the four high entropy diboride specimens with three, $(Hf_{0.2}Zr_{0.2}Ti_{0.2}Ta_{0.2}Nb_{0.2})B_2$, $(Hf_{0.2}Zr_{0.2}Ti_{0.2}Ta_{0.2}Mo_{0.2})B_2$, and $(Hf_{0.2}Zr_{0.2}Ti_{0.2}Ta_{0.2}Cr_{0.2})B_2$ showing a single phase. $(Hf_{0.2}Zr_{0.2}Ti_{0.2}Mo_{0.2}W_{0.2})B_2$ shows a minor $(Mo,Ti,W)B_4$ secondary phase. 81

Figure 4.3 Cross-section SEM images and the corresponding EDS composition maps of the single phase diborides, (a) $(Hf_{0.2}Zr_{0.2}Ti_{0.2}Ta_{0.2}Nb_{0.2})B_2$, (b) $(Hf_{0.2}Zr_{0.2}Ti_{0.2}Ta_{0.2}Mo_{0.2})B_2$, (c) $(Hf_{0.2}Zr_{0.2}Ti_{0.2}Ta_{0.2}Cr_{0.2})B_2$ 82

Figure 4.4 Point EDS $(Hf_{0.2}Zr_{0.2}Ti_{0.2}Mo_{0.2}W_{0.2})B_2$ showing a tungsten-molybdenum rich secondary phase, confirmed to be a tetraboride structure of the CrB type via XRD. The iridium values are due to the conductive coating on the sample 83

Figure 4.5 EBSD maps of (a) $(Hf_{0.2}Zr_{0.2}Ti_{0.2}Ta_{0.2}Nb_{0.2})B_2$, (b) $(Hf_{0.2}Zr_{0.2}Ti_{0.2}Ta_{0.2}Mo_{0.2})B_2$, (c) $(Hf_{0.2}Zr_{0.2}Ti_{0.2}Ta_{0.2}Cr_{0.2})B_2$, and (d) the probability distributions of each composition with respect to grain size.....84

Figure 5.1 XRD patterns of HEFO1: $(Hf_{0.25}Zr_{0.25}Ce_{0.25}Y_{0.25})O_{2-\delta}$, HEFO4A: $(Hf_{0.25}Zr_{0.25}Ce_{0.25})(Y_{0.125}Yb_{0.125})O_{2-\delta}$, HEFO4B: $(Hf_{0.2}Zr_{0.2}Ce_{0.2})(Y_{0.2}Yb_{0.2})O_{2-\delta}$, HEFO5A: $(Hf_{0.25}Zr_{0.25}Ce_{0.25})(Y_{0.125}Ca_{0.125})O_{2-\delta}$, HEFO7A: $(Hf_{0.25}Zr_{0.25}Ce_{0.25})(Y_{0.125}Gd_{0.125})O_{2-\delta}$, HEFO7B: $(Hf_{0.2}Zr_{0.2}Ce_{0.2})(Y_{0.2}Gd_{0.2})O_{2-\delta}$, HEFO8A: $(Hf_{0.25}Zr_{0.25}Ce_{0.25})(Yb_{0.125}Gd_{0.125})O_{2-\delta}$ 101

Figure 5.2 XRD patterns of HEFO2A: $(Hf_{0.25}Zr_{0.25}Ce_{0.25})(Y_{0.125}Ti_{0.125})O_{2-\delta}$, HEFO3A: $(Hf_{0.25}Zr_{0.25}Ce_{0.25})(Y_{0.125}Mg_{0.125})O_{2-\delta}$, HEFO5B: $(Hf_{0.2}Zr_{0.2}Ce_{0.2})(Y_{0.2}Ca_{0.2})O_{2-\delta}$, HEFO6A: $(Hf_{0.25}Zr_{0.25}Ce_{0.25})(Y_{0.125}La_{0.125})O_{2-\delta}$, all of which possess secondary phases. In all four cases, the primary phases are still solid-solution phases of the fluorite structure.....102

Figure 5.3 Cross-sectional SEM images and the corresponding EDS compositional maps of three selected specimens.....103

Figure 5.4 Thermal conductivities of the eight single-phase HEFOs, along with 8YSZ, measured by TDTR 104

Figure 5.5 Arrhenius plots of measured conductivities for five single-phase HEFO, along with 8YSZ, from 650˚C to 850˚C (measured in zero grade dry air).....105

Figure 5.6 Grain size distributions of HEFO4B: $(Hf_{0.2}Zr_{0.2}Ce_{0.2})(Y_{0.2}Yb_{0.2})O_{2-\delta}$ and 8YSZ. Both specimens were fabricated by the identical process of SPS and subsequent 1500˚C annealing in air 106

Figure 5.7 Measured hardness of eight single-phase HEFO along with 8YSZ, Y_2O_3 and Yb_2O_3 for comparison 107

Figure 5.8 HEFO1: $(Hf_{0.25}Zr_{0.25}Ce_{0.25})(Y_{0.25})O_{2-\delta}$: **(a)** XRD patterns showing phase evolution during the HEBM-SPS fabrication process. **(b)** Cross-sectional SEM image and the corresponding EDX compositional maps of the specimen after SPS 108

Figure 5.9 HEFO4A: $(Hf_{0.25}Zr_{0.25}Ce_{0.25})(Y_{0.125}Yb_{0.125})O_{2-\delta}$: **(a)** XRD patterns showing phase evolution during the HEBM-SPS fabrication process. **(b)** Cross-sectional SEM image and the corresponding EDX compositional maps of the specimen after SPS 109

Figure 5.10 HEFO4B: $(Hf_{0.2}Zr_{0.2}Ce_{0.2})(Y_{0.2}Yb_{0.2})O_{2-\delta}$: **(a)** XRD patterns showing phase evolution during the HEBM-SPS fabrication process. **(b)** Cross-sectional SEM image and the corresponding EDX compositional maps of the specimen after SPS 110

Figure 5.11 HEFO5A: $(Hf_{0.25}Zr_{0.25}Ce_{0.25})(Y_{0.125}Ca_{0.125})O_{2-\delta}$: **(a)** XRD patterns showing phase evolution during the HEBM-SPS fabrication process. **(b)** Cross-sectional SEM image and the corresponding EDX compositional maps of the specimen after SPS 111

Figure 5.12 HEFO7A: $(Hf_{0.25}Zr_{0.25}Ce_{0.25})(Y_{0.125}Gd_{0.125})O_{2-\delta}$: **(a)** XRD patterns showing phase evolution during the HEBM-SPS fabrication process. **(b)** Cross-sectional SEM image and the corresponding EDX compositional maps of the specimen after SPS 112

Figure 5.13 HEFO7B: $(Hf_{0.2}Zr_{0.2}Ce_{0.2})(Y_{0.2}Gd_{0.2})O_{2-\delta}$: **(a)** XRD patterns showing phase evolution during the HEBM-SPS fabrication process. **(b)** Cross-sectional SEM image and the corresponding EDX compositional maps of the specimen after SPS 113

Figure 5.14 HEFO8A: $(Hf_{0.25}Zr_{0.25}Ce_{0.25})(Yb_{0.125}Gd_{0.125})O_{2-\delta}$: **(a)** XRD patterns showing phase evolution during the HEBM-SPS fabrication process. **(b)** Cross-sectional SEM image and the corresponding EDX compositional maps of the specimen after SPS 114

Figure 5.15 HEFO8B: $(Hf_{0.2}Zr_{0.2}Ce_{0.2})(Yb_{0.2}Gd_{0.2})O_{2-\delta}$: **(a)** XRD patterns showing phase evolution during the HEBM-SPS fabrication process. **(b)** Cross-sectional SEM image and the corresponding EDX compositional maps of the specimen after SPS 115

Figure 5.16 HEFO2A: $(Hf_{0.25}Zr_{0.25}Ce_{0.25})(Y_{0.125}Ti_{0.125})O_{2-\delta}$: **(a)** XRD patterns showing phase evolution during the HEBM-SPS fabrication process. **(b)** Cross-sectional SEM image and the corresponding EDX compositional maps of the specimen after SPS 116

Figure 5.17 HEFO3A: $(Hf_{0.25}Zr_{0.25}Ce_{0.25})(Y_{0.125}Mg_{0.125})O_{2-\delta}$: **(a)** XRD patterns showing phase evolution during the HEBM-SPS fabrication process. **(b)** Cross-sectional SEM image and the corresponding EDX compositional maps of the specimen after SPS 117

Figure 5.18 HEFO5B: $(Hf_{0.2}Zr_{0.2}Ce_{0.2})(Y_{0.2}Ca_{0.2})O_{2-\delta}$: **(a)** XRD patterns showing phase evolution during the HEBM-SPS fabrication process. **(b)** Cross-sectional SEM image and the corresponding EDX compositional maps of the specimen after SPS 118

Figure 5.19 HEFO6A: $(Hf_{0.25}Zr_{0.25}Ce_{0.25})(Y_{0.125}La_{0.125})O_{2-\delta}$: **(a)** XRD patterns showing phase evolution during the HEBM-SPS fabrication process. **(b)** Cross-sectional SEM image and the corresponding EDX compositional maps of the specimen after SPS 119

Figure 6.1 Schematic illustration of the atomic structure of the hexagonal high-entropy disilicide with the ABC stacking sequences (*i.e.* the $CrSi_2$ prototype structure) 131

Figure 6.2 XRD pattern of the $(Mo_{0.2}Nb_{0.2}Ta_{0.2}Ti_{0.2}W_{0.2})Si_2$ specimen. Except one minor peak from a secondary hexagonal TiO phase (labeled by the red solid square), all other XRD peaks are indexed to a hexagonal C40 structure (or the $CrSi_2$ prototype structure with the $P6_{222}$ space group and the D_6 point group) with the lattice parameters a = 4.711 Å and c = 6.522 Å.....132

Figure 6.3 SEM micrograph and the corresponding EDX elemental maps of the $(Mo_{0.2}Nb_{0.2}Ta_{0.2}Ti_{0.2}W_{0.2})Si_2$ specimen 133

Figure 6.4 EBSD map of >1 mm^2 area of the high-entropy $(Mo_{0.2}Nb_{0.2}Ta_{0.2}Ti_{0.2}W_{0.2})Si_2$ surface, showing a rather uniform microstructure. No significant texture was observed. The measured grain size distribution is given, which fits a lognormal curve. The inset on the right-bottom corner is an additional EBSD map taken at a higher magnification 134

Figure 6.5 XRD pattern, SEM micrograph, and the corresponding EDX elemental maps of the $(Mo_{0.2}Nb_{0.2}Ta_{0.2}W_{0.2}Zr_{0.2})Si_2$ specimen. In addition to a primary hexagonal C40 phase, Ta-Zr-Si and Nb-Zr-Si rich secondary phases were observed.....135

LIST OF TABLES

Table 2.1 Summary of the seven metal diboride systems studied. For the lattice parameters (*a* and *c*), the "average" values represent the means of five individual metal diborides while the "XRD" values represent the actual lattice parameters of the high-entropy solutions measured by XRD. See Supplementary Table S-I for additional data. 45

Table 2.2 Summary of key parameters and measured results of the seven high-entropy metal diboride systems studied 46

Table 2.3 Summary of lattice parameters of the corresponding individual metal diborides (MB_2) as well as metallic (12-coordinate and at or near ambient temperatures) and covalent radii of different elements 47

Table 2.4 Summary of hardness measurements of six single-phase high-entropy metal diborides, along with six individual metal diborides that were fabricated via the same HEBM and SPS route 48

Table 3.1 Summary of the nominal composition, ReaFSPS heating scheme, and the sintering aid used for each sample. 68

Table 4.1 All High Entropy Diborides (HEBs) fabricated, along with lattice parameters, densities, thermal conductivities, Vicker's hardness, and excess boron carbide needed for single phase samples 85

Table 5.1 All High Entropy Fluorite Oxides (HEFOs) fabricated, along with lattice parameters, densities, thermal conductivities, and Vicker's hardness values 120

Table 6.1 Comparison of the properties of the high-entropy $(Mo_{0.2}Nb_{0.2}Ta_{0.2}Ti_{0.2}W_{0.2})Si_2$ with five individual constituent metal disilicides 136

ACKNOWLEDGEMENTS

I would, first and foremost, like to acknowledge the support and mentorship of my advisor, Dr. Jian Luo. It has been an honor to work with him for these years. I would like to thank Dr. Kenneth Vecchio for his guidance and access to his lab and resources which proved vital for my research. I am grateful for the advice and assistance from my other committee members, Dr. Olivia Graeve, Dr. Javier Garay, and Dr. Renkun Chen.

I would like to thank all my collaborators at UCSD, Dr. Tyler Harrington, Dr. Mojtaba Samiee, Dr. Yuanyao Zhang, Kevin Kauffman, Heidy Vega, Mingde Qin, Andrew Wright, Sicong Jiang, Dr. Tao Hu, Matthew Quinn, William Mellor, Dr. Naixie Zhou, Blake Bloomfield, Daniel Martinez, and Dr. Kenneth Vecchio. Additionally, I would like to thank the rest of the lab members of the Luo and Vecchio group for their thoughtful discussion and assistance.

I am thankful to my collaborators at the University of Virginia for their work in characterization of the materials as well as insight into fabrication of the materials. In particular, Dr. Jeffrey Braun, Lavina Backman, Kathleen Tomko, Dr. Patrick Hopkins, and Dr. Elizabeth Opila for their work within our MURI program. I would like to acknowledge the other members of the MURI program: Samuel Daigle, Mina Lim, and Dr. Donald Brenner at North Carolina State University; Dr. Cormac Toher, Dr. Pranab Sarker, Dr. Stefano Curtarolo at Duke University; Trent Borman and Dr. John-Paul Maria at Pennsylvania State Univeristy and the program managers Dr. Eric Wuchina and Dr. Kenny Lipkowitz for their invaluable guidance and assistance during my studies. I would like to acknowledge the financial support from the Office of Naval Research MURI program, grant no. N00014-15-1-2863.

Last, but not least, I would like to thank my parents, siblings, and loved ones for their endless support through my years of studies.

Chapter 2, in full, is a reprint of the material “High-Entropy Metal Diborides: A New Class of High-Entropy Materials and a New Type of Ultrahigh Temperature Ceramics” as it appears in *Scientific Reports*, J. Gild, Y. Zhang, T. Harrington, S. Jiang, T. Hu, M.C. Quinn, W.M. Mellor, N. Zhou, K. Vecchio, J. Luo, Scientific Reports 6 (2016) 37946. The dissertation author was the primary investigator and wrote the first draft of manuscript.

Chapter 3, in part, is a reprint of the material “Reactive flash spark plasma sintering of high-entropy ultrahigh temperature ceramics” as it appears in *Scripta Materialia*. J. Gild, K. Kaufmann, K. Vecchio, J. Luo, Reactive flash spark plasma sintering of high-entropy ultrahigh temperature ceramics, Scripta Materialia. 170 (2019) 106–110. The dissertation author was the primary investigator and wrote the first draft of manuscript.

Chapter 4, in full, is currently in preparation for submission for publication “Borocarbothermal Synthesis of High Entropy Metal Diborides”, J. Gild, A. Wright, K. Tomko, M. Qin, B. Bloomfield, D. Martinez, T. Harrington, K. Vecchio, P. Hopkins, J. Luo. The dissertation author was the primary investigator and wrote the first draft of manuscript.

Chapter 5, in part, is a reprint of the material “High-Entropy Fluorite Oxides” as it appears in *Journal of the European Ceramic Society*, J. Gild, M. Samiee, J.L. Braun, T. Harrington, H. Vega, P.E. Hopkins, K. Vecchio, J. Luo, Journal of the European Ceramic Society. 38 (2018) 3578–3584. The dissertation author was the primary investigator and wrote the first draft of manuscript.

Chapter 6, in full, is a reprint of the material “A high-entropy silicide: $(Mo_{0.2}Nb_{0.2}Ta_{0.2}Ti_{0.2}W_{0.2})Si_2$” as it appears in *Journal of Materiomics*, J. Gild, J. Braun, K. Kaufmann, E. Marin, T. Harrington, P. Hopkins, K. Vecchio, J. Luo, Journal of Materiomics. (2019). The dissertation author was the primary investigator and wrote the first draft of manuscript.

VITA

2012 Bachelor of Science, Physics, Boston College

2015 Masters of Science, Materials Science & Engineering, Rochester Institute of Technology

2019 Doctor of Philosophy, Materials Science & Engineering, University of California San Diego

Publications

J. Gild, Y. Zhang, T. Harrington, S. Jiang, T. Hu, M.C. Quinn, W.M. Mellor, N. Zhou, K. Vecchio, J. Luo, High-Entropy Metal Diborides: A New Class of High-Entropy Materials and a New Type of Ultrahigh Temperature Ceramics, Scientific Reports. 6 (2016) 37946. doi:10.1038/srep37946.

S. Jiang, T. Hu, **J. Gild**, N. Zhou, J. Nie, M. Qin, T. Harrington, K. Vecchio, J. Luo, A new class of high-entropy perovskite oxides, Scripta Materialia. 142 (2017) 116–120. doi:10.1016/j.scriptamat.2017.08.040.

J. Gild, M. Samiee, J.L. Braun, T. Harrington, H. Vega, P.E. Hopkins, K. Vecchio, J. Luo, High-entropy fluorite oxides, Journal of the European Ceramic Society. 38 (2018) 3578–3584. doi:10.1016/j.jeurceramsoc.2018.04.010.

T.J. Harrington, **J. Gild**, P. Sarker, C. Toher, C.M. Rost, O.F. Dippo, C. McElfresh, K. Kaufmann, E. Marin, L. Borowski, P.E. Hopkins, J. Luo, S. Curtarolo, D.W. Brenner, K.S. Vecchio, Phase stability and mechanical properties of novel high entropy transition metal carbides, Acta Materialia. 166 (2019) 271–280. doi:10.1016/j.actamat.2018.12.054.

J. Gild, K. Kaufmann, K. Vecchio, J. Luo, Reactive flash spark plasma sintering of high-entropy ultrahigh temperature ceramics, Scripta Materialia. 170 (2019) 106–110. doi:10.1016/j.scriptamat.2019.05.039.

J. Gild, J. Braun, K. Kaufmann, E. Marin, T. Harrington, P. Hopkins, K. Vecchio, J. Luo, A high-entropy silicide: $(Mo_{0.2}Nb_{0.2}Ta_{0.2}Ti_{0.2}W_{0.2})Si_2$, Journal of Materiomics. (2019). doi:10.1016/j.jmat.2019.03.002.

J. Gild, A. Wright, K. Tomko, M. Qin, B. Bloomfield, D. Martinez, T. Harrington, K. Vecchio, P. Hopkins, J. Luo, Borocarbothermal Synthesis of High Entropy Metal Diborides, In preparation.

ABSTRACT OF DISSERTATION

Synthesis and Fabrication of High Entropy Diborides, Fluorite Oxides, and Silicides

By

Joshua Gild

Doctor of Philosophy in Materials Science & Engineering

University of California San Diego, 2019

Professor Jian Luo, Chair

Since their inception in 2004, high entropy alloys have become a new area of intense research in the metallurgical community. Over five hundred distinct compositions have been examined and they have proven to have unique and promising characteristics in the mechanical, thermal, and chemical fields. The field of high entropy ceramics, however, only began in 2016 and is still a fledgling field of research. Here, the bulk synthesis and fabrication of high entropy

diborides, carbides, fluorite oxides, and silicides is examined. In the first part of the dissertation, the fabrication of high entropy diborides from commercial powder via high energy ball milling and subsequent spark plasma sintering is investigated. The materials are found to have superior hardness and oxidation resistance to the majority of binary diborides. In the second section, flash spark plasma sintering is utilized to fabricate high entropy diboride and high entropy carbide composites with graphite in 90 seconds. The presence of graphite was found to be necessary for the homogenization of the diborides even at very high temperatures. In the third section, the direct synthesis of high entropy diborides via borocarbothermal reduction of metal oxides and spark plasma sintering; this successfully created fully dense, homogenous materials. In the fourth part, the production of high entropy fluorite oxides based off the yttria-stabilized zirconia (YSZ) structure is performed. These materials were found to have significantly reduced thermal and ionic conductivities compared to 8YSZ, a commonly used fluorite oxide material. In the final part, a high entropy silicide is fabricated via milling and spark plasma sintering. It was found to have a thermal conductivity of approximately one third that of similar disilcides. The production of a wide swath of materials allowed for similar characteristics to be found amongst the materials. In particular, significant reductions in thermal conductivity and improvements in hardness (both Vickers and nanoindentation) appear to be uniform properties among all the high entropy ceramics, similar to what is observed in the metallurgical field. The discovery of these materials opens up a wide new range of compositional space for refractory and rare earth ceramics.

Chapter 1. Introduction

1.1 Motivation

There are ever increasing demands upon materials of all kind and lengths scales in today's modern age. In particular, there is a strong desire to fabricate new structural materials for extreme high temperature environments as seen in hypersonic and aerospace applications. Significant interest is being paid to optimizing the composition and microstructure of these materials to optimize performance.

Traditionally, materials have been based off one or two bulk base components with the addition of secondary elements to optimize performance in one or more areas - be it corrosion resistance, mechanical properties, melting point, electrical and magnetic properties, or other areas. While there is still a great deal of research to be done on these materials and their importance cannot be overstated, there is a more recent trend to expand compositional space into more complex areas. The development of chemically complex materials, commonly referred to as "high entropy" materials, is a rapidly developing new field in both metallurgy and ceramic engineering.

High-entropy alloys (HEAs), also known as complex concentrated alloys (CCAs) or multi-principal element alloys, typically consist of five or more principal elements in amounts ranging from 5 to 35 at. %. [1,2] The configurational entropy can reach a significant amount once five or more principal components are present in the system; it reaches a maximum value of $\Delta S_{mix} = RlnN$ per mole for a N-component system, where R is the gas constant, for an equimolar composition. The first high entropy alloys were introduced by Cantor et al. in 2004 with the production of $Fe_{20}Cr_{20}Mn_{20}Ni_{20}Co_{20}$ based alloys that are stabilized into a single FCC phase. [3] Since their introduction, a large number of new high entropy alloys have been developed and

their properties studied extensively. The majority of HEAs so far consist of the five elements in the Cantor alloy along with Al, V, Ti, and Cu due to their similarities with traditional steels as well as aluminum alloys due to their low densities. Additionally, significant work is being performed in refractory compositionally complex alloys (RCCAs) consisting of Group IV, V, and VI elements. There is also limited research into rare earth, alkali earth metal, or precious metal containing high entropy alloys. [1,4–7]

In general, the materials have been observed to have lowered thermal conductivity and increased hardness when compared to their constituent elements. [1,8] A variety of alloys have shown high compressive strength values at both room and elevated temperatures, showing promise as new structural materials. [9–11] In 2017, Miracle and Senkov gave an extensive review of the main principles and predominant properties of high entropy materials, with emphasis being given to four different aspects: [1]

- "The high entropy effect" - the increased configurational entropy of five or more components will help stabilize a solid solution over the presence of intermetallics or other complex phases. This argument has been used to suggest increased stability at higher temperatures as entropy linearly increases with temperature.
- "The lattice distortion effect" - the relatively large mismatch between atomic sizes of the principle components could increase the distortion of the lattice beyond that of conventional alloys. This is sometimes used as the rationale for increased hardness and reduced thermal conductivities of the materials, among other effects.
- "The sluggish diffusion effect" - diffusion is suggested to be slow in high entropy alloys due to the formation of nanocrystals and amorphous phases upon cooling.

- "The cocktail effect" - a qualitative argument that the end material can be significantly different or more useful than any of its constituents. This point is the same as the one made for bulk metallic glasses that have unique and interesting properties not seen in the constituent materials.

Furthermore, since the entropy scales with increased temperature, it has been argued that the formation of a single phase becomes more probable as temperature increases and that the overall melting temperature may scale as well. [1] The study of both the formation and the properties of these high entropy materials is critical for the development of new materials for high temperature applications.

In 2015, Rost et al. expanded the high entropy compositional space to the ceramic field with the fabrication of a $(Mg_{0.2}Co_{0.2}Ni_{0.2}Cu_{0.2}Zn_{0.2})O$ rocksalt oxide. [12] Notably, the oxide possesses a transformable phase structure from single phase FCC to multiple constituent phases when quenched in air from different temperatures, giving credence to the argument for enhanced entropic stability at high temperatures. Since its fabrication, this composition and its derivatives are observed to have colossal dielectric constants and lithium superionic conductivity when doped with Ga and Li. [13–15]

With the introduction of high entropy materials into the ceramics field, there was interest in the properties and stability of a wide variety of ceramic materials. This includes ceramics for a wide variety of applications – varying from structural to structural based purposes to high temperature, functional, or electronic purposes. For bulk ultra-high temperature ceramics (UHTCs), refractory diborides are of interest as some possess melting temperatures above 3000˚C and, perhaps even more importantly, have high thermal conductivities and retain good mechanical properties at higher temperatures. [16,17] This is critical for aerospace applications,

as poor thermal shock properties will lead to cracking of the ceramic layers, leading to poor oxidative and mechanical properties. Pure refractory diborides are notoriously difficult to sinter, however, requiring very fine particle size as well as low oxygen content to be sintered in a pure form. [18,19] The current state of the art UHTCs are ZrB_2 based ceramic composites with silicon carbide (SiC) and other additions to enhance mechanical properties as well as improve oxidation resistance in air at high temperatures. The SiC acts as a sintering aid as well, allowing for high densification of the material despite higher oxygen content. Similarly, refractory silicides and boron carbide are used as sintering aids for densification of the material. [16,20–25] To avoid the utilization of sintering aids, direct powder synthesis of the diborides is needed or more exotic methods of densification. Powder synthesis from refractory oxides or metal powders are both commonplace in literature as methods for making high quality powder for later densification. [26–32] Refractory diboride are prime candidates for exploring the enhanced properties of high entropy ceramics.

Refractory oxides, similar to yttria stabilized zirconia, are of interest for the protection of materials at high temperatures. Fluorite oxides consisting of hafnia and zirconia as well as rare earth oxides possess a high melting temperature, phase stability in a wide temperature range, low thermal conductivity, and a wide range of ionic conductivity. YSZ type oxides have been explored for their potential as thermal barrier coatings at high temperature where the stability of high entropy materials should be elevated. [33–35] There is great interest in new materials for solid oxide fuel cells (SOFCs) at a variety of temperatures; while lithium conductivity in rocksalt type oxides has been examined the ionic conductivity of other high entropy oxides had not been examined prior to Gild et al. in 2018. [14,36–40] The production of new materials for energy applications and thermal barrier coatings is a promising area for high entropy ceramics.

Refractory silicides are commonly utilized as coatings for refractory metals at high temperatures to prevent catastrophic oxidation in oxygen rich atmospheres. For instance, R512E is a commercial coating consisting of Si-20Fe-20Cr that is commonly applied to niobium alloys to minimize oxidation. [41] The fabrication of more complex silicides could allow for enhanced oxidation resistance of the coating as well as foresight into what type of compounds will appear when traditional reactive silicide coatings are applied to high entropy alloy substrates. The oxidation behavior and kinetics of high entropy alloys and ceramics is an area of new research but preliminary results suggest the formation of complex oxides that will require progress beyond the traditional oxidation resistant coatings. [42–44]

In 2016, Gild et al. expanded high entropy ceramics into the non-oxide realm with the fabrication of seven high entropy diborides, including $(Hf_{0.2}Zr_{0.2}Ta_{0.2}Nb_{0.2}Ti_{0.2})B_2$ and five other single phase compounds. [45] The high entropy diborides showed superior hardness and oxidation resistance compared to the constituent binary diboride systems. Since then, the high entropy ceramic field has rapidly expanded to include carbides, nitrides, sulfides, as well as fluorite, spinel, rocksalt, magnetoplumbite, and silicate oxides. [40,45–55] Similar to the high entropy alloy field, high entropy ceramics are observed to have increased hardness and reduced thermal conductivity compared to their constituent materials; at the moment, mechanical property characterization is still very sparse in the literature.

1.2 Objective and Overview

The objective of this research project is to fabricate and characterize a wide swath of the burgeoning field of high entropy ceramics. In particular, the production and characterization of high entropy diborides is the primary emphasis of the work. The project can be divided into six

sections. In chapter two, the fabrication and characterization of high entropy diborides from commercial powder utilizing high energy ball milling and spark plasma sintering is examined. In chapter three, the fabrication of high entropy diboride-graphite or carbide-graphite composites utilizing commercial powders, minimal milling, and flash spark plasma sintering is the focus. In chapter four, the synthesis of high entropy diboride powder via various borothermal and borocarbothermal reduction methods is performed. In chapter five, we fabricate and characterize high entropy fluorite oxides based off of an 8YSZ type basis. In chapter six, the formation of high entropy disilicides via mechanical alloying and spark plasma sintering is examined.

Chapter 2: High-Entropy Metal Diborides: A New Class of High-Entropy Materials and a New Type of Ultrahigh Temperature Ceramics

2.1 Introduction

Recently, the fabrication and properties of metallic high entropy alloys (HEAs) have attracted significant research interests.[1,2] In an HEA, the configurational entropy of a solid-solution phase is maximized to stabilize it against the formation of intermetallics. Typically, five or more elements can be mixed in a HEA in equimolar concentrations to produce a maximum molar configurational entropy of $\Delta S_{mix} = R\ln N$, where N is the number of equimolar components and R is the gas constant.[3,4] HEAs have shown superior mechanical and physical properties; especially, a series of recent studies fabricated a class of refractory, metallic HEAs and demonstrated their excellent wear resistance and strength, including (especially) exceptional high-temperature properties.[1–8] Since the minimization of Gibbs free energy ($G = H - TS$, where H is enthalpy, S is entropy, and T is temperature) dictates the thermodynamic stability of a material at a constant pressure, a high-entropy material (with large S) can be thermodynamically more stable (particularly) at high temperatures, motivating this study to explore the phase stability and fabrication feasibility of high-entropy metal diborides, as a new type of high-entropy materials as well as a new class of ultra-high temperature ceramics (UHTCs).

Most prior studies of crystalline high-entropy materials have been conducted for metallic HEAs of mostly simple face- and body-centered cubic (FCC and BCC), as well as occasionally hexagonal close packing (HCP), crystal structures; much less studies have been done for making crystalline high-entropy ceramics (albeit that glasses can be considered high-entropy materials in a broad definition), particularly those with more complex, non-cubic, crystal structures.[1,2]

Most recently, Rost *et al.* successfully fabricated an entropy-stabilized oxide, $(Mg_{0.2}Co_{0.2}Ni_{0.2}Cu_{0.2}Zn_{0.2})O$, that possessed a single-phase rocksalt (which is also a FCC) structure when it was quenched from a sufficiently high temperature; subsequent studies revealed that this entropy-stabilized oxide and its derivatives, $(Mg_{0.2}Co_{0.2}Ni_{0.2}Cu_{0.2}Zn_{0.2})_{1-x-y}Ga_yA_xO$ (where A = Li, Na, or K), have colossal dielectric constants and superionic conductivities. [9–11] To the best of our knowledge, this class of entropy-stabilized oxides and its derivatives represent the first and only crystalline high-entropy ceramics that have been reported to date.

This study further extended the state of the art for the crystalline high-entropy ceramics via successfully synthesizing a new class of high-entropy metal diborides, including $(Hf_{0.2}Zr_{0.2}Ti_{0.2}Nb_{0.2}Ta_{0.2})B_2$, $(Hf_{0.2}Zr_{0.2}Ti_{0.2}Mo_{0.2}Ta_{0.2})B_2$, $(Hf_{0.2}Zr_{0.2}Mo_{0.2}Nb_{0.2}Ta_{0.2})B_2$, $(Hf_{0.2}Mo_{0.2}Ti_{0.2}Nb_{0.2}Ta_{0.2})B_2$, $(Mo_{0.2}Zr_{0.2}Ti_{0.2}Nb_{0.2}Ta_{0.2})B_2$, and $(Hf_{0.2}Zr_{0.2}Ti_{0.2}Cr_{0.2}Ta_{0.2})B_2$ (Table 2.1). This work has greatly extended the knowledge of high-entropy materials, not only since it is the first time crystalline high-entropy non-oxide ceramics (specially borides) have been synthesized, but also because these high-entropy metal diborides exhibit a unique layered hexagonal crystal structure with alternating rigid two-dimensional (2D) boron nets and *high-entropy 2D layers* of metal cations (as essentially a class of quasi-2D high-entropy materials), as schematically shown in Fig. 1, which distinctly differs from any other high-entropy crystalline phases reported to date.

2.2 Results

2.2.1 Phase Evolution and Formation of High-Entropy Ceramic Phases

To synthesize high-entropy metal diborides, five commercial metal diboride powders of equimolar amounts were mixed and mechanically alloyed via high energy ball milling (HEBM)

for six hours; subsequently, the HEBM powders were compacted into disks of 20-mm diameter and densified utilizing spark plasmas sintering (SPS) at 2000°C for 5 minutes under a pressure of 30 MPa. The detailed synthesis procedure was described in the "Methods" section. Seven high-entropy metal diboride compositions were tested in this study, which are sometimes referred as HEB #1-#7 (as listed in Table 2.1 and 2.2. Representative X-ray diffraction (XRD) patterns shown in Fig. 2 and Fig. 2.9 - 2.15 illustrate the phase evolution during the HEBM and SPS fabrication process. The initial mixture of powder displayed XRD peaks for five individual metal diboride phases (although some peaks overlap for most compositions), which broadened and merged (due to the particle size reduction and mechanical alloying effects during HEBM); eventually, a single, high-entropy, phase of the hexagonal AlB_2 structure formed after SPS at 2000°C (Fig. 2; Fig. 2.9 - 2.15). Full-range XRD patterns of the SPS specimens are displayed in Fig. 3 (and in expanded views in Fig. 2.9 - 2.15), where six of them, *i.e.*, $Hf_{0.2}Zr_{0.2}Ti_{0.2}Nb_{0.2}Ta_{0.2})B_2$, $(Hf_{0.2}Zr_{0.2}Ti_{0.2}Mo_{0.2}Ta_{0.2})B_2$, $(Hf_{0.2}Zr_{0.2}Mo_{0.2}Nb_{0.2}Ta_{0.2})B_2$, $(Hf_{0.2}Mo_{0.2}Ti_{0.2}Nb_{0.2}Ta_{0.2})B_2$, $(Mo_{0.2}Zr_{0.2}Ti_{0.2}Nb_{0.2}Ta_{0.2})B_2$, and $(Hf_{0.2}Zr_{0.2}Ti_{0.2}Cr_{0.2}Ta_{0.2})B_2$, exhibit largely a single hexagonal phase, albeit the presence of minor secondary (Zr, Hf)O_2 phases; these secondary oxide phases are represented by the low-intensity peaks that are evident in Figs. 2 and 3, which are not indexed in Figs. 2 and 3 for the figure clarity, but indicated by the solid dots in Figs. 2.9 - 2.15. The formation of minor amounts of secondary oxide (ZrO_2 or HfO_2) phases is commonly observed in sintered ZrB_2 and HfB_2 specimens, which are native oxides that are difficult to remove (because of the extreme stabilities of native oxides of ZrO_2 and HfO_2). As the only special case, a secondary boride phase was observed in HEB #6, $(Hf_{0.2}Zr_{0.2}W_{0.2}Mo_{0.2}Ta_{0.2})B_2$, with XRD peaks matching those of the $(Ti_{1.6}W_{2.4})B_4$ compound, while the major XRD peaks still represent a hexagonal metal diboride solid-solution phase (Fig.

3 and Fig. S6).

2.2.2 Compositional Uniformity

Cross-sectional scanning electron microscopy (SEM) images and the corresponding energy dispersive X-ray (EDX) spectroscopy compositional maps of three selected specimens (after SPS at 2000°C) are shown in Fig. 4 (and additional EDX compositional maps of all seven specimens are documented in the Figs. 2.9 - 2.15). The compositions of all specimens are largely uniform, albeit the presence of uniformly-distributed minor secondary (Zr, Hf)O_2 phases (to different extents in different specimens), as well as the $(Ti_{1.6}W_{2.4})B_4$ secondary phase in HEB #6 (only). Less than 1 at.% W (tungsten) is present in Specimens #1-#5 and #7 as contamination from the WC-based milling media used in HEBM. EDX mapping operating at 20kV also found micrometer-scale Nb (niobium) localization in Specimens #1 and #3-#5, with occasional Zr and Mo clustering occurring concurrently in the same regions. This is somewhat surprising considering the fact that NbB_2 generally forms continuous solid solutions with other metal diborides.[12] Presumably, the Nb localization is due to kinetic effects and can be homogenized with annealing for a prolonged time or at higher temperatures. In general, the compositional homogeneities are largely satisfactory, as shown in Fig. 4 (and in expanded views in Figs. 2.9 - 2.15 for all seven specimens); they are significantly more homogenous than the typical (BCC) refractory HEAs made by casting, which usually form dendrite structures with severe compositional segregations.[7]

2.2.3 Atomic-Resolution Structural Characterization

AC STEM HAADF and ABF imaging has been conducted to confirm the formation of uniform solid solution at nanometer and atomic scales, particularly the formation 2-D high-

entropy metal layers (separated by the rigid 2-D boron nets in the (0001) basal planes) without any significant layer-to-layer variation (or layered segregation) of different metal atoms in different (0001) planes perpendicular to the *c*-axis. The STEM-ABF and STEM-HAADF images in Fig. 5(a) and (b) show a homogeneous solid solution phase in the HEB #2, $Hf_{0.2}Zr_{0.2}Ti_{0.2}Mo_{0.2}Ta_{0.2})B_2$. STEM ABF and HAADF images with higher magnification showed the atomic configuration of atoms in the view of $[01\bar{1}0]$ zone axis. The atomic planes (0001) and $(01\bar{1}0)$ were indicated in Fig. 5(c). The mean spacing between two (0001) planes is about 3.449 Å, which is close to 3.316Å measured by XRD. In Fig. 5(c), the metallic atoms were highlighted by red circles on (0001) plane. Light element B can be visualized via ABF imaging. The highlighted green dots in Fig. 5(c) indicated the B atoms, which are located between two basal planes (0001). The observed atomic configuration is consistent with the unit cell model depicted in Fig. 1. The same atomic configuration and homogeneity were also observed in different locations (Figs. 2.16 and 2.17) and a different specimen (Figure 2.18). A careful digital image analysis (Fig. 2.19) revealed that the measured standard deviations of lattice spacings between the basal (0001) planes are only ~0.6% of the average measured *c* lattice parameter or the measured variations from STEM ABF and HAADF images are ~0.02Å, which directly confirmed the formation 2-D high-entropy metal layers without a layered segregation of different metal specimens in different (0001) basal planes, where these 2-D metal layers are well separated by the rigid 2-D boron nets in between (Fig. 1). Thus, these high-entropy metal diborides can be considered as (layered) quasi-2D high-entropy materials, as schematically illustrated in Fig. 1.

2.2.4 Nanoscale Compositional Mapping

The compositional homogeneity at nanoscale for the HEB #2, $(Hf_{0.2}Zr_{0.2}Ti_{0.2}Mo_{0.2}Ta_{0.2})B_2$, was confirmed by EDX maps for different metallic elements. Fig. 6 showed that Hf, Zr, Ta, Mo and Ti were uniformly distributed at nanoscale. No segregation or aggregation was found throughout the scanned area. Since these compositional maps were also taken with the electron beam being parallel to the $[01\bar{1}0]$ zone axis, they also confirmed no layered segregation along the *c*-axis in (0001) basal planes; thus, this is indeed a quasi-2D high-entropy material as illustrated in Fig. 1. Additional EDX mapping at a different location was also conducted and documented in Fig. 2.19.

2.2.5 Densification and Lattice Parameters

In general, greater than 92% of theoretical densities has been achieved by SPS at 2000°C (Table 2.1; see Table 2.2 for the actual measured densities, along with the theoretical densities calculated using the lattice parameters measured by XRD). The lattice parameters were measured from XRD and listed in Table 2.1. Typically, the measured lattice parameters are within <1% of those calculated by the rule of mixtures (Table 2.1), which, along with the narrow XRD peaks (where the peak widths are much narrower than the mean differences among the five peaks of individual metal diborides, as shown in Fig. 2 and Figs. 2.9 - 2.15), indicates the formation of disordered solid solutions for all high-entropy metal diborides made in this study (consistent with the direct STEM HAADF/ABF imaging and nanoscale compositional mapping as shown in Fig. 5 and Fig. 6).

2.2.6 Hardness and Oxidation Resistance

Initial property assessments indicated that both the hardness and the oxidation resistance of these high-entropy metal diborides are generally greater or better than the average

performances of the individual (conventional) metal diborides made by the identical HEBM and SPS fabrication processing. We understand that both hardness and oxidation resistance should critically depend on microstructures; the presence of porosity and oxide inclusion, as a consequence of the HEBM procedure that we adopted for promoting the homogenization of high-entropy solid solutions, adversely affected the hardness and oxidation resistance. To conduct a fair assessment of the relative performance of high-entropy and conventional metal diborides, we measured six single-phase high-entropy diborides, along with a controlled group of HfB_2, ZrB_2, TaB_2, NbB_2, TiB_2, and CrB_2 specimens made by the identical HEBM and SPS fabrication processing using the same processing parameters (except for CrB_2; see "Methods" section for explanation). Fig. 7 displays the measured hardness of six high-entropy metal diborides (with the actual measured data being listed in Table 2.4), which are generally greater than the averages of the hardness values measured from individual metal diborides fabricated via the same route. Because MoB_2 is not an equilibrium bulk phase below 1500°C, the averages for HEB#2-HEB#5 that contains 20% MoB_2 were calculated without MoB_2. Yet, it is well established that MoB_2 has a lower melting temperature and theoretical hardness than all the other metal diborides in HEB#2-HEB#5 (HfB_2, ZrB_2, TaB_2, NbB_2, and TiB_2) so that the actual averages from the "rule of mixtures," if we could make and measure MoB_2 via the same procedure, should be even lower. Furthermore, results from an initial oxidation resistance measurement of these high-entropy and individual metal diborides made by the identical fabrication processing are shown in Fig. 8, with additional data and images documented in 2.21-2.23. Taking HEB#1 $(Hf_{0.2}Zr_{0.2}Ti_{0.2}Nb_{0.2}Ta_{0.2})B_2$ as an example (which is a good case for considering because none of its oxides is volatile in this temperature range so that the weight gains shown in Fig. 8 and Fig. 2.21 are easier to interpret), Figs. 8, 2.21 and 2.22 show that

HEB#1 performs better than most of its individual components made with the same procedure (ZrB_2, TaB_2, NbB_2, and TiB_2) except for HfB_2; it certainly performs better than the "average" performance of these five individual metal diborides. Consistently, both HEB #1 and HEB #7 maintained their shapes even at 1500°C, while the majority of the respective individual metal diborides (except for HfB_2) that were fabricated via the same HEBM and SPS route oxidized more severely. For example, the TiB_2 specimen, which represents one most widely-used metal diboride today, pulverized completely at 1500°C (Fig. 2.22). Finally, the four MoB_2-containing high-entropy diborides (HEB#2-HEB#5) exhibited interesting and diverse oxidation behaviors because MoO_3 is volatile. Despite this, some of them still perform better than many conventional metal diborides that do not have volatile native oxides (Figs. 2.21 and 2.23).

2.3 Discussion

The formation of (metallic) HEAs are often predicted by using the atomic-size effect (δ) and the enthalpy of mixing (ΔH_{mix}) as the two main criteria.[1,2] The enthalpy of mixing is difficult to quantify for the current case, so attention is focused on analyzing the atomic-size effect. The original Hume-Rothery solid-solution rule suggests that $(r_{\text{solute}} - r_{\text{solvent}})/r_{\text{solvent}} \leq 15\%$ is one of the necessary conditions for forming a binary solid solution. Following the same concept, the average atomic-size difference (δ) can be defined for a multicomponent HEA alloy, as:

$$\delta \equiv \sqrt{\sum_{i=1}^{N} X_i \left[1 - r_i \Big/ \left(\sum_{i=1}^{N} X_i r_i\right)\right]^2} \qquad (1)$$

where r_i and X_i are the atomic radius and molar content, respectively, of the i-th component. Prior studies suggested, mostly based on empirical observations, that a necessary

(but not sufficient) criterion for forming a single-phase (disordered) HEA is that the computed δ of the solid solution should be sufficiently small: $\delta \leq \delta_{max} \approx 4\%$ [1] or 4.3%. [1,2] By simply plugging the values of metallic or covalent radii of the metals, and the computed δ values are in the range of 3.5% to ~8% in Table 2.4; specifically, HEB #7 has the highest $\delta \approx 8\%$; yet, it still forms single-phase, high-entropy, solid solution. In reality, metal diborides [$M^{2+}(B^{-})_2$] form a highly anisotropic layered structure (*i.e.*, the hexagonal AlB_2 structure), where each metal atom donates two electrons and the M-B bonds (between the metal and B layers) have mixed ionic and covalent characteristics (see Fig. 1). Within the 2D metal layers, M-M bonds are strained significantly by the more rigid boron net (Fig. 1). Thus, none of the available (metallic, covalent or ionic) radii can effectively represent the actual bond lengths in the metal diborides in the AlB_2 structure (Fig. 1).[13]

Alternatively, we propose to calculate the average size difference for a high-entropy metal diboride using the lattice constants of individual metal diborides (measured lattice parameters a_i and c_i for the *i*-th MB_2, as summarized in Ref. 14, instead of the atomic radii of metals), as:

$$\delta_a = \sqrt{\sum_{i=1}^{N} X_i \left[1 - a_i \Big/ \left(\sum_{i=1}^{N} X_i a_i\right)\right]^2} \tag{2}$$

and

$$\delta_c = \sqrt{\sum_{i=1}^{N} X_i \left[1 - c_i \Big/ \left(\sum_{i=1}^{N} X_i c_i\right)\right]^2} \tag{3}$$

Subsequently, the values of δ_a and δ_c have been computed for the seven specimens and

listed in Table 2.1 and Table 2.2.[14] Interestingly, the computed δ_a values are small (in the range of 1.3% to 2.3% for all seven specimens) because the M-M bonds are strained by the rigid boron net (that can deform metal cations and M-M bond lengths towards an ideal "strain-free" value dictated by stronger B-B bonds; Fig. 1).[13] Thus, the computed δ_c values may better represent the average size difference because of less constraint along the *c*-axis. Coincidentally, Specimens #1-#5 and #7, for which single-phase, high-entropy, solid solutions did form, all have computed δ_c values in the range of 3.9% to 5.2%, whereas HEB #6, for which single-phase did not form, has the largest computed δ_c value of ~6.2%. It is interesting to further note that HEB #7 (with a simple high-entropy phase) has a greater δ_a but smaller δ_c than those of HEB #6 (with two boride phases), suggesting that a smaller δ_c may be more important than a smaller δ_a.

However, we should emphasize that small differences in lattice parameters (measured by small δ_a and δ_c) are only one necessary, but not essential, condition for forming high-entropy solutions. A very small δ value is certainly not a guarantee for forming a single-phase, high-entropy, solid solution. For example, the precipitation of the secondary $(Ti_{1.6}W_{2.4})B_4$ phase in HEB #6 may be related to the facts that this $(Ti_{1.6}W_{2.4})B_4$ phase is extremely stable or WB_2 is not stable by itself; further investigation is needed here to clarify the most important reason for the precipitation of $(Ti_{1.6}W_{2.4})B_4$ in HEB #6.

Moreover, the average size differences are certainly not the only factors that determine the ability to form a single high-entropy phase. For example, it is known that an average lattice parameter *a* of ~3.04Å would produce "strain-free" metal layers that match the rigid boron net, thereby being favored; this may also be a factor for HEB #7 to exhibit single high-entropy phase since its average *a* (of ~3.081Å) has the closest match to the ideal strain-free value (Table 2.2;

despite that this factor also favors HEB #6, where the largest δ_c may be a determining factor).[13] In addition to the several size factors discussed above, the mixing enthalpy, as well as the valence electron concentration, may also play an important role in determining whether a single high-entropy phase forms.[1,2]

It is worth making a few additional notes regarding the observed phase stabilities. First, perhaps the most interesting observation is the formation of a single-phase, high-entropy solution in HEB #7, $(Hf_{0.2}Zr_{0.2}Ti_{0.2}Cr_{0.2}Ta_{0.2})B_2$, despite the limited solid solubilities of CrB_2 in both HfB_2 and ZrB_2.[12,15] Second, MoB_2 is believed to be metastable at room temperature, but the hexagonal MoB_2 phase could be retained in the SPS specimens; in this study, four 20%-Mo-containing high-entropy metal diborides have been made.[16] Third, the starting powder W_2B_5 (since WB_2 is not commercially available) possessed a different structure and it has limited solubilities in all diborides except for TiB_2, which can be another reason that HEB #6 did not possess a single solid-solution phase (in addition to the largest δ_c of ~6.2%). [17–19]

It is important to emphasize that both the hardness and oxidation resistance can be affected by the microstructure, *e.g.*, the porosity and oxide inclusions, significantly. Thus, we choose to compare the high-entropy and individual metal diborides fabricated using the same method to allow a fair assessment of relative hardness and oxidation resistance (even if our specimens have high levels of porosity and oxidation inclusions due to HEBM than those fully-dense and oxide-free specimens prepared by other fabrication routes). We expect that fully-dense and oxide-free specimens should have higher hardness and better oxidation resistance.

Although the high-entropy metal diborides do appear to exhibit greater hardness and better oxidization resistance than the average performances of the individual metal diborides

(provided that they are made with the same fabrication route), perhaps a more important advantage for adopting high-entropy materials is a large compositional design space to allow tuning of properties. This will be particularly important for improving oxidation resistance, which depends on many (often kinetic) factors; thus, there is perhaps no simple answer on whether high-entropy metal diborides are good or bad for oxidation resistance (and some other properties). A large compositional design space is useful for designing better protective oxide scales (with additives or in composites, which are often necessary for real applications), representing a complex material engineering problem beyond the scope of this study. Further systematic investigation of hardness, oxidation resistance, and other properties of the high-entropy metal diborides, which often critically depend on the microstructure and therefore the processing optimization, is important but beyond the scope of this study that focuses on the formation, structure, microstructure, and thermodynamic stability of this new class of high-entropy materials.

In summary, this study has successfully synthesized six single-phase, high-entropy, metal diborides via mechanical alloying and SPS. In general, metal diboride-based UHTCs have ultrahigh melting points, as well as excellent thermal and electrical conductivities, hardness, and wear and oxidation resistances; thus, they have potential structural applications in extreme environments.[13,15,20–23] In addition, with a unique, layered hexagonal (AlB_2) crystal structure, with alternating metal and boron layers, some metal diborides also exhibit exotic functionality, *e.g.*, MgB_2 is a well-known superconductor. While extensive future research has to be conducted to investigate their mechanical, chemical (oxidation), and physical properties, these high-entropy metal diborides represent a new class of UHTCs, as well as a new type of high-entropy materials that can have unique compositions and structures that differ distinctly from any

other existing materials, as well as great possibilities of tailoring their properties via an extremely-large compositional engineering space.

2.4 Methods

2.4.1 Synthesis of High-Entropy Metal Diboride Specimens

To synthesize high-entropy metal diborides, powders of HfB_2, ZrB_2, NbB_2, TiB_2, W_2B_5 (to substitute WB_2 that is not commercially available), CrB_2 (99.5% purity; purchased from Alfa Aesar, MA, USA), TaB_2, and MoB_2 (99% purity; purchased from Goodfellow, PA, USA) were utilized as starting materials. Appropriate amounts of five powders were utilized to fabricate specimens of each composition (with the stoichiometry being calculated on the metal basis). The seven compositions are listed in Table 2.1 and referred to as HEB #1 to #7 in the text. The raw powders were mechanically alloyed via high energy ball milling (HEBM) using a Spex 8000D mill (SpexCertPrep, NJ, USA) for six hours in WC media. To prevent overheating, the HEBM was stopped every 60 minutes to allow cooling for five minutes. The powders were then hand ground in an agate mortar to a 325 mesh; subsequently, they were compacted into disks of 20-mm diameter and densified utilizing spark plasmas sintering (SPS, Thermal Technologies, CA, USA) in vacuum (10^{-2} Torr) at 2000°C for 5 minutes under a pressure of 30 MPa, with a heating ramp rate of 100 °C/min. The inside of the graphite die was lined with a 25μm-thick molybdenum foil to prevent reactions between the graphite and the diboride specimen. The molybdenum foil was then lined with a layer of 125μm-thick graphite paper to minimize reactions between the foil and the outer die.

2.4.2 Characterization

The specimens were characterized by X-ray diffraction (XRD) using a Rigaku

diffractometer with Cu Kα radiation and scanning electron microscopy (SEM) in conjunction with energy dispersive X-ray spectroscopy (EDX). The specimen densities were measured via the Archimedes method to an accuracy of ± 0.01 g/cm^2 and the relative densities were calculated via using theoretical densities that were determined by the ideal stoichiometry and lattice parameters measured by XRD. The atomic and nanoscale characterization was conducted using aberration-corrected scanning transmission electron microscopy (AC STEM); STEM high-angle annular dark-field (HAADF) images, medium-angle annular dark-field (MAADF), and annular bright-field (ABF) images were taken by using a 200 kV STEM (ARM-200F, JEOL) equipped with a probe Cs corrector (CEOS Gmbh), which offers an unprecedented opportunity to probe structures with a sub-Ångström resolution. For HAADF imaging, we adopted a probe convergence angle of ~ 22 mrad and a detector with inner semi-angle of > 60 mrad. The ABF images were taken with a detector of 12-23 mrad, while MAADF images were taken with a detector of 23-50 mrad. The energy dispersion X-ray (EDX) spectroscopy was employed to map the chemical composition at nanoscale. The TEM samples were prepared by dual-beam FIB/SEM system (Scios, FEI).

2.4.3 Hardness and Oxidation Measurements

Hardness and oxidation measurements were conducted using all six single-phase high-entropy diborides (HEB #1-#5 and #7) and six individual metal diboride benchmarking specimens (HfB_2, ZrB_2, TaB_2, NbB_2, TiB_2, and CrB_2) that were made by the same HEBM and SPS fabrication method using the same processing parameters, with one exception that CrB_2 was sintered at lower temperature of 1800°C because its substantially lower melting (and therefore sintering) temperature. MoB_2 was not examined because it is not a thermodynamically stable phase (and will decompose to MoB and Mo_2B_5) below 1500°C. Hardness measurements were

performed with a Vickers' diamond indenter at 200 kgf/mm^2 with a hold time of 15 seconds. The indentations were examined for conformation with the ASTM C1327. The indentations averaged 20-25 μm in width during the testing. Multiple measurements were performed at different locations of each specimen; the mean and standard deviation are reported. The density and hardness are generally uniform at different locations for HEB specimens #1-#5 and all six individual metal diboride specimens; however, HEB #7 has a denser outside shell and less dense inner core with different average hardness values (due to the effect of low-melting CrB_2 that promotes rapid densification near the surface); thus, the hardness values were measured at both regions and reported in Table 2.4 but only the overall mean and standard deviation were used in comparison. The oxidation experiments were conducted in a tube furnace under flowing dry air. The specimens were annealed at 800°C, 900°C, 1000°C, 1100°C, 1200°C, 1300°C, 1400°C, and 1500°C sequentially. Each annealing step included a one-hour isothermal oxidation at the desired temperature with a heating ramp rate of 10°C/min; after the isothermal annealing, the specimens were cooled in the furnace with uncontrolled cooling rates on the order of 100°C/min. After each annealing step, the specimens were removed from the furnace and weighted. At low annealing temperatures, specimens were weighted directly. At high temperatures (typically 1300°C and above), many specimens reacted with the alumina crucibles so that the specimens were weighted in the crucibles to obtain the net weight gains/losses. We found the measured weights are generally accurate for the oxidization temperatures of 1000-1200°C (from direct weighting of specimens) and for the annealing temperatures of 1400 and 1500°C, where the weight changes were sufficiently large to allow to be weighted accurately in crucibles. Outside these two temperature windows, the weight gains/losses were typically on the same order of magnitude as the measurement errors; thus, those data are not reported.

Chapter 2, in full, is a reprint of the material "High-Entropy Metal Diborides: A New Class of High-Entropy Materials and a New Type of Ultrahigh Temperature Ceramics" as it appears in *Scientific Reports*, J. Gild, Y. Zhang, T. Harrington, S. Jiang, T. Hu, M.C. Quinn, W.M. Mellor, N. Zhou, K. Vecchio, J. Luo, Scientific Reports 6 (2016) 37946. The dissertation author was the primary investigator and wrote the first draft of manuscript.

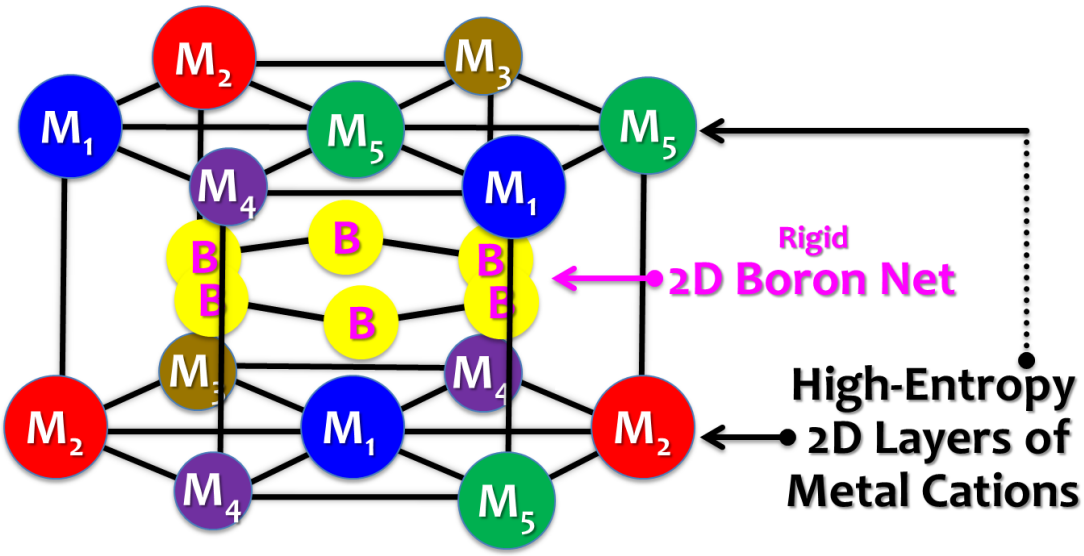

Figure 2.1 Schematic illustration of the atomic structure of the high-entropy metal diborides. Here, M_1, M_2, M_3, M_4, and M_5 represent five different transition metals (selected from Zr, Hf, Ti, Ta, Nb, W, and Mo). This new class of high-entropy materials and new type of UHTCs have a unique layered hexagonal crystal structure with alternating rigid 2D boron nets and high-entropy 2D layers of metal cations (as essentially a class of quasi-2D high-entropy materials), with mixed ionic and covalent (M-B) bonds between the metals and boron.

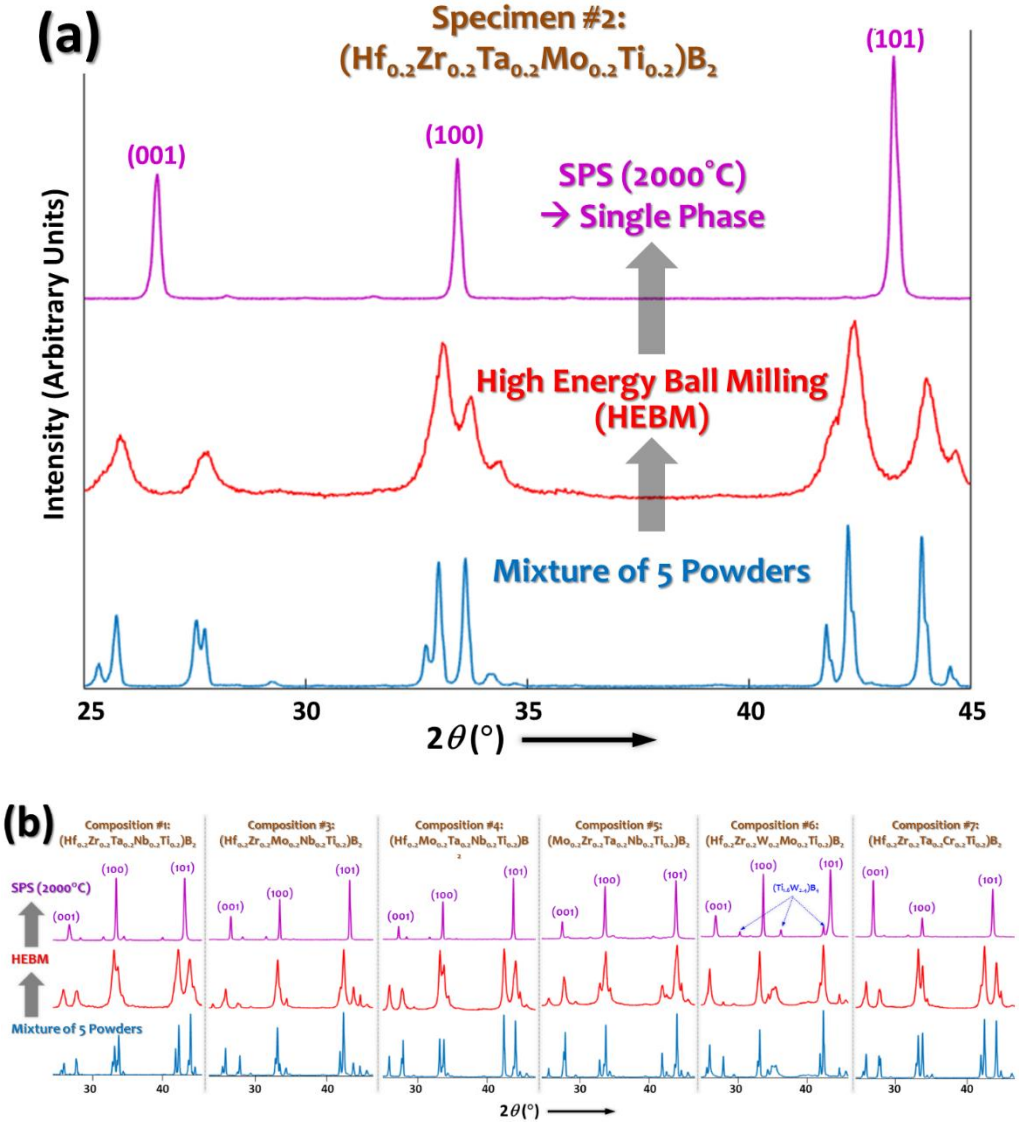

Figure 2.2 XRD patterns showing the phase evolution during the HEBM and SPS fabrication processes in (a) HEB #2 as an exemplar in an expanded scale and (b) six other specimens. Only the first three peaks of the high-entropy hexagonal AlB_2 phases are shown here for figure clarity; full-range XRD patterns (of $2\theta = 20° – 100°$, showing eleven XRD peaks of the high-entropy hexagonal phases) are documented in the Figs. 2.9 - 2.15.

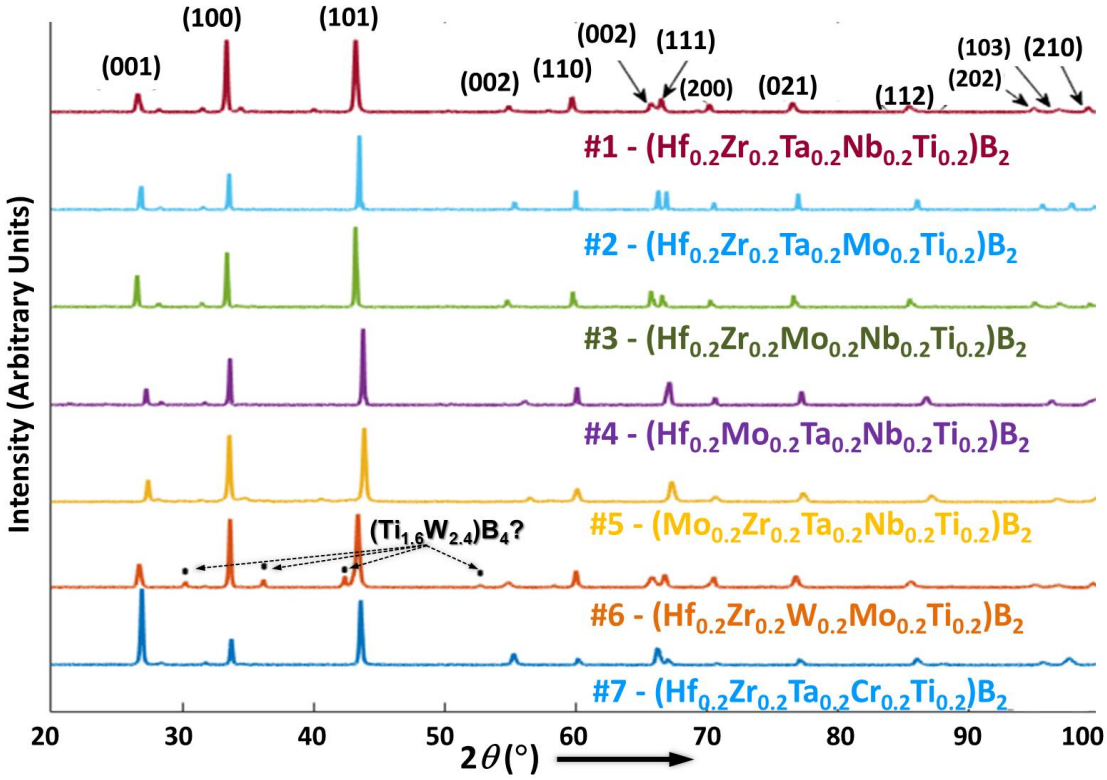

Figure 2.3 XRD patterns of all seven specimens after SPS at 2000 °C, where the peaks of the primary hexagonal phase are indexed. Six of seven specimens (except for HEB #6) exhibit largely a single hexagonal phase of the AlB_2 structure, albeit the presence of minor secondary (Zr, Hf)O_2 (native oxides), which are represented by the low-intensity peaks that are not indexed here the figure clarity (but indicated by the solid dots in Figs. 2.9 - 2.15). As the only special case, a secondary boride phase was observed in HEB #6, with XRD peaks matching those of the $(Ti_{1.6}W_{2.4})B_4$ compound, while the major XRD peaks still represent a hexagonal metal diboride solid-solution phase.

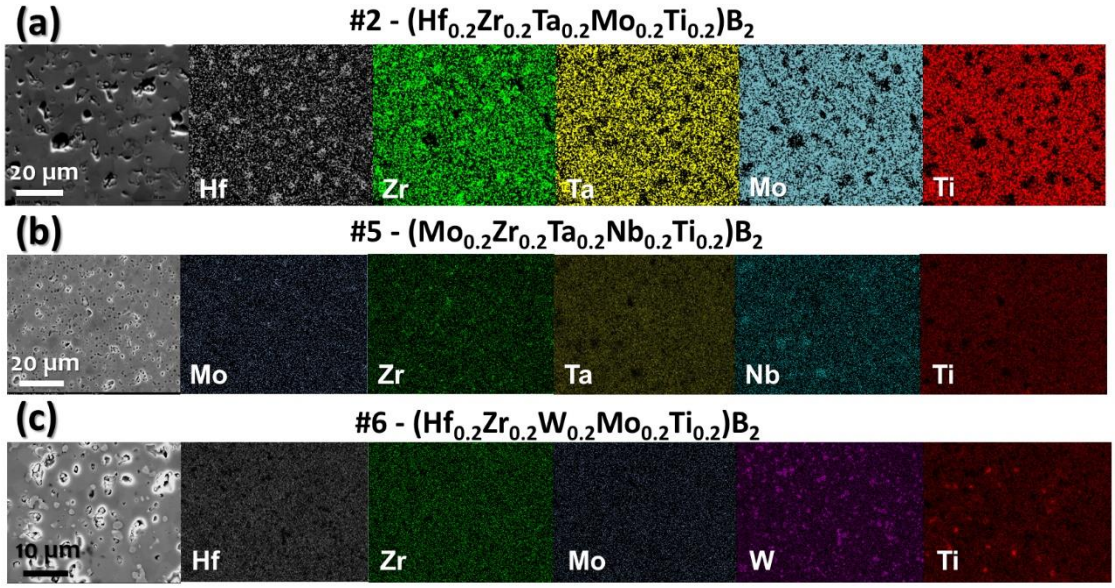

Figure 2.4 Cross-sectional SEM image and the corresponding EDX compositional maps of three selected specimens after SPS, showing the formation of largely homogeneous high-entropy solid-solution phases except for the HEB #6 shown in (c). The compositions are largely uniform albeit the presence of minor (Zr, Hf)O_2 based native oxides, *e.g.*, in (a), and some Nb clustering in four Nb-containing specimens, *e.g.*, in (b). The formation of a secondary boride phase was observed only in HEB # 6, as shown in (c). Additional EDX compositional maps (in expanded views) of all seven specimens are documented in the Figs. 2.9 - 2.15.

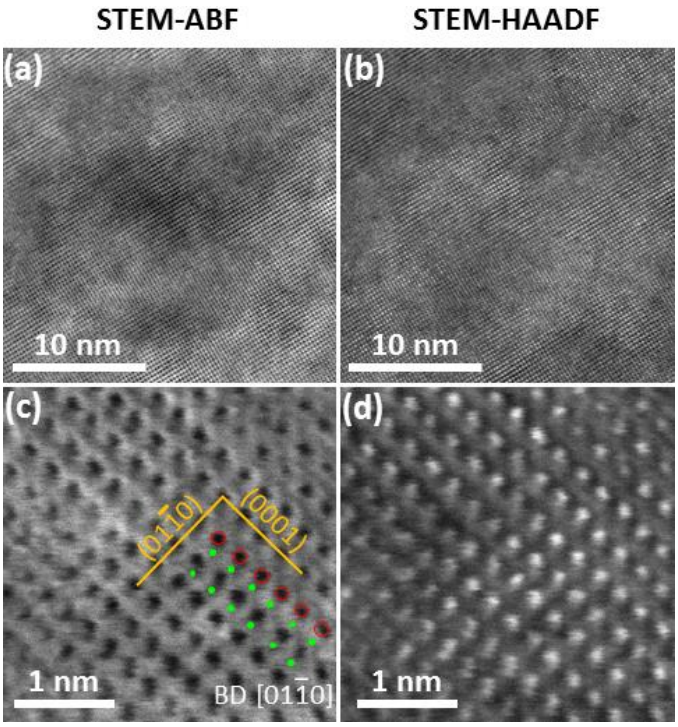

Figure 2.5 Atomic-resolution STEM ABF and HAADF images of HEB #2 ($Hf_{0.2}Zr_{0.2}Ta_{0.2}Mo_{0.2}Ti_{0.2}$)$B_2$. (a) and (b): ABF and HAADF images at a low magnification, showing the homogeneity of the solid-solution phase. (c) and (d): ABF and HAADF images at a higher magnification, showing atomic configuration. The electron beam is parallel to the $[01\bar{1}0]$ zone axis of hexagonal structure. (0001) and $(01\bar{1}0)$ planes are indexed in (c). The red circles highlight the columns of transition metal atoms (Hf, Zr, Ta, Mo and Ti). The green dots indicate the B atoms. Additional STEM images from different regions and a different specimen are documented in the Figs. 2.16-2.18; a further digital analysis of HAADF and ABF images in Fig. 2.19 shows that the standard variations in the (0001) lattice spacings are only ~ 0.6% or ~0.02Å, indicating homogenous mixing of five metal atoms (Hf, Zr, Ta, Mo and Ti) within the 2-D metal layers in (0001) planes.

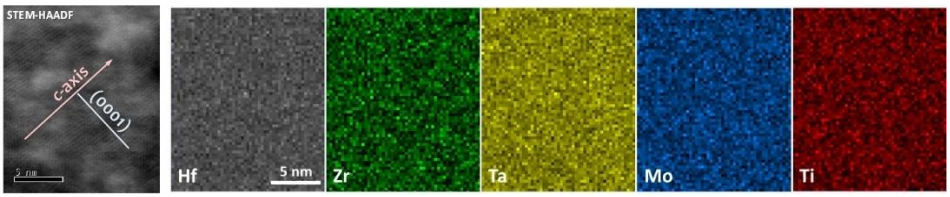

Figure 2.6 STEM-HAADF image and the corresponding EDS compositional maps for HEB #2 ($Hf_{0.2}Zr_{0.2}Ta_{0.2}Mo_{0.2}Ti_{0.2})B_2$, showing the homogeneous chemical distribution at nanoscale. These compositional maps were taken when the electron beam is parallel to the $[01\bar{1}0]$ zone axis, showing no significant layer-to-layer variations of metal composition in different basal (0001) planes. Additional EDX compositional maps obtained from a different region are documented in the Fig. 2.20.

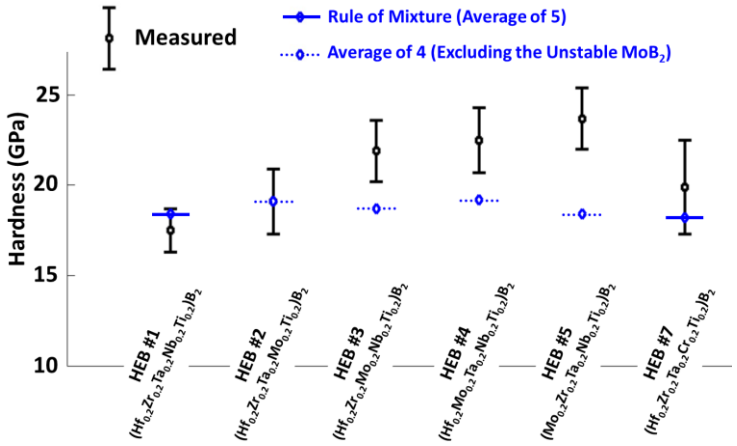

Figure 2.7 Measured hardness of six single-phase high-entropy metal diborides, which are generally greater than the "rule-of-mixtures" averages of the hardness values measured from individual metal diborides that were fabricated via the same HEBM and SPS route. Since MoB_2 is not an equilibrium bulk phase below 1500°C, the averages for HEB#2-HEB#5 were calculated without MoB_2. However, MoB_2 has a lower melting temperature and theoretical hardness than all other five other metal diborides in question; thus, the actual rule-of-mixtures averages should be even lower. It is also important to note that the hardness can be affected by porosity and oxide inclusions so that fully-dense and oxide-free metal diborides should have greater hardness than these measured values. We choose to compare the measured hardness values of high-entropy and conventional metal diborides fabricated by the same method to allow a fair assessment of relative values.

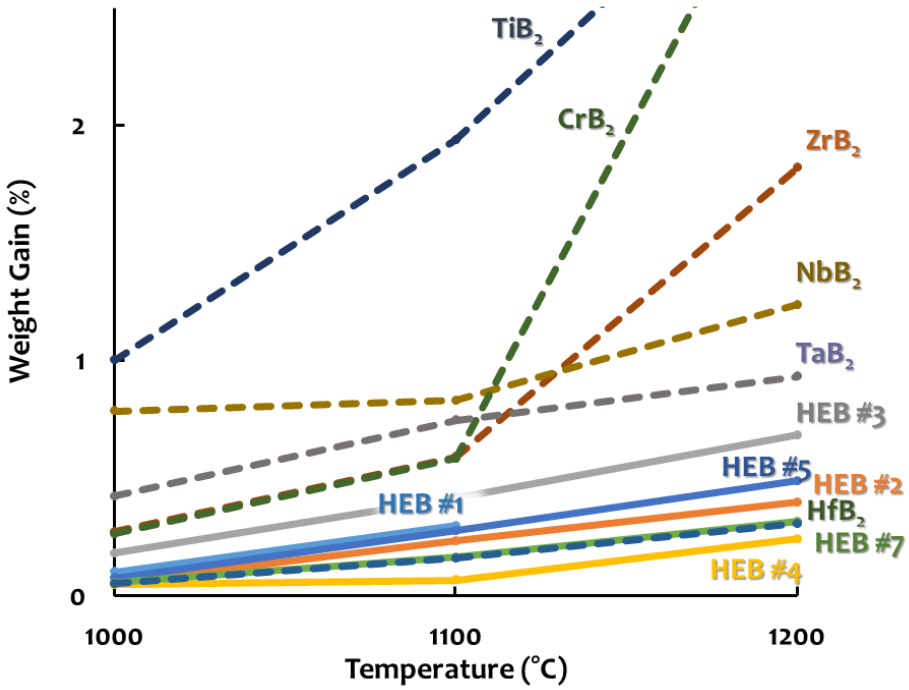

Figure 2.8 A snapshot of the relative oxidation performance of various high-entropy and individual metal diborides fabricated and tested with the same conditions. This figure displays percentage weight gain vs. oxidation temperature curves during annealing in flowing dry air at 1000°C, 1100°C, and 1200°C (for one hour each) sequentially for six single-phase high-entropy metal diborides [HEB #1 = $(Hf_{0.2}Zr_{0.2}Ti_{0.2}Nb_{0.2}Ta_{0.2})B_2$, HEB #2 = $(Hf_{0.2}Zr_{0.2}Ti_{0.2}Mo_{0.2}Ta_{0.2})B_2$, HEB #3 = $(Hf_{0.2}Zr_{0.2}Mo_{0.2}Nb_{0.2}Ta_{0.2})B_2$, HEB #4 = $(Hf_{0.2}Mo_{0.2}Ti_{0.2}Nb_{0.2}Ta_{0.2})B_2$, HEB #5 = $(Mo_{0.2}Zr_{0.2}Ti_{0.2}Nb_{0.2}Ta_{0.2})B_2$, and HEB #7 = $(Hf_{0.2}Zr_{0.2}Ti_{0.2}Cr_{0.2}Ta_{0.2})B_2$], along with six individual metal diborides fabricated via the same HEBM and SPS route. See the "Methods" section for the experimental procedure and Figs. 2.21-2.23 for additional results, including weight gain per surface area plots, weight percentage gains at higher temperatures, and images of all specimens after oxidation at different temperatures. In this figure (and Fig. 2.21), solid lines represent the high-entropy metal diborides and dashed lines represent the individual (conventional) metal diborides made by the same fabrication route.

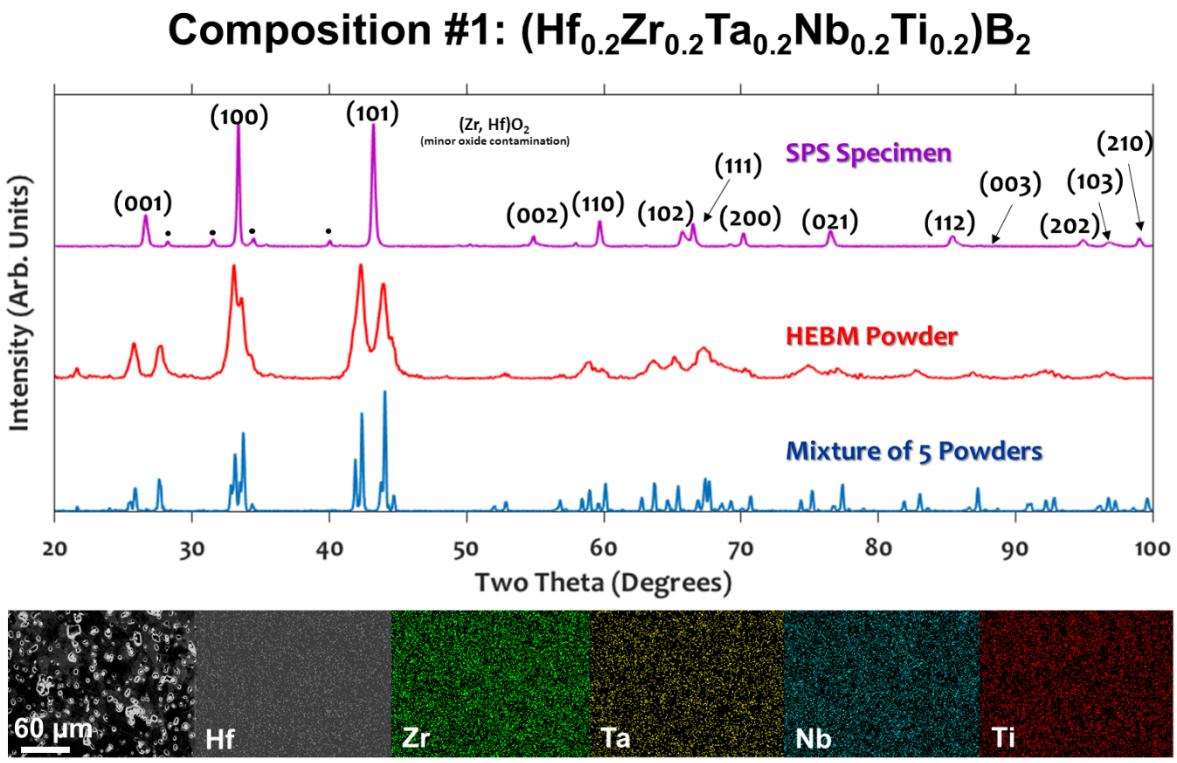

Figure 2.9 Specimen #1 $(Hf_{0.2}Zr_{0.2}Ta_{0.2}Nb_{0.2}Ti_{0.2})B_2$: **(a)** XRD patterns showing phase evolution during the HEBM-SPS fabrication process. **(b)** Cross-sectional SEM image and the corresponding EDX compositional maps of the specimen after SPS.

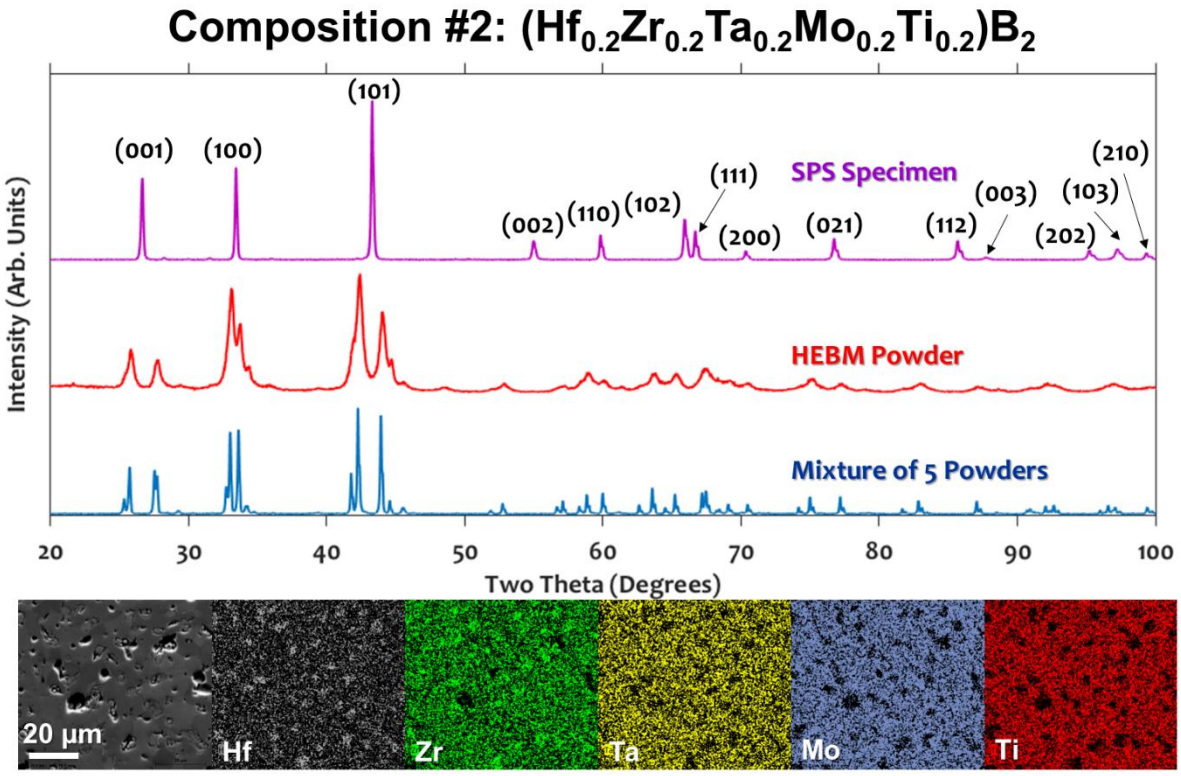

Figure 2.10 Specimen #2 ($Hf_{0.2}Zr_{0.2}Ta_{0.2}Mo_{0.2}Ti_{0.2})B_2$: **(a)** XRD patterns showing phase evolution during the HEBM-SPS fabrication process. **(b)** Cross-sectional SEM image and the corresponding EDX compositional maps of the specimen after SPS.

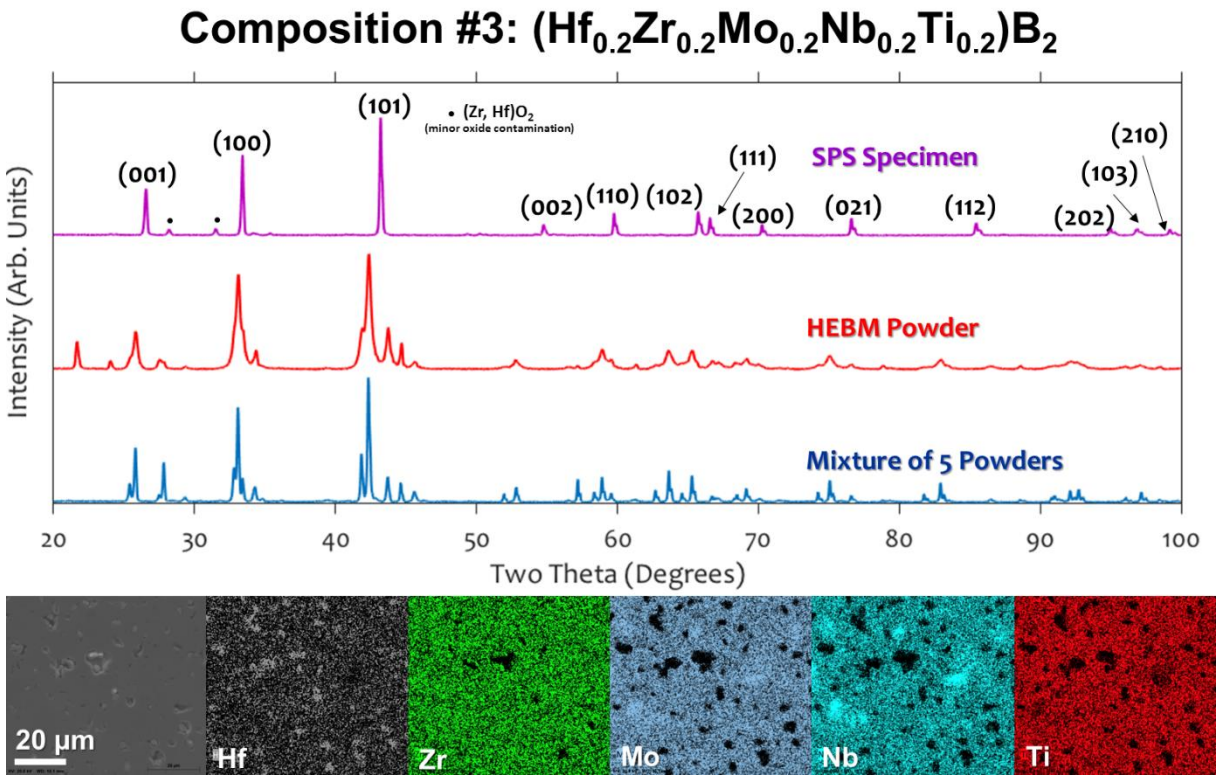

Figure 2.11 Specimen #3 $(Hf_{0.2}Zr_{0.2}Mo_{0.2}Nb_{0.2}Ti_{0.2})B_2$: **(a)** XRD patterns showing phase evolution during the HEBM-SPS fabrication process. **(b)** Cross-sectional SEM image and the corresponding EDX compositional maps of the specimen after SPS.

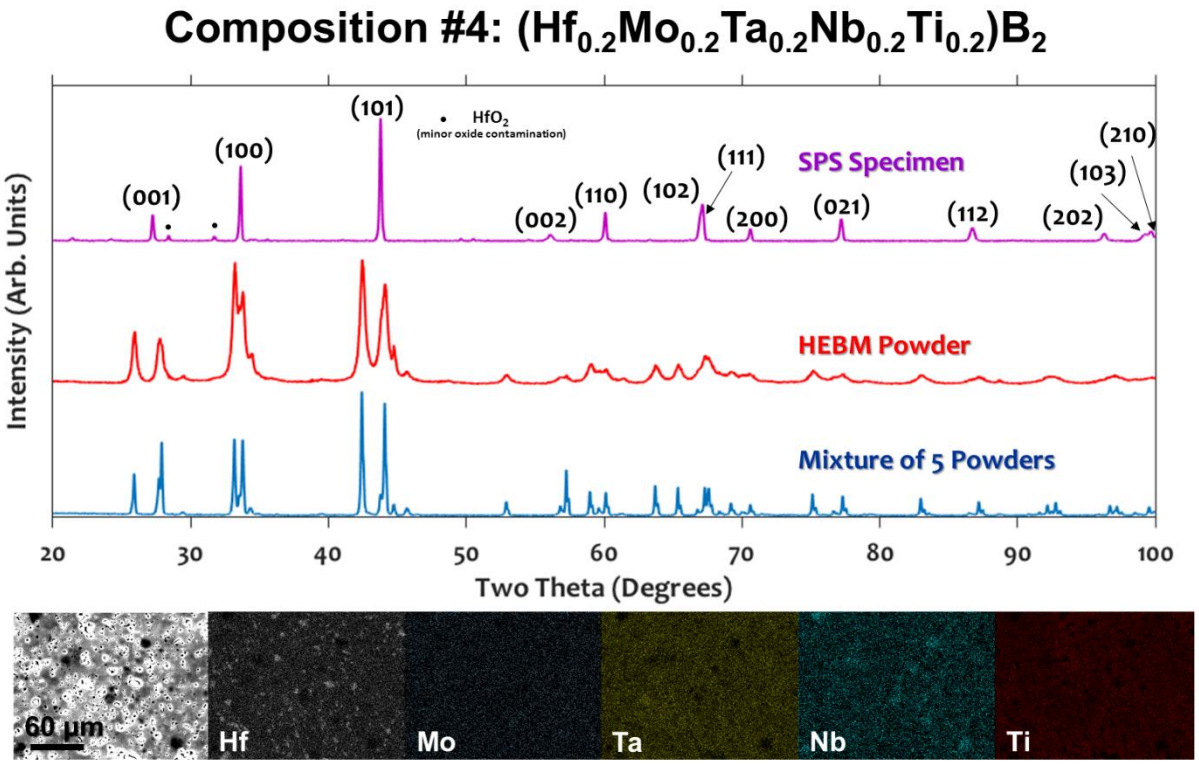

Figure 2.12 Specimen #4 ($Hf_{0.2}Mo_{0.2}Ta_{0.2}Nb_{0.2}Ti_{0.2})B_2$: **(a)** XRD patterns showing phase evolution during the HEBM-SPS fabrication process. **(b)** Cross-sectional SEM image and the corresponding EDX compositional maps of the specimen after SPS.

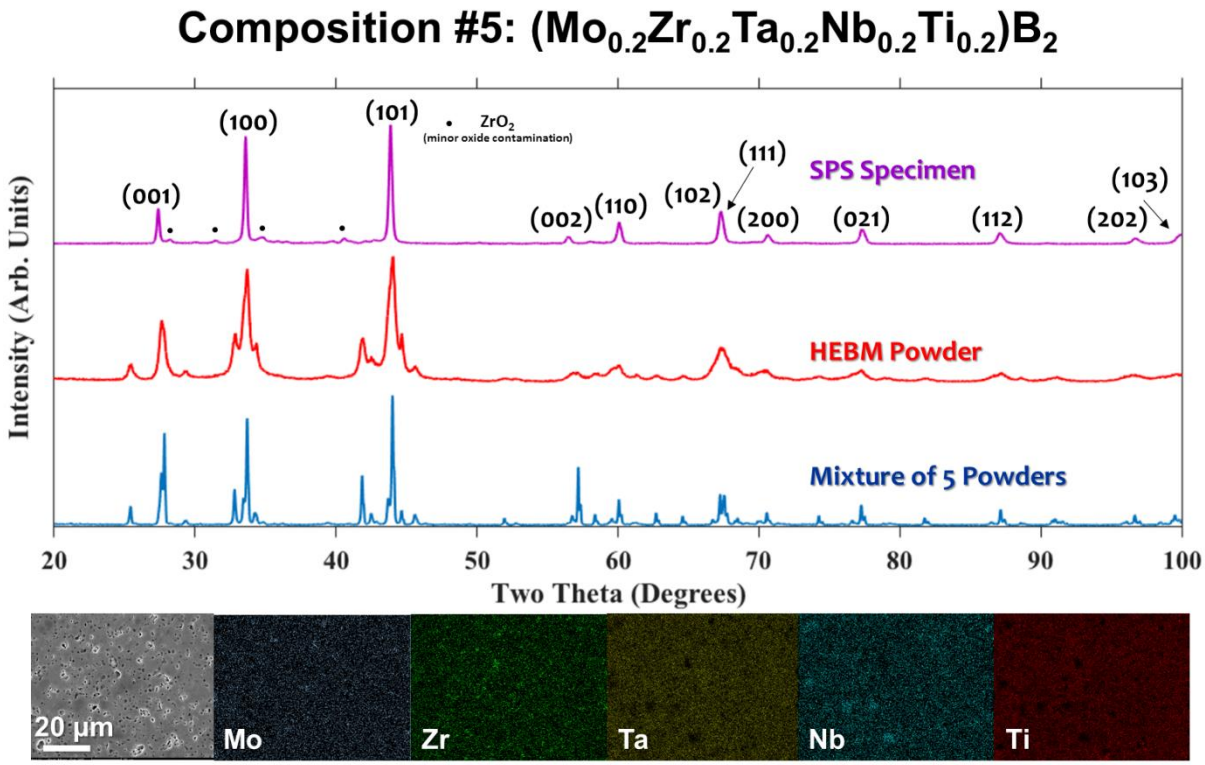

Figure 2.13 Specimen #5 ($Mo_{0.2}Hf_{0.2}Ta_{0.2}Nb_{0.2}Ti_{0.2})B_2$: **(a)** XRD patterns showing phase evolution during the HEBM-SPS fabrication process. **(b)** Cross-sectional SEM image and the corresponding EDX compositional maps of the specimen after SPS.

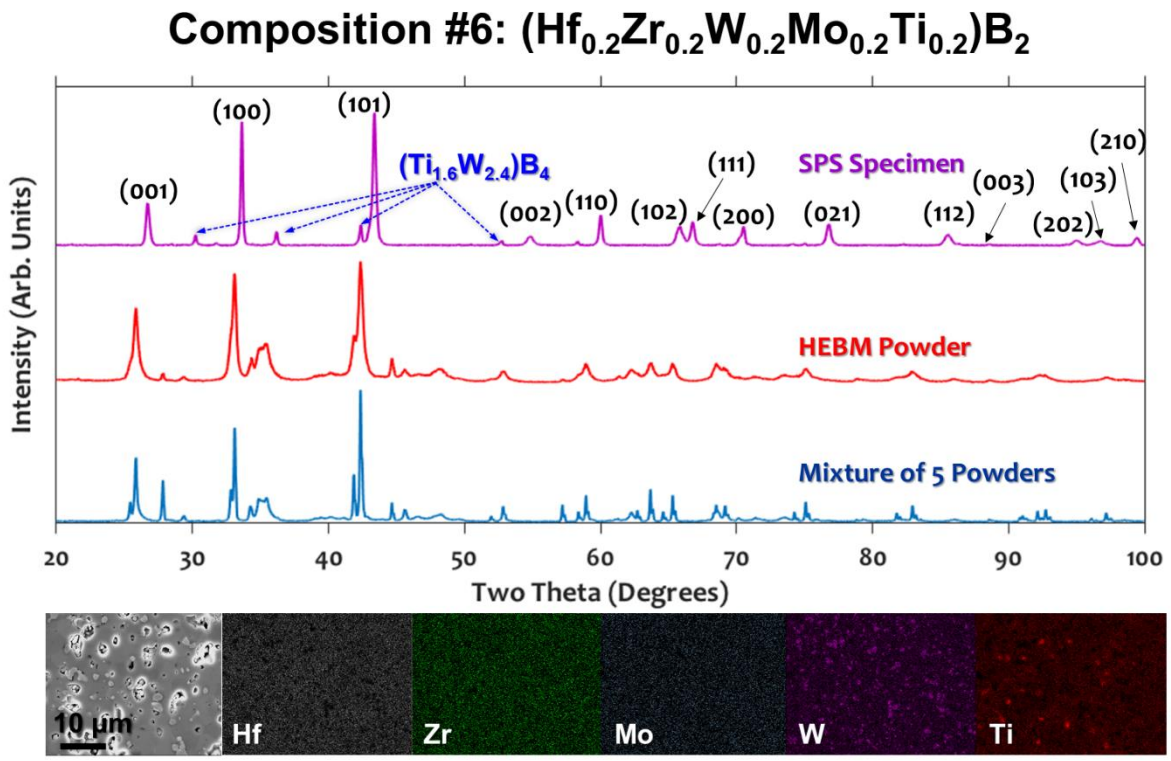

Figure 2.14 Specimen #6 ($Zr_{0.2}Hf_{0.2}W_{0.2}Mo_{0.2}Ti_{0.2})B_2$: **(a)** XRD patterns showing phase evolution during the HEBM-SPS fabrication process. **(b)** Cross-sectional SEM image and the corresponding EDX compositional maps of the specimen after SPS.

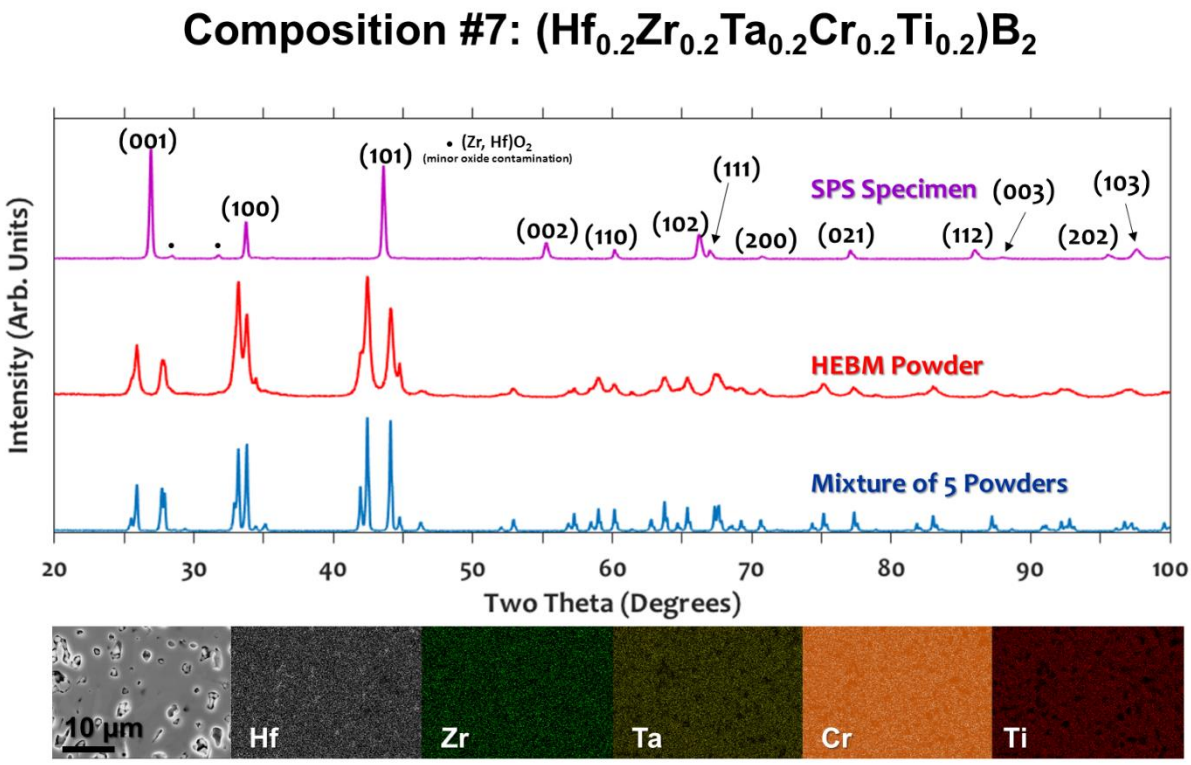

Figure 2.15 Specimen #7 ($Zr_{0.2}Hf_{0.2}Ta_{0.2}Cr_{0.2}Ti_{0.2})B_2$: **(a)** XRD patterns showing phase evolution during the HEBM-SPS fabrication process. **(b)** Cross-sectional SEM image and the corresponding EDX compositional maps of the specimen after SPS.

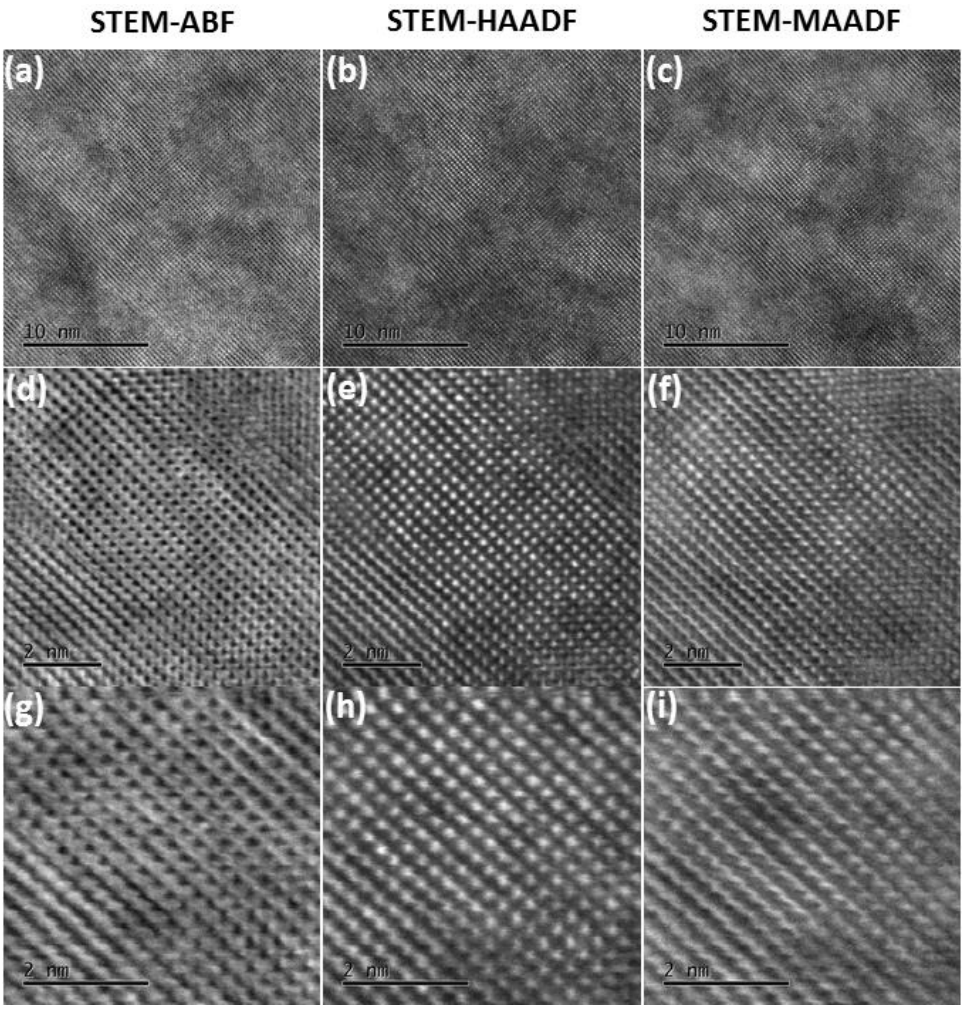

Figure 2.16 STEM images at three different magnifications for Specimen #2 ($Hf_{0.2}Zr_{0.2}Ta_{0.2}Mo_{0.2}Ti_{0.2})B_2$ at a different location in the same specimen shown in Fig. 5. **(a)**, **(d)** and **(g)** are STEM-ABF images; **(b)**, **(e)** and **(h)** are STEM-HAADF images; **(c)**, **(f)** and **(i)** are STEM-MAADF images.

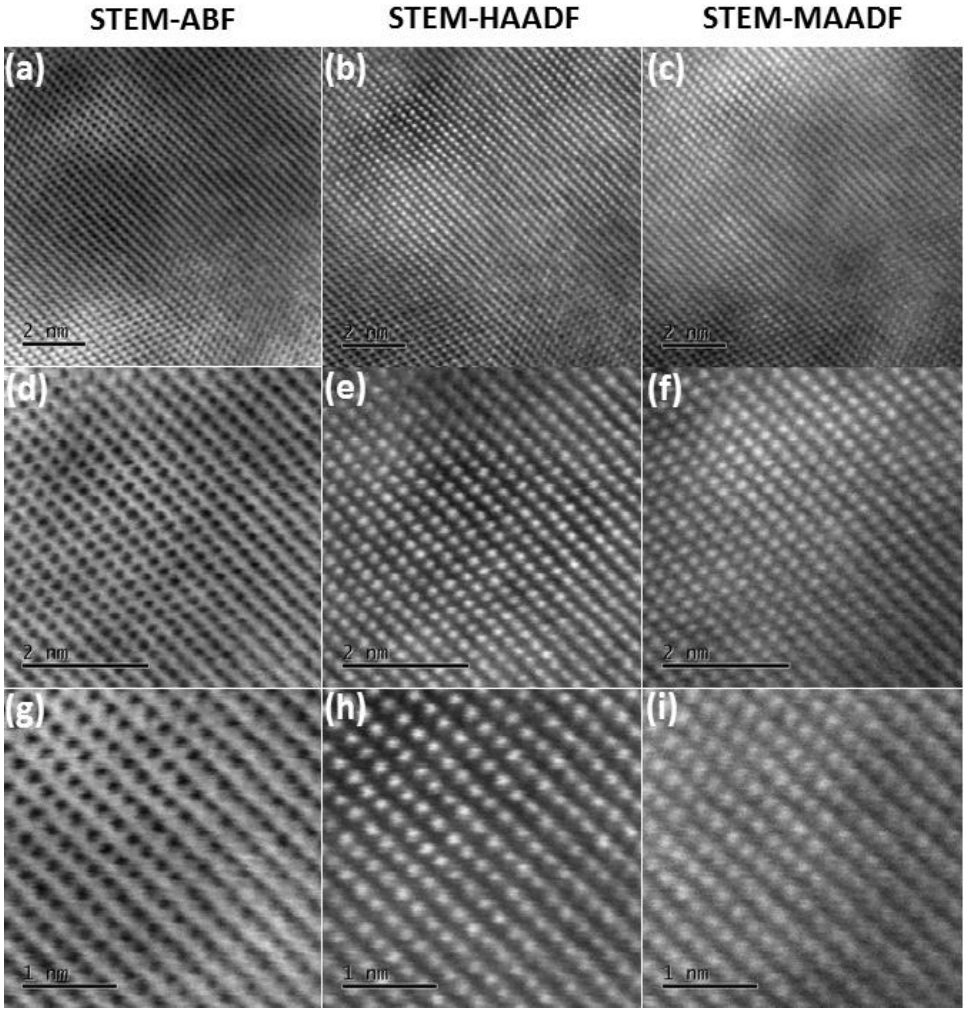

Figure 2.17 STEM images at three different magnifications for Specimen #2 $(Hf_{0.2}Zr_{0.2}Ta_{0.2}Mo_{0.2}Ti_{0.2})B_2$ from a different grain in the same specimen shown in Fig. 5. **(a)**, **(d)** and **(g)** are STEM-ABF images; **(b)**, **(e)** and **(h)** are STEM-HAADF images; **(c)**, **(f)** and **(i)** are STEM-MAADF images.

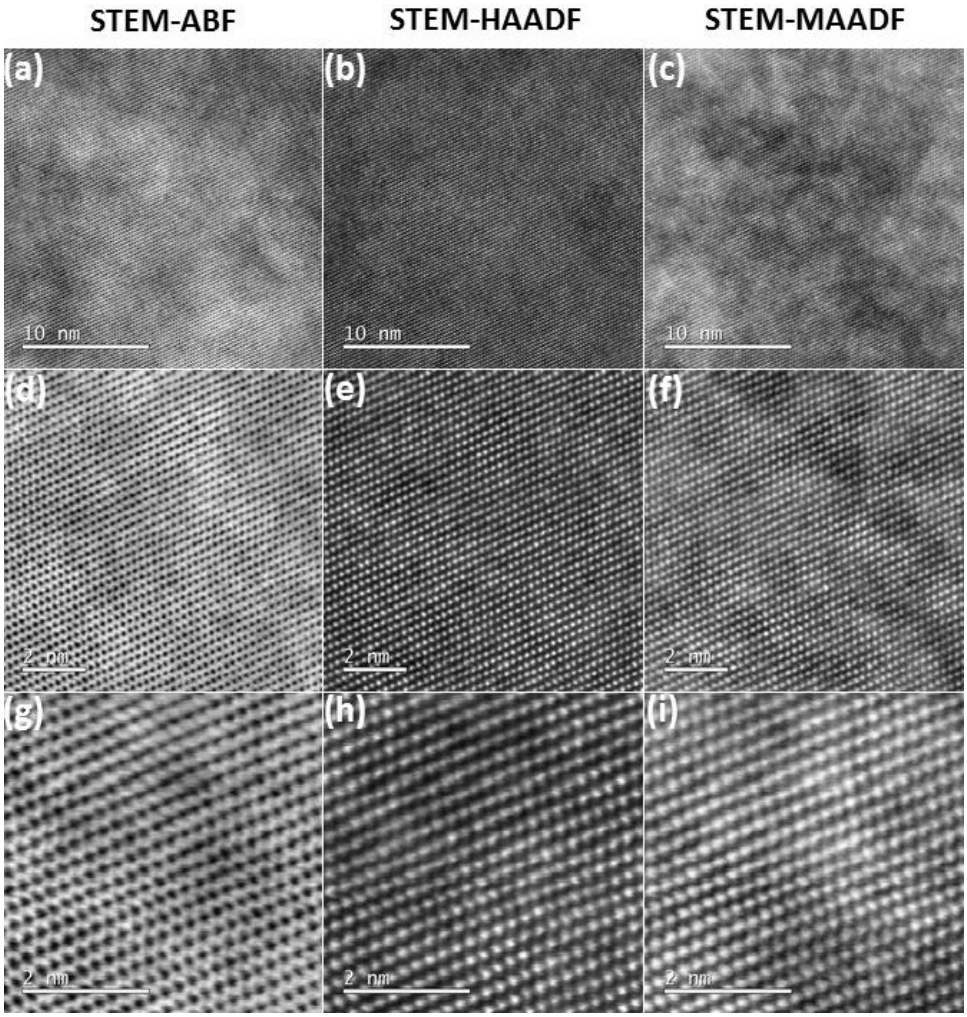

Figure 2.18 STEM images at three different magnifications for Specimen #1 ($Hf_{0.2}Zr_{0.2}Ta_{0.2}Nb_{0.2}Ti_{0.2})B_2$. **(a)**, **(d)** and **(g)** are STEM-ABF images; **(b)**, **(e)** and **(h)** are STEM-HAADF images; **(c)**, **(f)** and **(i)** are STEM-MAADF images.

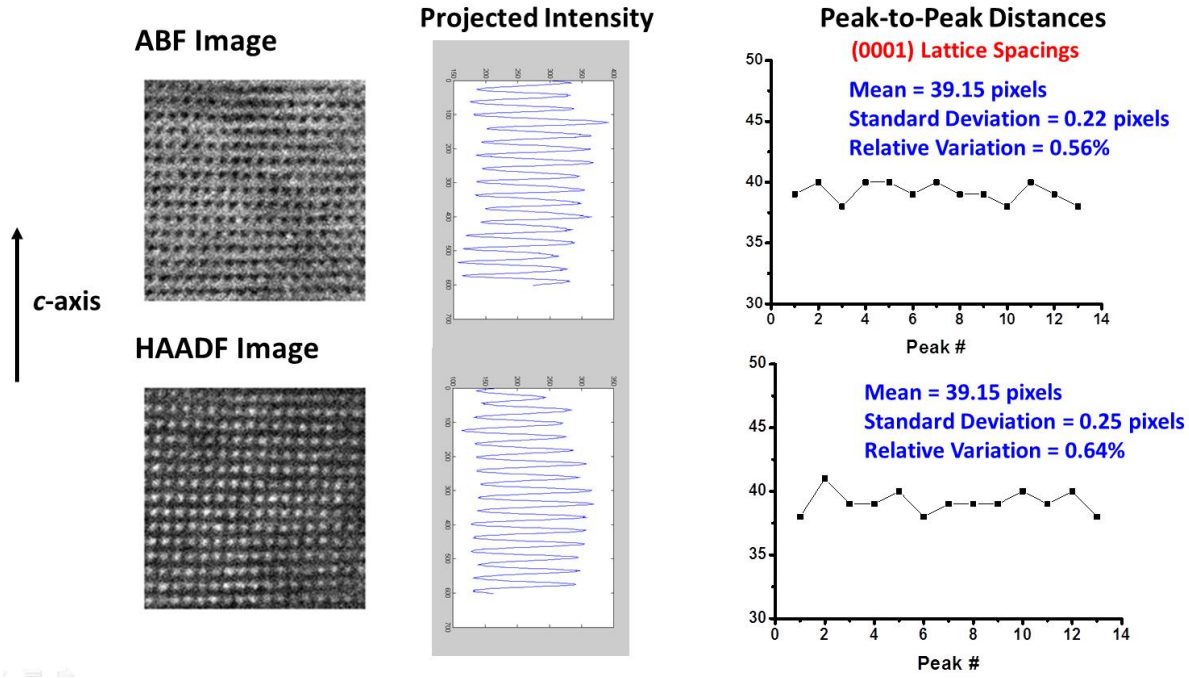

Figure 2.19 Digital analysis of the STEM ADF and HAADF images from Specimen #2 $(Hf_{0.2}Zr_{0.2}Ta_{0.2}Mo_{0.2}Ti_{0.2})B_2$, showing a narrow distribution of measured basal (0001) lattice spacings that is only ~0.6% of the mean, *i.e.*, a standard variation of ~0.02 Å. This result directly confirmed the formation 2-D high-entropy metal layers between the 2-D boron nets without any significant layer-to-layer variation or segregation of different metal atoms in different 2-D metal layers.

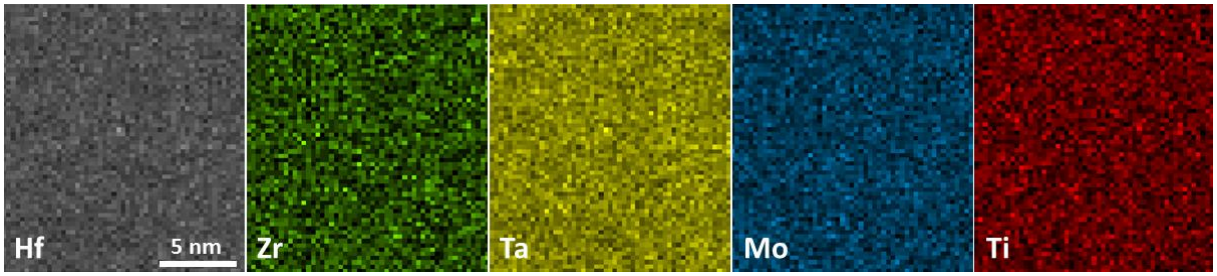

Figure 2.20 Nanoscale EDX compositional maps for Specimen #2 ($Hf_{0.2}Zr_{0.2}Ta_{0.2}Mo_{0.2}Ti_{0.2})B_2$ from a different location in the same specimen shown in Fig. 6, showing the homogeneous chemical distribution at nanoscale.

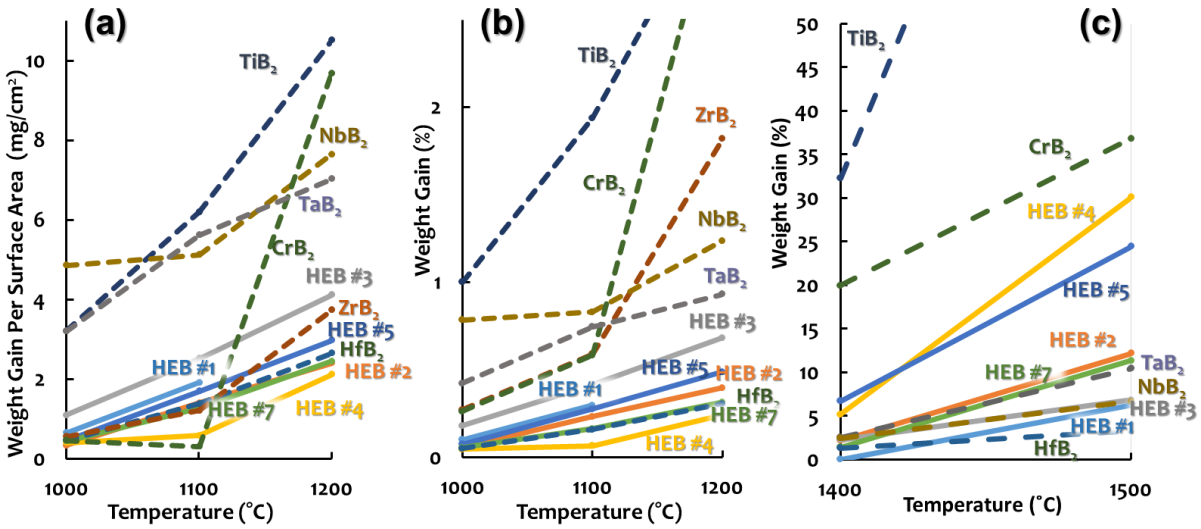

Figure 2.21 (a) Weight gain per surface area and (b) percentage weight gain vs. oxidation temperature curves during isothermal oxidation experiments in flowing dry air at 1000°C, 1100°C, and 1200 °C (for one hour each) sequentially for six single-phase high-entropy metal diborides (*a.k.a.* HEB #1 = $(Hf_{0.2}Zr_{0.2}Ti_{0.2}Nb_{0.2}Ta_{0.2})B_2$, HEB #2 = $(Hf_{0.2}Zr_{0.2}Ti_{0.2}Mo_{0.2}Ta_{0.2})B_2$, HEB #3 = $(Hf_{0.2}Zr_{0.2}Mo_{0.2}Nb_{0.2}Ta_{0.2})B_2$, HEB #4 = $(Hf_{0.2}Mo_{0.2}Ti_{0.2}Nb_{0.2}Ta_{0.2})B_2$, HEB #5 = $(Mo_{0.2}Zr_{0.2}Ti_{0.2}Nb_{0.2}Ta_{0.2})B_2$, and HEB #7 = $(Hf_{0.2}Zr_{0.2}Ti_{0.2}Cr_{0.2}Ta_{0.2})B_2$), along with six individual metal diborides that were fabricated via the same HEBM and SPS route. **(c)** Percentage weight gain vs. oxidation temperature curves during subsequent annealing at 1400 and 1500 °C. Please see the "Methods" section for the detailed experimental procedure. A modified version of panel (b) is also presented in Fig. 8 in the main text. In all , solid lines represent the high-entropy metal diborides and dashed lines represent the conventional (individual) metal diborides made by the same HEBM and SPS route (as the controlled group).

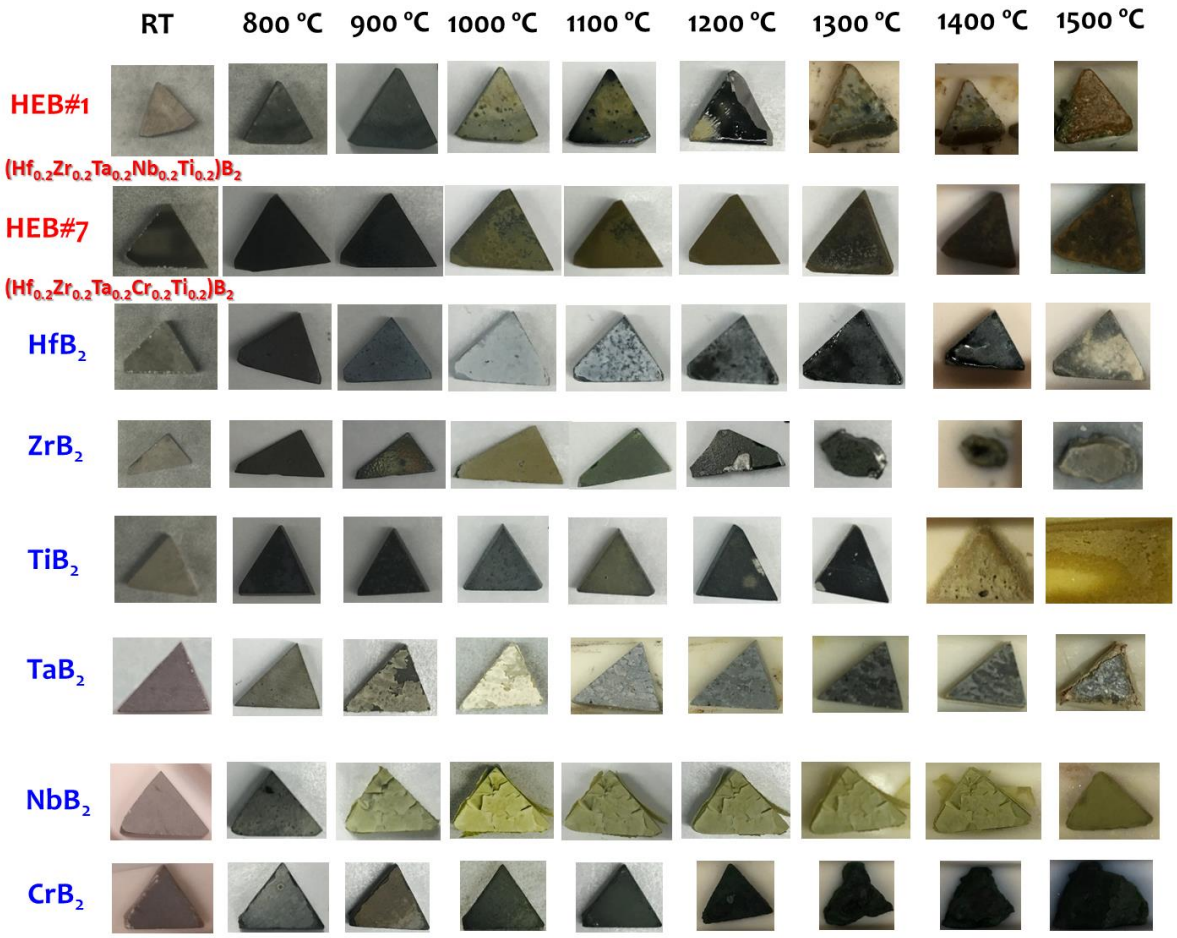

Figure 2.22 Optical images showing the changes of the specimen appearance during a sequential oxidation experiments at 800-1500°C for HEB #1 $(Hf_{0.2}Zr_{0.2}Ti_{0.2}Nb_{0.2}Ta_{0.2})B_2$ and HEB #7 $(Hf_{0.2}Zr_{0.2}Ti_{0.2}Cr_{0.2}Ta_{0.2})B_2$), along with six individual metal diborides that were fabricated via the same HEBM and SPS route. Please see the "Methods" section for the detailed experimental procedure. Both HEB #1 and HEB #7 maintained their shapes up to 1500°C, while most of the six individual metal diborides (except for HfB_2) that were fabricated via the same procedure appeared to be oxidized more severely. At 1500°C, TiB_2 pulverized.

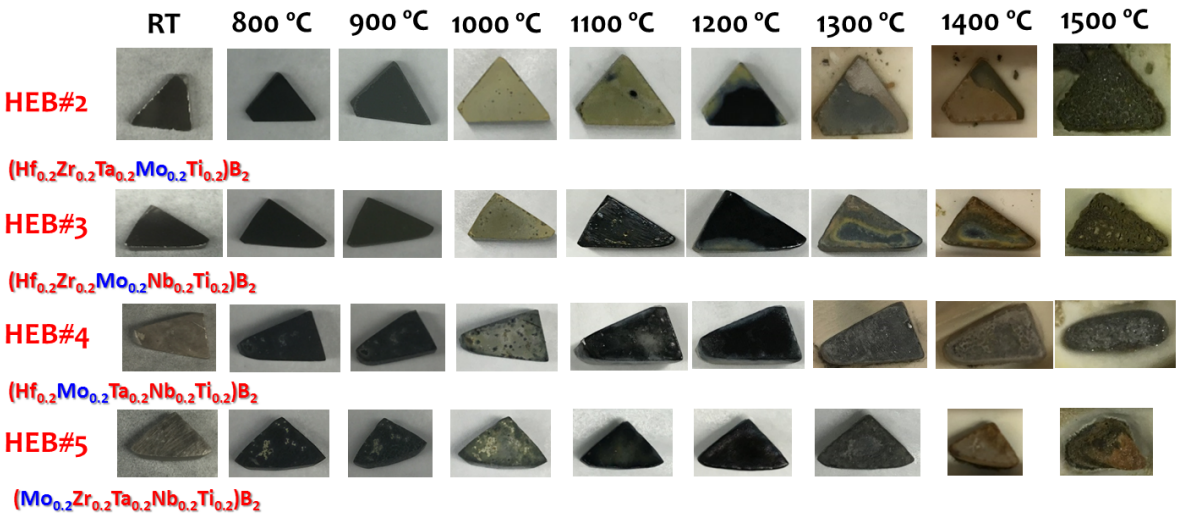

Figure 2.23 Optical images showing the changes of the specimen appearance during a sequential oxidation experiments at 800-1500°C for four MoB_2-containing high-entropy diborides, which exhibited interesting, yet different, oxidation behaviors. Noting that MoO_3 is volatile in this temperature range.

Table 2.1 Summary of the seven metal diboride systems studied. For the lattice parameters (*a* and *c*), the "average" values represent the means of five individual metal diborides while the "XRD" values represent the actual lattice parameters of the high-entropy solutions measured by XRD. See 2.2 for data.

	Composition	**Single Boride Phase?**	δ_a	δ_c	***a* (Å)**		***c* (Å)**		**Relative Density**
					Average	**XRD**	**Average**	**XRD**	
HEB #1	$(Hf_{0.2}Zr_{0.2}Ta_{0.2}Nb_{0.2}Ti_{0.2})B_2$	Yes	1.4 %	3.9 %	3.110	3.101	3.346	3.361	92.4%
HEB #2	$(Hf_{0.2}Zr_{0.2}Ta_{0.2}Mo_{0.2}Ti_{0.2})B_2$	Yes	1.7 %	5.2 %	3.093	3.080	3.307	3.316	92.4%
HEB #3	$(Hf_{0.2}Zr_{0.2}Mo_{0.2}Nb_{0.2}Ti_{0.2})B_2$	Yes	1.7 %	5.2 %	3.101	3.092	3.311	3.345	92.3%
HEB #4	$(Hf_{0.2}Mo_{0.2}Ta_{0.2}Nb_{0.2}Ti_{0.2})B_2$	Yes	1.3 %	4.0 %	3.084	3.082	3.253	3.279	92.2%
HEB #5	$(Mo_{0.2}Zr_{0.2}Ta_{0.2}Nb_{0.2}Ti_{0.2})B_2$	Yes	1.6 %	4.6 %	3.090	3.075	3.265	3.253	92.1%
HEB #6	$(Hf_{0.2}Zr_{0.2}W_{0.2}Mo_{0.2}Ti_{0.2})B_2$	No	2.0 %	6.2 %	3.082	--	3.268	--	--
HEB #7	$(Hf_{0.2}Zr_{0.2}Ta_{0.2}Cr_{0.2}Ti_{0.2})B_2$	Yes	2.3 %	5.2 %	3.081	3.079	3.307	3.336	92.2%

Table 2.2 Summary of key parameters and measured results of the seven high-entropy metal diboride systems studied.

		Single Phase?	δ calculated from				a (Å)		c (Å)		Density (g/cm^3)		Relative Density
	Composition		a_{MB_2} (δ_a)	c_{MB_2} (δ_c)	$r_{metallic}$	$r_{covalent}$	Average	Experiment (XRD)	Average	Experiment (XRD)	Experiment	Theoretical*	
HEB #1	$(Hf_{0.2}Zr_{0.2}Ta_{0.2}Nb_{0.2}Ti_{0.2})B_2$	Yes	1.4 %	3.9 %	4.3 %	3.5 %	3.110	3.101	3.346	3.361	7.71	8.34	92.4%
HEB #2	$(Hf_{0.2}Zr_{0.2}Ta_{0.2}Mo_{0.2}Ti_{0.2})B_2$	Yes	1.7 %	5.2 %	5.4 %	5.1 %	3.093	3.080	3.307	3.316	7.87	8.52	92.4%
HEB #3	$(Hf_{0.2}Zr_{0.2}Mo_{0.2}Nb_{0.2}Ti_{0.2})B_2$	Yes	1.7 %	5.2 %	5.4 %	5.0 %	3.101	3.092	3.311	3.345	6.80	7.37	92.3%
HEB #4	$(Hf_{0.2}Mo_{0.2}Ta_{0.2}Nb_{0.2}Ti_{0.2})B_2$	Yes	1.3 %	4.0 %	4.4 %	4.5 %	3.084	3.082	3.253	3.279	7.99	8.67	92.2%
HEB #5	$(Mo_{0.2}Zr_{0.2}Ta_{0.2}Nb_{0.2}Ti_{0.2})B_2$	Yes	1.6 %	4.6 %	4.6 %	4.5 %	3.090	3.075	3.265	3.253	7.09	7.70	92.1%
HEB #6	$(Hf_{0.2}Zr_{0.2}W_{0.2}Mo_{0.2}Ti_{0.2})B_2$	No	2.0 %	6.2 %	6.2 %	5.1 %	3.082	--	3.268	--	--	--	--
HEB#7	$(Hf_{0.2}Zr_{0.2}Ta_{0.2}Cr_{0.2}Ti_{0.2})B_2$	Yes	2.3 %	5.2 %	7.8 %	8.3 %	3.081	3.079	3.307	3.336	7.36	7.98	92.2%

Note: *Theoretical densities were calculated based on the lattice parameters measured by XRD.

Table 2.3 Summary of lattice parameters of the corresponding individual metal diborides (MB_2) as well as metallic (12-coordinate and at or near ambient temperatures) and covalent radii of different elements. [14,24,25] We do not calculate δ values based on ionic radii, which depend strongly on the valence state (whereas the ionic radii for the M^{2+} in $M^{2+}(B^-)_2$ do not exist for most metals used here; additionally, the M-B bonds also have covalent characteristics and M^{2+} "cations" are highly anisotropic).

Me	a_{MB_2}**(Å)**	c_{MB_2} **(Å)**	$r_{metallic}$ **(Å)**	$r_{covalent}$ **(Å)**
Zr	3.170	3.533	1.60	1.75
Hf	3.139	3.473	1.59	1.75
Nb	3.115	3.265	1.46	1.64
Ta	3.088	3.241	1.46	1.70
Mo	3.041	3.066	1.39	1.54
Ti	3.038	3.220	1.47	1.60
W	3.020	3.050	1.39	1.62
Cr	2.969	3.066	1.28	1.39

Table 2.4 Summary of hardness measurements of six single-phase high-entropy metal diborides, along with six individual metal diborides that were fabricated via the same HEBM and SPS route. MoB_2 is not an equilibrium bulk phase below 1500°C so that we did not have the hardness measurement on it. Thus, the "rule of mixture" averages for HEB#2-HEB#5 were calculated without MoB_2; however, MoB_2 has a lower melting temperature and theoretical hardness than five other metal diborides in question (HfB_2, ZrB_2, TaB_2, NbB_2, and TiB_2); thus, we expect the actual rule-of-mixture averages should be even lower if we could make and test a MoB_2 with the same processing conditions. Noting that the hardness can be affected by porosity and oxide inclusions, which are present in the current case due to the HEBM process that is necessary for mixing uniform high-entropy metal diborides. Thus, we choose to compare the hardness of these high-entropy diborides with individual metal diborides that were fabricated using the same method to allow a fair comparison. We expect that fully-dense and oxide-free metal diborides should have higher hardness than these measured values.

[#]Noting an exception that CrB_2 was sintered at a lower temperature of 1800°C because its intrinsic lower melting (therefore sintering) temperature.

	Relative Density	**Measured Hardness (GPa)**	**Rule of Mixtures**
High-Entropy Borides (HEB):			
HEB #1: $(Hf_{0.2}Zr_{0.2}Ta_{0.2}Nb_{0.2}Ti_{0.2})B_2$	92.4%	17.5 ± 1.2	18.4 ± 1.1 [*]without MoB_2
MoB_2-Containing High-Entropy Diborides:			
HEB #2: $(Hf_{0.2}Zr_{0.2}Ta_{0.2}Mo_{0.2}Ti_{0.2})B_2$	92.4%	19.1 ± 1.8	19.1 ± 1.3[*]
HEB #3: $(Hf_{0.2}Zr_{0.2}Mo_{0.2}Nb_{0.2}Ti_{0.2})B_2$	92.3%	21.9 ± 1.7	18.7 ± 0.7[*]
HEB #4: $(Hf_{0.2}Mo_{0.2}Ta_{0.2}Nb_{0.2}Ti_{0.2})B_2$	92.2%	22.5 ± 1.7	19.2 ± 1.3[*]
HEB #5: $(Mo_{0.2}Zr_{0.2}Ta_{0.2}Nb_{0.2}Ti_{0.2})B_2$	92.1%	23.7 ± 1.7	18.4 ± 1.2[*]
HEB #7: $(Hf_{0.2}Zr_{0.2}Ta_{0.2}Cr_{0.2}Ti_{0.2})B_2$ (overall average)	92.2%	19.9 ± 2.6	18.2 ± 1.2
HEB #7 (less dense region in the center)	>92.2%	21.0 ± 2.8	
HEB #7 (more dense region at the edge)	<92.2%	18.8 ± 1.8	
Individual Metal Diborides (fabricated via the same HEBM and SPS route, using the same parameters[#]):			
HfB_2	~80%	18.6 ± 1.3	
ZrB_2	83.7%	15.4 ± 1.1	
TaB_2	94.8%	17.5 ± 0.8	
NbB_2	96.4%	15.6 ± 0.9	
TiB_2	91.0%	25.0 ± 1.8	
CrB_2[#]	94.8%	14.5 ± 0.7	

References:

[1] Y. Zhang, T.T. Zuo, Z. Tang, M.C. Gao, K.A. Dahmen, P.K. Liaw, Z.P. Lu, Prog. Mater. \ Sci. 61 (2014) 1–93.

[2] M.-H. Tsai, J.-W. Yeh, Mater. Res. Lett. 2 (2014) 107–123.

[3] B. Gludovatz, A. Hohenwarter, D. Catoor, E.H. Chang, E.P. George, R.O. Ritchie, Science 345 (2014) 1153–1158.

[4] A. Poulia, E. Georgatis, A. Lekatou, A.E. Karantzalis, Int. J. Refract. Met. Hard Mater. 57 (2016) 50–63.

[5] É. Fazakas, V. Zadorozhnyy, L.K. Varga, A. Inoue, D.V. Louzguine-Luzgin, F. Tian, L. Vitos, Int. J. Refract. Met. Hard Mater. 47 (2014) 131–138.

[6] O.N. Senkov, J.M. Scott, S.V. Senkova, D.B. Miracle, C.F. Woodward, J. Alloys Compd. 509 (2011) 6043–6048.

[7] M.C. Gao, C.S. Carney, Ö.N. Doğan, P.D. Jablonksi, J.A. Hawk, D.E. Alman, JOM 67 (2015) 2653–2669.

[8] O.N. Senkov, G.B. Wilks, D.B. Miracle, C.P. Chuang, P.K. Liaw, Intermetallics 18 (2010) 1758–1765.

[9] C.M. Rost, E. Sachet, T. Borman, A. Moballegh, E.C. Dickey, D. Hou, J.L. Jones, S. Curtarolo, J.-P. Maria, Nat. Commun. 6 (2015) 8485.

[10] D. Bérardan, S. Franger, D. Dragoe, A.K. Meena, N. Dragoe, Phys. Status Solidi RRL – Rapid Res. Lett. 10 (2016) 328–333.

[11] D. Bérardan, S. Franger, A.K. Meena, N. Dragoe, J. Mater. Chem. A 4 (2016) 9536–9541.

[12] B. Post, F.W. Glaser, D. Moskowitz, Acta Metall. 2 (1954) 20–25.

[13] W.G. Fahrenholtz, G.E. Hilmas, I.G. Talmy, J.A. Zaykoski, J. Am. Ceram. Soc. 90 (2007) 1347–1364.

[14] Y. Zhou, H. Xiang, Z. Feng, Z. Li, J. Mater. Sci. Technol. 31 (2015) 285–294.

[15] V.I. Matkovich, Boron and Refractory Borides, Springer Berlin Heidelberg, Berlin, Heidelberg, 1977.

[16] H. Klesnar, T.L. Aselage, B. Morosin, G.H. Kwei, J. Alloys Compd. 241 (1996) 180–186.

[17] R. Telle, E. Fendler, G. Pettsov, Powder Metall. Met. Ceram. 32 (1993) 240–248.

[18] Y.B. Kuz'ma, V.I. Lakh, B.I. Stadnyk, D.A. Kovalyk, Sov. Powder Metall. Met. Ceram. 9 (1970) 1003–1006.

[19] M. Shibuya, M. Kawata, M. Ohyanagi, Z.A. Munir, J. Am. Ceram. Soc. 86 (2003) 706–10.

[20] G.-J. Zhang, W.-M. Guo, D.-W. Ni, Y.-M. Kan, J. Phys. Conf. Ser. 176 (2009) 012041.

[21] W.G. Fahrenholtz, G.E. Hilmas, Int. Mater. Rev. 57 (2012) 61–72.

[22] W. Fahrenholtz, E. Wuchina, W. Lee, Y. Zhou, eds., Ultra-High Temperature Ceramics: Materials for Extreme Environment Applications, The America Ceramic Society/Wiley, Hoboken, New Jersey, 2014.

[23] W.G. Fahrenholtz, J. Binner, J. Zou, J. Mater. Res. FirstView (2016) 1–16.

[24] N.N. Greenwood, A. Earnshaw, Chemistry of the Elements, 2nd ed., Elsevier, 1997.

[25] B. Cordero, V. Gómez, A.E. Platero-Prats, M. Revés, J. Echeverría, E. Cremades, F. Barragán, S. Alvarez, Dalton Trans. (2008) 2832–2838.

Chapter 3: Reactive flash Spark Plasma Sintering of High-Entropy Ultrahigh Temperature Ceramics

3.1 Introduction

In 2010, Cologna *et al*. originally reported the "flash sintering" of 3 mol. % yttria stabilized zirconia at a low furnace temperature of ~850˚C in just seconds with an applied electric field [1]. Since its inception, flash sintering has been utilized to densify a variety of materials including, but not limited to, ZnO, TiO_2, ZrO_2, and various other ceramics [2–6]. A series of fundamental studies suggested that the flash can start as thermal runaway in many systems and rapid densification rates are related to the ultrafast heating rates in the flash sintering [5,7–10]. Several fundamental scientific questions and related phenomena have been discussed in a recent viewpoint article in *Scripta Materialia* [11]. To date, most flash sintering experiments have been conducted on either "dog-bone" specimens, that lack practicality, or relatively small pellets. The conventional flash sintering is also difficult to apply to more conductive materials. More recently, flash sintering has been realized within spark plasma sintering (SPS) devices. Taking advantage of the large current capability of SPS, this so-called "flash SPS (FSPS)" technique enables the rapid densification of high-temperature and more conductive materials, including TiB_2-BN, B_4C, and SiC [12–15], of larger sizes. Of particular interest to the ultra-high temperature ceramic (UHTC) community is a 2014 study of FSPS of ZrB_2 by Grasso et al., who achieved up to ~95% relative density in 35 s [16].

High-entropy alloys (HEAs) have garnered a great deal of interest in the metallurgical community since their introduction in 2004 by Cantor *et al*. and Yeh *et al*. [17–19]. In 2015, an entropy-stabilized oxide, $(Mg_{0.2}Zn_{0.2}Co_{0.2}Cu_{0.2}Zn_{0.2})O$, was fabricated in bulk form as the ceramic counterpart to HEAs [20]. Since then, high-entropy ceramics have been expanded to

include borides, carbides, silicides, and nitrides, as well as fluorite-structured, perovskite, and spinel oxides [21–28]. Specifically, a class of high-entropy UHTCs, e.g., $(Hf_{0.2}Zr_{0.2}Ta_{0.2}Nb_{0.2}Ti_{0.2})B_2$ and $(Hf_{0.2}Zr_{0.2}Ta_{0.2}Nb_{0.2}Ti_{0.2})C$, have attracted great interest [21,24]. However, the densification and homogenization of high-entropy UHTCs, particularly high-entropy metal diborides, has proved difficult. Specifically, the present author's achieved ~93% density of $(Hf_{0.2}Zr_{0.2}Ta_{0.2}Nb_{0.2}Ti_{0.2})B_2$ via mechanical alloying with the aggressive high-energy ball milling (HEBM) followed by high-temperature SPS for rather long time [24]. Subsequently, self-heating synthesis of $(Hf_{0.2}Zr_{0.2}Ta_{0.2}Nb_{0.2}Ti_{0.2})B_2$ by Tallarita *et al.* [29] led to similar densities while borothermal synthesis by Zhang *et al*. [30] led to higher densities, albeit with significant Nb inhomogeneity.

In this paper, we reported a Reactive Flash Spark Plasma Sintering (ReaFSPS) to synthesize, densify, and homogenize a high-entropy metal diboride, $(Hf_{0.2}Zr_{0.2}Ta_{0.2}Nb_{0.2}Ti_{0.2})B_2$, and a high-entropy metal carbide, $(Hf_{0.2}Zr_{0.2}Ta_{0.2}Nb_{0.2}Ti_{0.2})C$, to high densities in as fast as 120 seconds. This ReaFSPS method combines the conventional FSPS with reactive sintering to synthesize high-entropy ceramics directly from commercial powders of individual components (so that sintering occurs simultaneously with the "reaction" to form and homogenize the high-entropy phase). Notably, we showed that adding minor carbon can enable synthesis and homogenization of the high-entropy metal diboride without aggressive mechanical alloying that could otherwise cause severe contamination and oxidation issues.

3.2 Materials and Methods

3.2.1 Synthesis of High-Entropy Diborides and Carbides

Powders of HfB_2, ZrB_2, NbB_2, TiB_2, HfC, ZrC, NbC, TiC, TaC (99% purity, ≥45 μm; purchased from Alfa Aesar, MA, USA), TaB_2 (99.9% purity, ≥10 μm; purchased from

Goodfellow, PA, USA), and graphitic carbon (99.9% purity, ≥1.2 μm; purchased from US Research Nanomaterials, TX, USA) were utilized as starting materials. Equimolar amounts of the powder, on a metal basis, were measured out and placed into a tungsten carbide planetary mill jar with or without the addition of graphitic carbon. The mixture was milled at 200 rpm for 2 hours in acetone and dried in a rotary evaporator. The planetary milling is much less energetic than the aggressive SPEX HEBM conducted previously for mechanical alloying [24], and it was used here primarily for mixing the powders (without significant mechanical alloying) with little contamination and oxidation.

For FSPS, the samples were pre-sintered into 20 mm disks at 1400˚C for the carbide and 1600˚C for the diboride under 30 MPa of pressure with a heating rate of 200˚C/min for 5 min (SPS, Thermal Technologies, CA, USA). The pre-sintering allowed for very moderate densification of the samples (without forming the high-entropy phase) to lend sufficient strength for subsequent ReaFSPS processing. The relative density after the pre-sintering was ~60% for both the boride and carbide. The 20-mm disk was pressed between two 40-mm plungers with a layer of 5 mm thick graphite felt insulation on the top and bottom to help provide uniform contact between the sample and plungers. A 25-μm thick layer of molybdenum foil (99.95 % purity, Alfa Aesar, MA, USA) was placed between the specimen and the graphite felt to minimize reaction with carbon at high temperatures. A constant low nominal pressure of 5 MPa, relative to the initial sample diameter of 20 mm, was applied and maintained for the entirety of the FSPS experiment. No graphite die was utilized in ReaFSPS, to force the current to pass entirely through the sample. The heating of the sample was dictated by manipulating the output of the electric power supply device as a percentage of the maximum 3000 A available in our SPS equipment. All heating and sintering were performed under vacuum while cooling occurred in an

argon atmosphere. Two sintering parameters were followed for the diboride specimens. The initial samples, hereby referred to as Sample B1 and Sample B2, were heated at 30% power for 120 sec, 50% power for 30 sec, and 100% power for 90 sec. The third sample, B3, was only heated to 30% power for 120 sec. The carbide Sample C1 followed this same low power heating regime used for Sample B3. In all cases, the electric power was increased at a rate of 1% per sec to minimize thermal shock and reduced at 50% per sec for rapid cooling.

3.2.2 Characterization

Densities were calculated from the measured mass and geometric parameters of the pellets. The relative densities were calculated utilizing theoretical densities computed based on an ideal stoichiometry and the lattice parameter measured by X-ray diffraction (XRD). The addition of carbon in the sample reduces the theoretical density to 7.67 g/cm^3 and 8.92 g/cm^3, respectively, for the high-entropy diboride and carbide, respectively, assuming no loss of carbon during the sintering.

All sintered specimens were characterized by X-ray diffraction (XRD) utilizing a Rigaku diffractometer with Cu Kα radiation. Field emission scanning electron microscopy (FE-SEM) images, electron dispersive X-ray spectroscopy (EDS), and electron backscatter diffraction (EBSD) data were collected from specimens utilizing a FEI Apreo scanning electron microscope (SEM) equipped with an Oxford N-Max^N EDX detector and Oxford Symmetry EBSD detector.

3.3 Results and Discussion

3.3.1 Phase Evolution and Formation of High Entropy Phases

The XRD patterns shown in Figure 1 illustrate the formation of a single, hexagonal, diboride phase for Sample B3 and a single, cubic, carbide phase for Sample C1; the formation of

single high-entropy phases as well as the compositional homogeneities in Samples B3 and C1 are further confirmed by EDX data shown in Figure 3. Moderate levels of Nb segregation are observed in both the boride and carbide, similar to our previous work fabricating high-entropy diborides [24]. XRD of the milled powder and pre-sintered specimens are shown in the figures 6-8; the pre-sintered specimens and milled powder possessed multiple diboride and carbide phases after processing.

The formation of single high-entropy UHTC (both diboride and carbide) phases from mixtures of five individual components/phases in ReaFSPS within ~120 seconds is significant. Notably, we used ReaFSPS to successfully fabricate a single-phase and >99% dense (further discussed below) $(Hf_{0.2}Zr_{0.2}Ta_{0.2}Nb_{0.2}Ti_{0.2})B_2$ specimen from a ~60% dense specimen consisting five diboride phases (HfB_2, ZrB_2, NbB_2, TiB_2, and TaB_2) in as short as 120 seconds at a relatively low energy output (900 A). In comparison, previous fabrication of high-entropy diborides has required prolonged heating times, typically ten to twenty minutes at higher SPS power levels, and it must agressive mechanic alloying or utilize special direct synthesis methods [29,30].

An additional interesting, important, and useful finding of this study is the new method to add minor (3 wt. %) carbon to promote the formation and homogenization of the high-entropy metal diboride phase from five individual diboride phases. In fact, our initial comparison study of making diboride specimens, Sample B1 (no C) vs. Sample B3 (3 wt. % C), show that the lack of carbon addition prevented the formation of a single hexagonal high-entropy diboride phase, even at a 3X high power. Here, we propose that the carbon both enhanced the conductivity of the sample and aided in removal of oxygen from the surface of the particles before or during the initial stage of the sintering, allowing for more diffusion along grain boundaries. Consistently,

Gonzalez–Julian *et al*. found that the application of direct current to ZrB_2 in SPS helped the elimination of boron oxide, which allowed for faster diffusion in the sample [31].

We should note that a minor amount of (Hf, Zr)O_2 is observed in both the XRD and SEM, as shown in Figures 1 and 2, despite the addition of carbon. In addition, a small amount of cubic tantalum rich carbide phase, with minor XRD peaks similar to that of $(Hf_{0.2}Zr_{0.2}Ta_{0.2}Nb_{0.2}Ti_{0.2})C$, is present in Samples B2 and B3. This Ta-rich secondary carbide phase is also evident the EDX elemental maps shown in Figure 3. Small amounts of carbide phases are commonly observed in borocarbothermal reduction of metal oxides [32,33].

3.3.2 Densities of Sintered Specimens

Our optimized $(Hf_{0.2}Zr_{0.2}Ta_{0.2}Nb_{0.2}Ti_{0.2})B_2$ specimen made by ReaFSPS, Sample B3, possesses a density of 7.62 g/cm^3 (~99.3%). We should note that the theoretical density does not take into account the small carbide phase present in Sample B3, as well as any possible loss of carbon. Nonetheless, the measured high relative density (<1 % porosity) is consistent with the SEM imaging (Figure 2(c)). The high-entropy carbide Sample C1 has a measured density of 8.14 g/cm^3 (<91.4%), being lower due to excess carbon as well as higher overall porosity, as is shown in Figure 2(d).

3.3.3 Estimation of Temperature during Flash Spark Plasma Sintering

While the temperature of the sample is not measured directly, it can be roughly estimated by the geometry of the sample and the power inputs, with the assumption of the blackbody radiation being the predominant heat loss mechanism at high temperatures. A more detailed explanation of the temperature estimation can be found elsewhere [8]. For ReaFSPS at 100% power, the temperature at the steady-state is estimated to be ~4500˚C – well above the melting

temperature of any of the constituent diborides [34] – though the actual temperature might be lower due to the reaction with graphite (to form at least some liquid that adsorb heat) and extra heat conduction. Strong evidence of melting is indeed observed in Figure 2(b); furthermore, a significant volumetric expansion of the specimen (as shown in the figure 6) indicates a reaction with the carbon environment and further reduces the actual sample temperature compared to the estimation. It is interesting to note that even this high specimen temperature did not homogenize the diboride mixture to form the single-phase high-entropy solid solution without the initial addition of 3 wt. % extra uniformly-distributed carbon in the specimen.

Although such a high temperature (with 100% power) and associated diboride-carbon eutectic reactions are generally undesirable, Figure 2(b) suggests a new possibility of using ReaFSPS to fabricate a unique microstructure with carbon layers at the grain boundaries (via the eutectic liquid formed during ReaFSPS) of high-entropy metal diborides. This offers a novel route to make a unique microstructure (with weak boundaries to deflect cracks). However, much more optimization work must be done to fine control the microstructure to increase the mechanical properties (as the current specimen is too porous).

At 30% current output, the estimated temperature from the steady-state blackbody radiation is ~3300˚C (albeit the actual specimen temperature might be a bit lower), which is near the melting temperature of HfB_2 and ZrB_2. While this estimated temperature is well above the eutectic temperature for group IV diborides and carbon, minimal reactions were observed, likely due to the blocking effects of the molybdenum foil on the sample faces [35,36]. More than 99% relative density has been achieved in Sample B3 with a compositionally-homogenous high-entropy phase and a uniform microstructure (Figure 2(c)).

3.3.4 Electron Backscatter Diffraction

EBSD was utilized to measure the grain size and examine the texture of the sintered $(Hf_{0.2}Zr_{0.2}Ta_{0.2}Nb_{0.2}Ti_{0.2})B_2$ and $(Hf_{0.2}Zr_{0.2}Ta_{0.2}Nb_{0.2}Ti_{0.2})C$ specimens. EBSD maps and their distributions are shown in Figure 4. An average grain sizes of 19.4 ± 11.6 μm and 11.4 ± 5 μm were found for Samples B2 and B3, respectively; the larger grain size in Sample B2 is due to a significantly higher temperature at 100% power. The high-entropy carbide Sample C1 showed a grain size of 5.5 ± 2.0 μm. The smaller grain size of the carbide is likely related to a lower relative density in comparison to the diboride specimens. No significant texturing was evident in any samples.

3.4 Conclusion

In summary, a high-entropy diboride, $(Hf_{0.2}Zr_{0.2}Ta_{0.2}Nb_{0.2}Ti_{0.2})B_2$, and a high-entropy carbide, $(Hf_{0.2}Zr_{0.2}Ta_{0.2}Nb_{0.2}Ti_{0.2})C$, have been successfully sintered and homogenized in 120 seconds with the utilization of ReaFSPS. The formation of single high-entropy phases has been confirmed via a combination of XRD, SEM, EDS, and EBSD. An interesting and useful finding is that the addition of 3 wt. % of carbon can promote the formation and homogenization of a high-entropy diboride phase without aggressive mechanical alloying, to achieve >99% relative density via ReaFSPS, which is otherwise unattainable. This new route can be generally useful for the synthesis and fabrication of high-entropy UHTCs in a short time utilizing commercial powders without the needs of using aggressive mechanical alloying or special powder synthesis methods.

Chapter 3, in part, is a reprint of the material “Reactive flash spark plasma sintering of high-entropy ultrahigh temperature ceramics” as it appears in *Scripta Materialia*. J. Gild, K. Kaufmann, K. Vecchio, J. Luo, Reactive flash spark plasma sintering of high-entropy ultrahigh

temperature ceramics, Scripta Materialia. 170 (2019) 106–110. The dissertation author was the primary investigator and wrote the first draft of manuscript.

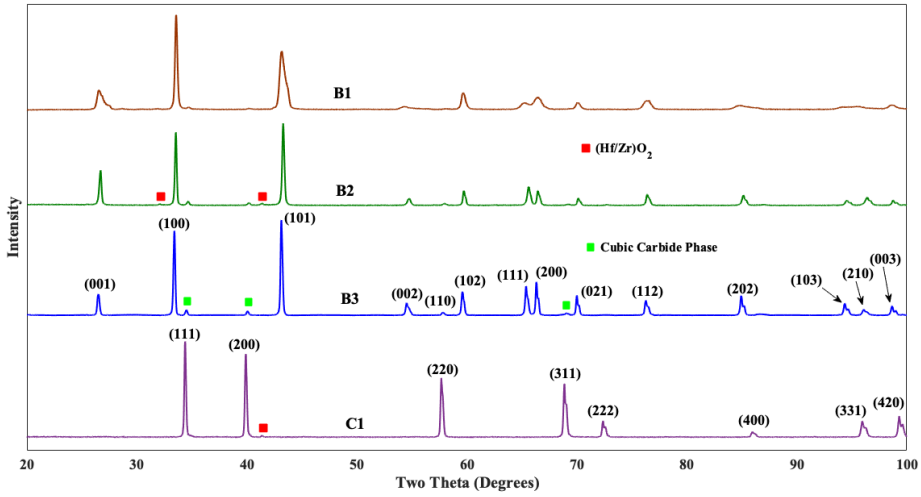

Figure 3.1 Powder XRD of three $(Hf_{0.2}Zr_{0.2}Ta_{0.2}Nb_{0.2}Ti_{0.2})B_2$ specimens (Samples B1, B2, and B3) and one $(Hf_{0.2}Zr_{0.2}Ta_{0.2}Nb_{0.2}Ti_{0.2})C$ specimen (Sample C1) made by ReaFSPS. Sample B1 (no carbon addition, 100% power) contains broad peaks that indicate multiple hexagonal phases, while Sample B2 (3 wt. % C, 100% power) and Sample B3 (3 wt. % C, 30% power) show a single, hexagonal, high-entropy diboride phase. Sample C1 shows a single high-entropy carbide phase of $(Hf_{0.2}Zr_{0.2}Ta_{0.2}Nb_{0.2}Ti_{0.2})C$ (ReaFSPS conditions: 1 wt. % C, 30% power). Minor (Hf, Zr)O_2 peaks are observed for in all samples. A small amount of a high-entropy carbide phase is also present in Samples B2 and B3 due to reactions with graphite.

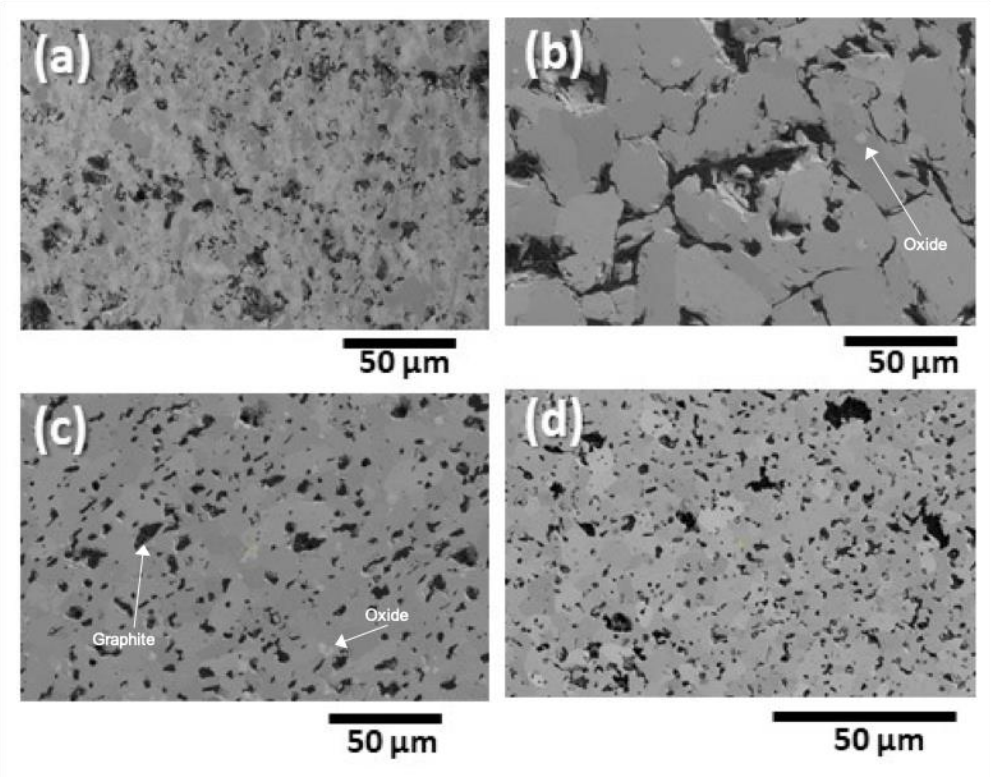

Figure 3.2 SEM micrograph of sintered $(Hf_{0.2}Zr_{0.2}Ta_{0.2}Nb_{0.2}Ti_{0.2})B_2$ (a) Sample B1 (no C, 100% power), (b) Sample B2 (3 wt. % C, 100% power), and (c) Sample B3 (3 wt. % C, 30% power), as well as (d) $(Hf_{0.2}Zr_{0.2}Ta_{0.2}Nb_{0.2}Ti_{0.2})C$ Sample C1 (1 wt. % C, 30% power). The inhomogeneity in Sample B1 is shown in the contrast of part (a), illustrating the necessity of a carbon sintering aid.

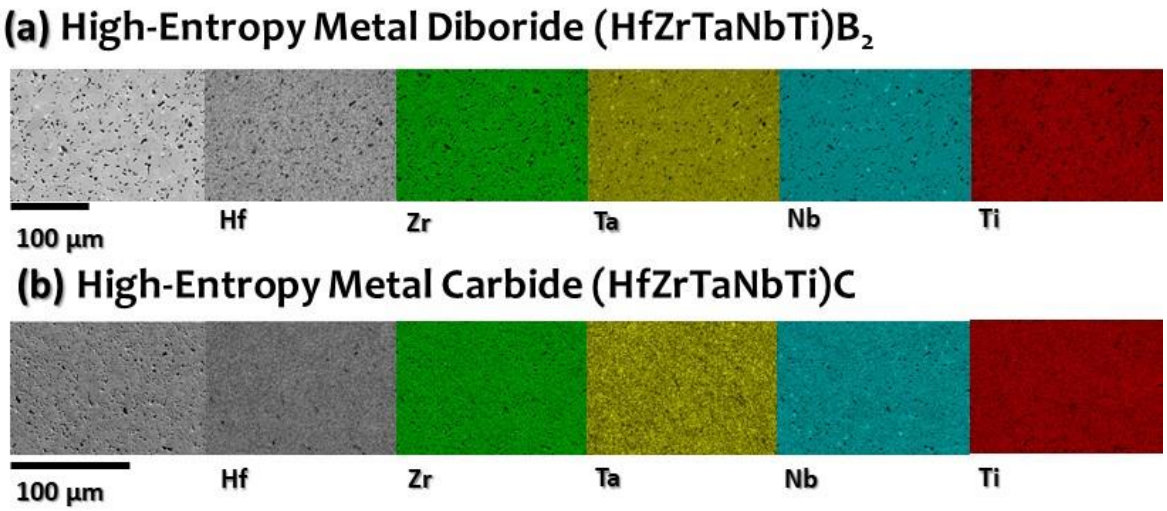

Figure 3.3 SEM micrographs and EDX elemental maps of (a) Sample B3, $(Hf_{0.2}Zr_{0.2}Ta_{0.2}Nb_{0.2}Ti_{0.2})B_2$, and (b) Sample C1, $(Hf_{0.2}Zr_{0.2}Ta_{0.2}Nb_{0.2}Ti_{0.2})C$, fabricated by ReaFSPS.

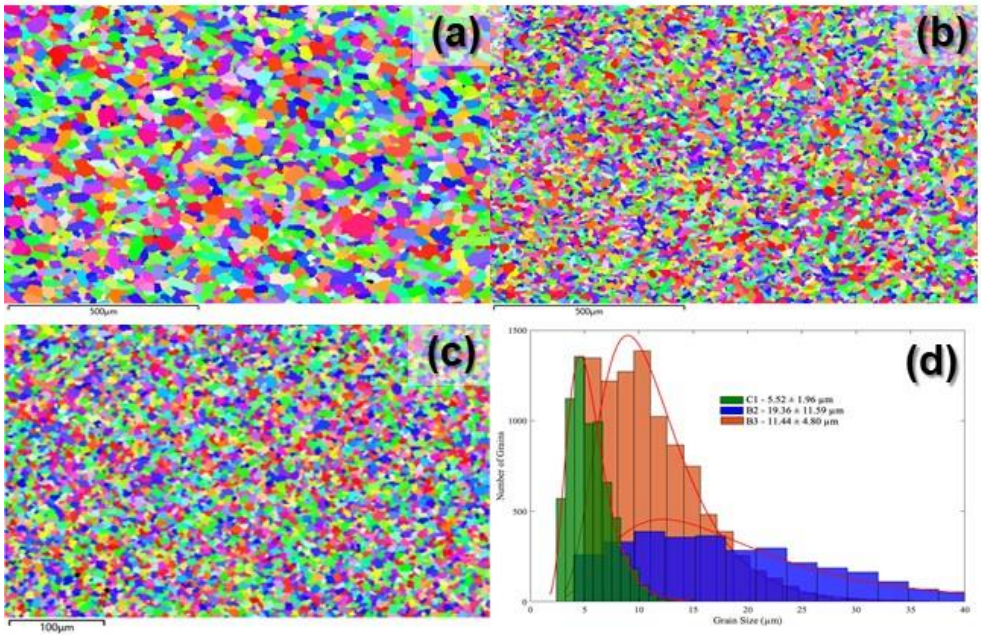

Figure 3.4 EBSD maps of (a) Sample B2, (b) Sample B3, and (c) Sample C1, and (d) grain size distributions for all three single-phase specimens.

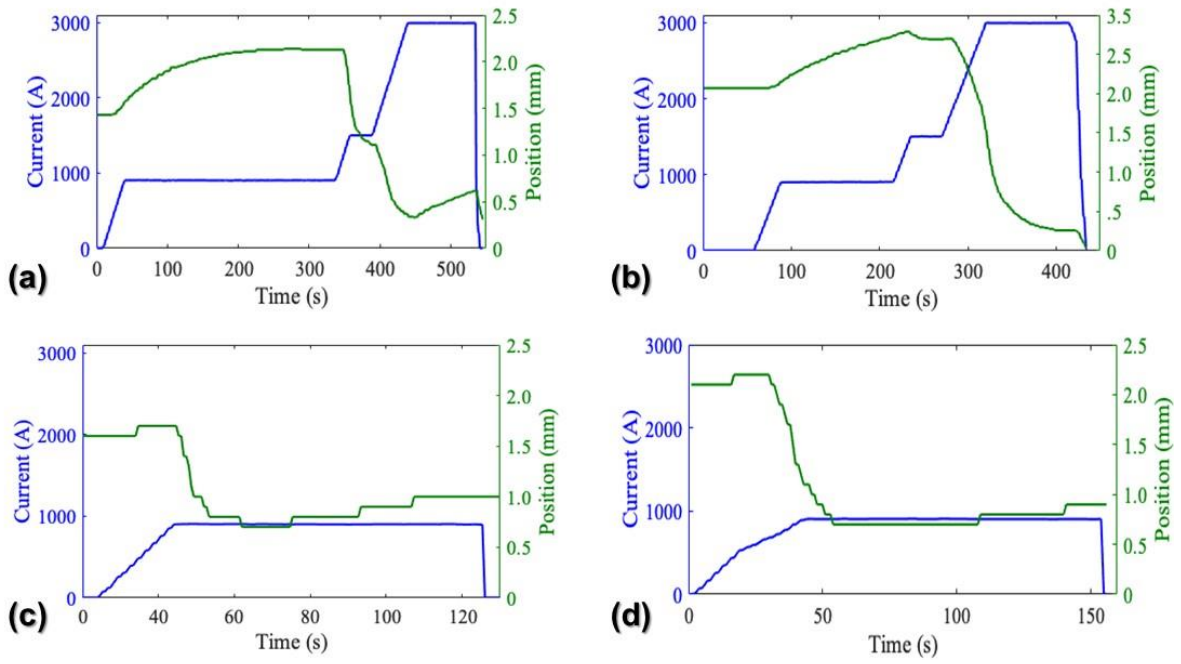

Figure 3.5 Position and current output curves with respect to time during the ReaFSPS of (a) Sample B1, (b) Sample B2, (c) Sample B3, and (d) Sample C1.

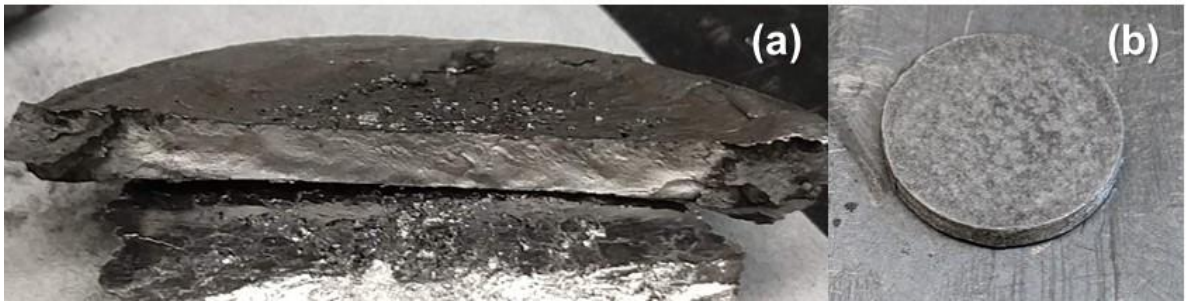

Figure 3.6 $Hf_{0.2}Zr_{0.2}Ta_{0.2}Nb_{0.2}Ti_{0.2})B_2$ + 3 wt. % C specimens fabricated by ReaFSPS using (a) 100% power (Sample B2) (b) 30% power (Sample B3). The darker outside edges indicate high reactivity and melting at high processing temperatures.

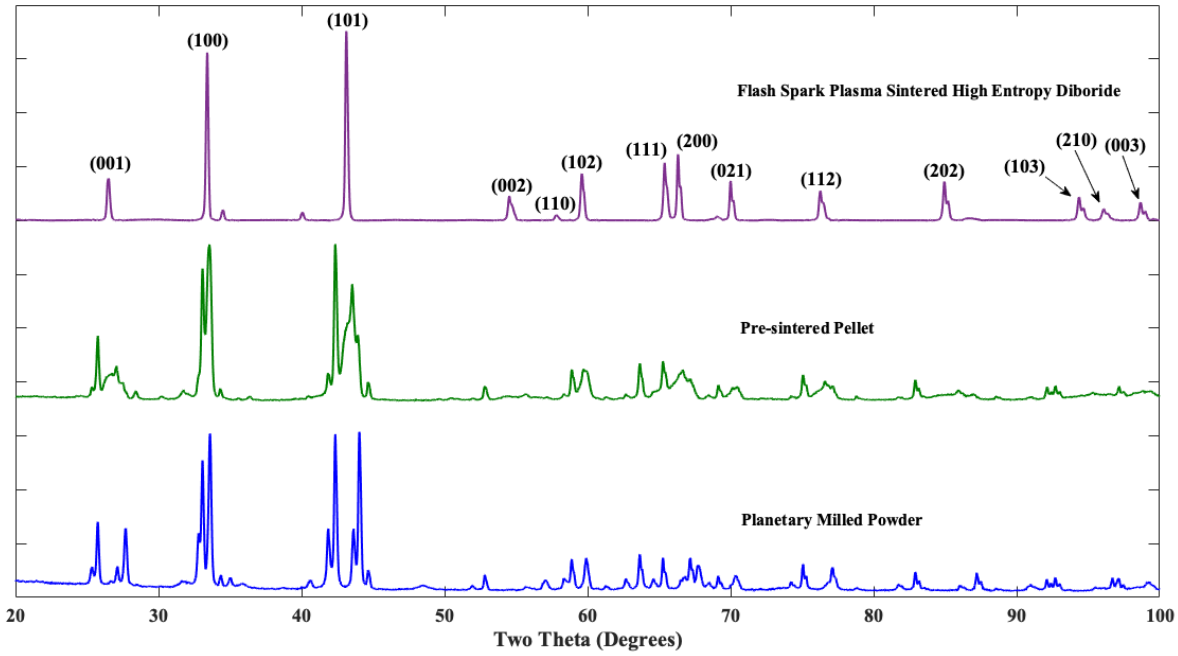

Figure 3.7 Powder XRD of milled diboride powder, the presintered sample (at 1600˚C for 5 min), and $(Hf_{0.2}Zr_{0.2}Ta_{0.2}Nb_{0.2}Ti_{0.2})B_2$ specimen fabricated by ReaFSPS using 30% power.

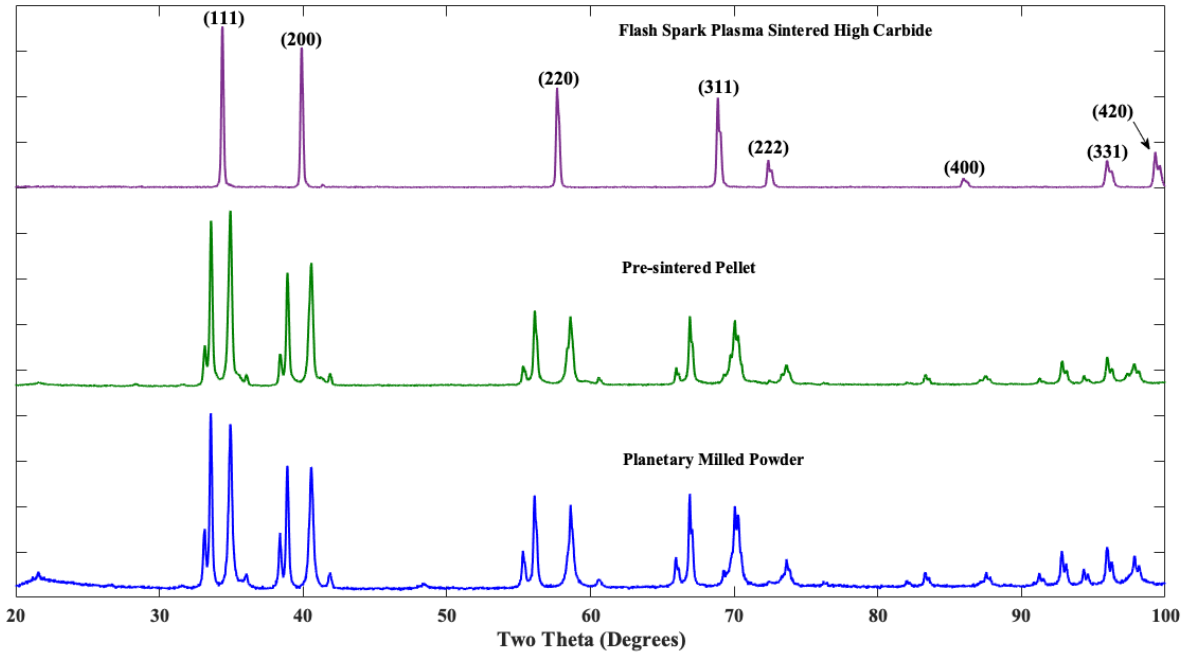

Figure 3.8 Powder XRD of milled carbide powder, the presintered sample (at 1400˚C for 5 min), and $(Hf_{0.2}Zr_{0.2}Ta_{0.2}Nb_{0.2}Ti_{0.2})C$ specimen fabricated by ReaFSPS using 30% power.

Table 3.1 Summary of the nominal composition, ReaFSPS heating scheme, and the sintering aid used for each sample.

Sample ID	**Nominal Composition**	**Sintering Aid**	**Heating Scheme** (heat/ramping rate = 1% per sec for all cases)
B1	$Hf_{0.2}Zr_{0.2}Ta_{0.2}Nb_{0.2}Ti_{0.2})B_2$	No	30% for 120 s + 50% for 30 s + 100% for 90 s
B2		3 wt. % C	
B3		3 wt. % C	30% for 120 s
C1	$(Hf_{0.2}Zr_{0.2}Ta_{0.2}Nb_{0.2}Ti_{0.2})C$	1 wt. % C	

References

[1] M. Cologna, B. Rashkova, R. Raj, J. Am. Ceram. Soc. 93 (2010) 3556–3559.

[2] M. Cologna, J.S.C. Francis, R. Raj, J. Eur. Ceram. Soc. 31 (2011) 2827–2837.

[3] X. Hao, Y. Liu, Z. Wang, J. Qiao, K. Sun, J. Power Sources 210 (2012) 86–91.

[4] Zhang Y., Nie J., Luo J., J. Ceram. Soc. Jpn. 124 (2016) 296–300.

[5] Y. Zhang, J. Nie, J.M. Chan, J. Luo, Acta Mater. 125 (2017) 465–475.

[6] M. Biesuz, V.M. Sglavo, J. Eur. Ceram. Soc. 39 (2019) 115–143.

[7] R.I. Todd, E. Zapata-Solvas, R.S. Bonilla, T. Sneddon, P.R. Wilshaw, J. Eur. Ceram. Soc. 35 (2015) 1865–1877.

[8] Y. Zhang, J.-I. Jung, J. Luo, Acta Mater. 94 (2015) 87–100.

[9] Y. Dong, I.-W. Chen, J. Am. Ceram. Soc. 98 (2015) 3624–3627.

[10] W. Ji, B. Parker, S. Falco, J.Y. Zhang, Z.Y. Fu, R.I. Todd, J. Eur. Ceram. Soc. 37 (2017) 2547–2551.

[11] J. Luo, Scr. Mater. 146 (2018) 260–266.

[12] S. Grasso, T. Saunders, H. Porwal, B. Milsom, A. Tudball, M. Reece, J. Am. Ceram. Soc. 99 (n.d.) 1534–1543.

[13] S. Grasso, E.-Y. Kim, T. Saunders, M. Yu, A. Tudball, S.-H. Choi, M. Reece, Cryst. Growth Des. 16 (2016) 2317–2321.

[14] B. Niu, F. Zhang, J. Zhang, W. Ji, W. Wang, Z. Fu, Scr. Mater. 116 (2016) 127–130.

[15] R. McKinnon, S. Grasso, A. Tudball, M.J. Reece, J. Eur. Ceram. Soc. 37 (2017) 2787 2794.

[16] S. Grasso, T. Saunders, H. Porwal, O. Cedillos-Barraza, D.D. Jayaseelan, W.E. Lee, M.J. Reece, J. Am. Ceram. Soc. 97 (2014) 2405–2408.

[17] B. Cantor, I.T.H. Chang, P. Knight, A.J.B. Vincent, Mater. Sci. Eng. A 375–377 (2004) 213–218.

[18] J.-W. Yeh, S.-J. Lin, T.-S. Chin, J.-Y. Gan, S.-K. Chen, T.-T. Shun, C.-H. Tsau, S.-Y. Chou, Metall. Mater. Trans. A 35 (2004) 2533–2536.

[19] J.-W. Yeh, S.-K. Chen, S.-J. Lin, J.-Y. Gan, T.-S. Chin, T.-T. Shun, C.-H. Tsau, S.-Y. Chang, Adv. Eng. Mater. 6 (2004) 299–303.

[20] C.M. Rost, E. Sachet, T. Borman, A. Moballegh, E.C. Dickey, D. Hou, J.L. Jones, S. Curtarolo, J.-P. Maria, Nat. Commun. 6 (2015) 8485.

[21] T.J. Harrington, J. Gild, P. Sarker, C. Toher, C.M. Rost, O.F. Dippo, C. McElfresh, K. Kaufmann, E. Marin, L. Borowski, P.E. Hopkins, J. Luo, S. Curtarolo, D.W. Brenner, K.S. Vecchio, Acta Mater. 166 (2019) 271–280.

[22] J. Gild, M. Samiee, J.L. Braun, T. Harrington, H. Vega, P.E. Hopkins, K. Vecchio, J. Luo, J. Eur. Ceram. Soc. 38 (2018) 3578–3584.

[23] S. Jiang, T. Hu, J. Gild, N. Zhou, J. Nie, M. Qin, T. Harrington, K. Vecchio, J. Luo, Scr. Mater. 142 (2017) 116–120.

[24] J. Gild, Y. Zhang, T. Harrington, S. Jiang, T. Hu, M.C. Quinn, W.M. Mellor, N. Zhou, K. Vecchio, J. Luo, Sci. Rep. 6 (2016) 37946.

[25] Q.-W. Xing, S.-Q. Xia, X.-H. Yan, Y. Zhang, J. Mater. Res. 33 (2018) 3347–3354.

[26] C.-H. Lai, S.-J. Lin, J.-W. Yeh, S.-Y. Chang, Surf. Coat. Technol. 201 (2006) 3275–3280.

[27] V. Braic, A. Vladescu, M. Balaceanu, C.R. Luculescu, M. Braic, Surf. Coat. Technol. 211 (2012) 117–121.

[28] T. Jin, X. Sang, R.R. Unocic, R.T. Kinch, X. Liu, J. Hu, H. Liu, S. Dai, Adv. Mater. 30 (2018) 1707512.

[29] G. Tallarita, R. Licheri, S. Garroni, R. Orrù, G. Cao, Scr. Mater. 158 (2019) 100–104.

[30] Y. Zhang, W.-M. Guo, Z.-B. Jiang, Q.-Q. Zhu, S.-K. Sun, Y. You, K. Plucknett, H.-T. Lin, Scr. Mater. 164 (2019) 135–139.

[31] J. Gonzalez–Julian, K. Jähnert, K. Speer, L. Liu, J. Räthel, M. Knapp, H. Ehrenberg, M. Bram, O. Guillon, J. Am. Ceram. Soc. 99 (2016) 35–42.

[32] G.-J. Zhang, W.-M. Guo, D.-W. Ni, Y.-M. Kan, J. Phys. Conf. Ser. 176 (2009) 012041.

[33] D.-W. Ni, G.-J. Zhang, Y.-M. Kan, P.-L. Wang, J. Am. Ceram. Soc. 91 (2008) 2709–2712.

[34] W. Fahrenholtz, E. Wuchina, W. Lee, Y. Zhou, eds., Ultra-High Temperature Ceramics: Materials for Extreme Environment Applications, The America Ceramic Society/Wiley, Hoboken, New Jersey, 2014.

[35] E. Rudy, Ternary Phase Equilibria in Transition Metal-Boron-Carbon-Silicon Systems, Air

Force Materials Laboratory, Aerojet-General Corp Sacramento, CA Research Lab, 1966.

[36] Y.V. Levinskii, S.E. Salibekov, M.K. Levinskaya, Sov. Powder Metall. Met. Ceram. 4 (1965) 923–926.

Chapter 4. Borocarbothermal Synthesis of High Entropy Metal Diborides

4.1 Introduction

High-entropy alloys (HEAs), also known as complex concentrated alloys (CCAs), are materials with five or more elements varying concentrations from 5 to 35 at%. The configurational entropy is viewed as most significant when five or more elements are present in equimolar amounts, as to maximize $\Delta S_{mix} = RlnN$ for an N-component system where R is the gas constant. [1–3] The concept has been expanded to that of high entropy ceramics which has come to include diborides, carbides, nitrides, sulfides, as well as fluorite, spinel, rocksalt, magnetoplumbite, and silicate oxides. [4–16] In the ultra-high temperature ceramic (UHTC) community, high entropy diborides and carbides, e.g., $(Hf_{0.2}Zr_{0.2}Ti_{0.2}Ta_{0.2}Nb_{0.2})B_2$ and $(Hf_{0.2}Zr_{0.2}Ti_{0.2}Ta_{0.2}Nb_{0.2})C$, are of particular interest.

In the current author's previous work, we synthesized six single phase, high entropy metal diborides via high energy ball milling of commercial powders and spark plasma sintering [9]. While this procedure allowed for the rapid production of multiple high entropy systems and limited characterization, it left undesirable oxide inclusions as well as a density of ≈93%. The difficulty in producing fully dense monolithic diboride specimens is well noted for two reasons: the strong chemical bonds leading to slow diffusion and oxygen contamination accelerating grain growth at the expense of densification. To avoid these issues, fine powder, preferably submicron, with little oxygen contamination is required to fully densify diboride or the samples can be fabricated via reactive powder or flash spark plasma sintering; Tallartia et al achieved similar densities without the oxide inclusions via self-propagating synthesis of metal and boron powder while the present author's achieved >99% density via reactive flash spark plasma sintering

with]additions of carbon. [17,18] While there is a substantial body of work on the direct synthesis of individual diboride powders, especially ZrB_2, there is limited work in the high entropy diboride field. [19–23] Zhang et al fabricated high entropy powder via borothermal synthesis but their method left significant oxide inclusions in the final sintered specimen; more recently Junfeng et al. fabricated a dense and oxide free high entropy diboride, $(Hf_{0.2}Zr_{0.2}Ti_{0.2}Ta_{0.2}Nb_{0.2})B_2$, via borocarbothermal synthesis and spark plasma sintering. [24,25] In this paper, we examine the borocarbothermal synthesis of fully dense, oxide free, $(Hf_{0.2}Zr_{0.2}Ti_{0.2}Ta_{0.2}Nb_{0.2})B_2$, $(Hf_{0.2}Zr_{0.2}Ti_{0.2}Ta_{0.2}Mo_{0.2})B_2$, $(Hf_{0.2}Zr_{0.2}Ti_{0.2}Ta_{0.2}Cr_{0.2})B_2$, and $(Hf_{0.2}Zr_{0.2}Ti_{0.2}Mo_{0.2}W_{0.2})B_2$.

4.2 Materials and Methods

4.2.1 Borocarbothermal Reduction of Metal Oxides

The raw materials for borocarbothermal synthesis were powders of HfO_2, ZrO_2, Nb_2O_5, Ta_2O_5, TiO_2, MoO_3, WO_3, Cr_2O_3 (≥99% purity; ≤45 μm purchased from Alfa Aesar, MA, USA), B_4C, C (≥99.9% purity; 1-3 μm, 0.4 – 1.2 μm, respectively, purchased from US Research Nanomaterials, TX, USA). Appropriate amounts of five powders were weighed (calculated on a metals basis) according to formulas below. Due to the residual oxide present in boron carbide as well as formation of boron suboxides, excess amount of boron carbide or carbon are necessary in order to fully reduce the metal oxides. [20,22,26,27] The excess amounts used for each composition is given in table 1. Four compositions were examined – $(Hf_{0.2}Zr_{0.2}Ti_{0.2}Ta_{0.2}Nb_{0.2})B_2$, $(Hf_{0.2}Zr_{0.2}Ti_{0.2}Ta_{0.2}Mo_{0.2})B_2$, $(Hf_{0.2}Zr_{0.2}Ti_{0.2}Ta_{0.2}Cr_{0.2})B_2$, and $(Hf_{0.2}Zr_{0.2}Ti_{0.2}Mo_{0.2}W_{0.2})B_2$ according the following equations:

$$2HfO_2 + 2ZrO_2 + 2TiO_2 + Ta_2O_5 + Nb_2O_5 + 3C + 7B_4C \rightarrow$$

$$2(Hf_{0.2}Zr_{0.2}Ti_{0.2}Ta_{0.2}Nb_{0.2})B_2 + 4B_2O_3 + 10CO$$

$$12HfO_2 + 12ZrO_2 + 12TiO_2 + 6Ta_2O_5 + 12MoO_3 + 31C + 41B_4C \rightarrow$$

$$12(Hf_{0.2}Zr_{0.2}Ti_{0.2}Ta_{0.2}Mo_{0.2})B_2 + 22B_2O_3 + 72CO$$

$$24HfO_2 + 24ZrO_2 + 24TiO_2 + 12Ta_2O_5 + 12Cr_2O_3 + 33C + 81B_4C \rightarrow$$

$$24(Hf_{0.2}Zr_{0.2}Ti_{0.2}Ta_{0.2}Cr_{0.2})B_2 + 42B_2O_3 + 114CO$$

$$7HfO_2 + 7ZrO_2 + 7TiO_2 + 7MoO_3 + 7WO_3 + 27B_4C \rightarrow$$

$$7(Hf_{0.2}Zr_{0.2}Ti_{0.2}Mo_{0.2}W_{0.2})B_2 + 19B_2O_3 + 27CO$$

Due to the formation of boron suboxides such as BO, B_2O_2, and others, an excess amount of boron carbide is necessary in order to fully reduce the oxides and form a pure diboride phase. The excess amounts of boron carbide necessary was found to be dependent upon the composition of the diboride and the values are all given in table 1. Carbon was not used as a precursor in the tungsten containing sample due to the high stability of WC relative to the diboride structure.

For borocarbothermal synthesis, the mixture of five metal oxide powders were initially milled for 48 hours in zirconia jars at 200rpm in acetone with YSZ media. The milled oxides, boron carbide, and graphite were planetary milled for 2 hours at 200 rpm in acetone in polytetrafluoroethylene (PTFE) jars for YSZ media. The powder was then dried in a rotary evaporator after both milling steps. The powder mixture was then lightly pressed into 25 mm pellets to ensure good contact of the particles in the powder. The pellets were loaded into a graphite furnace (Red Devil, RDWebb, Natick, MA, USA) that was pumped down to 1×10^{-1} bar and backfilled with argon thrice before a turbomolecular pump was engaged to pump down to 1×10^{-4} bar. The furnace, while under vacuum, was heated to 1475˚C at a rate of 10˚C/min, held at

1475˚C for 15 minutes to allow for calibration of the pyrometer, and heated to 1550˚C at a rate of 5˚C/min. It was held at 1550˚C for 90 minutes to allow for the evaporation of boron oxide and allowed to cool naturally. Upon removal from the furnace, the powder was immediately quenched in liquid nitrogen to prevent oxygen contamination and moved into an argon glovebox. All SPS dies with this powder were assembled in the glovebox to prevent oxidation of the powder.

The powders were then densified into 20-mm diameter disks via spark plasma sintering (SPS, Thermal Technologies, CA, USA) at 2000˚C for 30 minutes under an initial uniaxial pressure of 80 MPa, which was lowered to 30 MPA after 5 minutes at 2000˚C to prevent creep of the graphite tooling, with a heating ramping rate of 100˚C/min. The chamber was initially pumped down to vacuum of at least 2 x 10^{-2} Torr prior to the SPS experiments and backfilled with argon gas twice to minimize oxygen contamination from the chamber; the run was performed under vacuum until 2000˚C when argon was flown. The graphite die was lined with 125 μm thick graphite paper to prevent reaction of the specimen with the die. Upon completion, the samples were allowed to cool in an uncontrolled manner in the SPS.

4.2.2 Characterization

Densities were calculated from the measured mass and geometric parameters of the pellets. The relative densities were calculated utilizing theoretical densities computed based on an ideal stoichiometry and the lattice parameter measured by X-ray diffraction (XRD).

All sintered specimens were characterized by X-ray diffraction (XRD) utilizing a Rigaku diffractometer with Cu Kα radiation. Field emission scanning electron microscopy (FE-SEM) images, electron dispersive X-ray spectroscopy (EDS), and electron backscatter diffraction

(EBSD) data were collected from specimens utilizing a FEI Apreo scanning electron microscope (SEM) equipped with an Oxford N-Max^N EDX detector and Oxford Symmetry electron backscatter diffraction (EBSD) detector.

Vicker's hardness measurements were performed on all compositions. Hardness measurements were performed with a Vickers' diamond indenter at 200 gf/mm^2 with a hold time of 15 s. The indentations were examined for conformation with the standard ASTM C1327. The indentations averaged 20–25 μm in width during the testing. Twenty-five measurements were performed at different locations of each specimen; the mean and standard deviation are reported.

4.3 Results and Discussion

4.3.1 Borocarbothermal Synthesis Powder Morphology

The XRD of the diboride powder post synthesis shows the presence of multiple diboride phases with broad peaks as is seen in Fig 1a. This is to be expected as the temperatures of the synthesis are not sufficient to allow for the formation of a single high entropy diboride phase and the lattice parameters of the individual diborides are similar enough that multiple phases can manifest as peak broadening for polydisperse particle size powder. No refractory metal oxide peaks nor boron carbide peaks were observed in XRD. SEM characterization of the powder showed particle size between 200 and 500 nm, shown in Fig 1b. The oxygen content of the powder was not measured due to its strong reactivity with air and water.

4.3.2 Phase formation and compositional uniformity

The XRD patterns of $(Hf_{0.2}Zr_{0.2}Ti_{0.2}Ta_{0.2}Nb_{0.2})B_2$, $(Hf_{0.2}Zr_{0.2}Ti_{0.2}Ta_{0.2}Mo_{0.2})B_2$, and $(Hf_{0.2}Zr_{0.2}Ti_{0.2}Ta_{0.2}Cr_{0.2})B_2$ showed single, hexagonal, diboride phase for all compositions examined and are shown in Fig 2. EDX confirms elemental conformity of all compositions in Fig

3, notably more homogenous than our previous work as well as recent work by Zhang et. al. It should be noted we did not observe any residual hafnium or zirconium oxide secondary phases which were prevalent in their work [25,28]. Similar results were observed by Tallarita et al with powder produced via self-heating synthesis and subsequent densification via spark plasma sintering but they only achieved 92.5% relative density. [18] The lattice parameters of the specimens are given in Table 1.

$(Hf_{0.2}Zr_{0.2}Ti_{0.2}Mo_{0.2}W_{0.2})$ formed a mixture of a high entropy diboride structure and a molybdenum and tungsten rich tetraboride of the CrB structure type, space group Cmcm. This is the same secondary crystal structure we previously observed in $(Hf_{0.2}Zr_{0.2}Ti_{0.2}Mo_{0.2}W_{0.2})B_2$ fabricated from commercial powders including W_2B_5, though with much finer dispersion than was observed in the commercial powder. This same structure has been observed experimentally and found to be favorable via DFT for multiple refractory elements. [29,30] Interestingly, the phase was predominately rich in Ti and W in our previous work - corresponding to the $(Ti_{1.6}W_{2.4})B_4$ phase - whereas in the current work, it is principally rich in Mo and W, though a significant amount of Ti is still dispersed into the phase. Given that molybdenum has been found to be soluble into the WB_4 phase in previous work up to 50 atomic percent, it is expected here that high solubility into the tetraboride phase is observed. [30]

4.3.3 Density

Samples sintered from borocarbothermal synthesis powder possessed superior density compared to our previous work – 98-100% versus 93% in the case of $(Hf_{0.2}Zr_{0.2}Ti_{0.2}Ta_{0.2}Nb_{0.2})B_2$. Similar density differences are observed for $(Hf_{0.2}Zr_{0.2}Ti_{0.2}Ta_{0.2}Mo_{0.2})B_2$, $(Hf_{0.2}Zr_{0.2}Ti_{0.2}Ta_{0.2}Cr_{0.2})B_2$, and $(Hf_{0.2}Zr_{0.2}Ti_{0.2}Mo_{0.2}W_{0.2})B_2$.

4.3.4 Hardness Data

The measured Vicker's hardness values of the diborides specimens are given in table 1. $(Hf_{0.2}Zr_{0.2}Ti_{0.2}Ta_{0.2}Nb_{0.2})B_2$ possesses significantly lower values of hardness, 20.5 ± 1.0 GPa, than the other compositions which are 24.9 ± 1.0 GPa. These values are similar to that of ZrB_2, HfB_2, and TiB_2 composites reported in literature but superior to that of CrB_2. They are notably higher, however, than our previous results for the compositions from samples made via mechanical alloying and spark plasma sintering. [31–34] The two phase composition, $(Hf_{0.2}Zr_{0.2}Ti_{0.2}Mo_{0.2}W_{0.2})B_2$, showed higher hardness of 29.4 ± 1.7 GPa. An increased value of hardness is not surprising for a composition containing a tungsten rich boride phase, as tungsten tetraborides have been examined as materials for ultra-hard ceramic applications. [35,36]

4.3.5 Electron Backscatter Diffraction

EBSD was utilized to measure the grain size and examine the texture of the sintered single phase specimens. EBSD maps and their distributions are shown in Fig. 4. An average grain size of 3.4 ± 1.3 μm for $(Hf_{0.2}Zr_{0.2}Ti_{0.2}Ta_{0.2}Nb_{0.2})B_2$, 6.8 ± 4.0 μm for $(Hf_{0.2}Zr_{0.2}Ti_{0.2}Ta_{0.2}Mo_{0.2})B_2$, 4.5 ± 1.9 μm for $(Hf_{0.2}Zr_{0.2}Ti_{0.2}Ta_{0.2}Cr_{0.2})B_2$, and 4.3 ± 1.8 μm for $(Hf_{0.2}Zr_{0.2}Ti_{0.2}Mo_{0.2}W_{0.2})B_2$. The tetraboride phase was found to be approximately 10% of the sample via EBSD. The grain sizes of $(Hf_{0.2}Zr_{0.2}Ti_{0.2}Ta_{0.2}Nb_{0.2})B_2$ are similar to those observed by Junfeng et al for the same composition post SPS at 2000˚C. [24] No significant texturing was evident in any samples.

4.4 Conclusion

Four high entropy diboride compositions, $(Hf_{0.2}Zr_{0.2}Ti_{0.2}Ta_{0.2}Nb_{0.2})B_2$, $(Hf_{0.2}Zr_{0.2}Ti_{0.2}Ta_{0.2}Mo_{0.2})B_2$, $(Hf_{0.2}Zr_{0.2}Ti_{0.2}Ta_{0.2}Cr_{0.2})B_2$, and $(Hf_{0.2}Zr_{0.2}Ti_{0.2}Mo_{0.2}W_{0.2})B_2$ have

been synthesized and densified via borocarbothermal reduction of metal oxide powders and subsequent spark plasma sintering. The samples show significantly higher density, hardness, and thermal conductivity than the samples fabricated via high energy ball milling and spark plasma sintering in the present author's previous work. The presence of a secondary tetraboride phase in $(Hf_{0.2}Zr_{0.2}Ti_{0.2}Mo_{0.2}W_{0.2})B_2$ is observed to significantly increase hardness compared to other high entropy diborides. This method is a very promising route for the fabrication of high entropy diborides and multi-phase high hardness boride structures.

Chapter 4, in full, is currently in preparation for submission for publication "Borocarbothermal Synthesis of High Entropy Metal Diborides", J. Gild, A. Wright, K. Tomko, M. Qin, B. Bloomfield, D. Martinez, T. Harrington, K. Vecchio, P. Hopkins, J. Luo. The dissertation author was the primary investigator and wrote the first draft of manuscript.

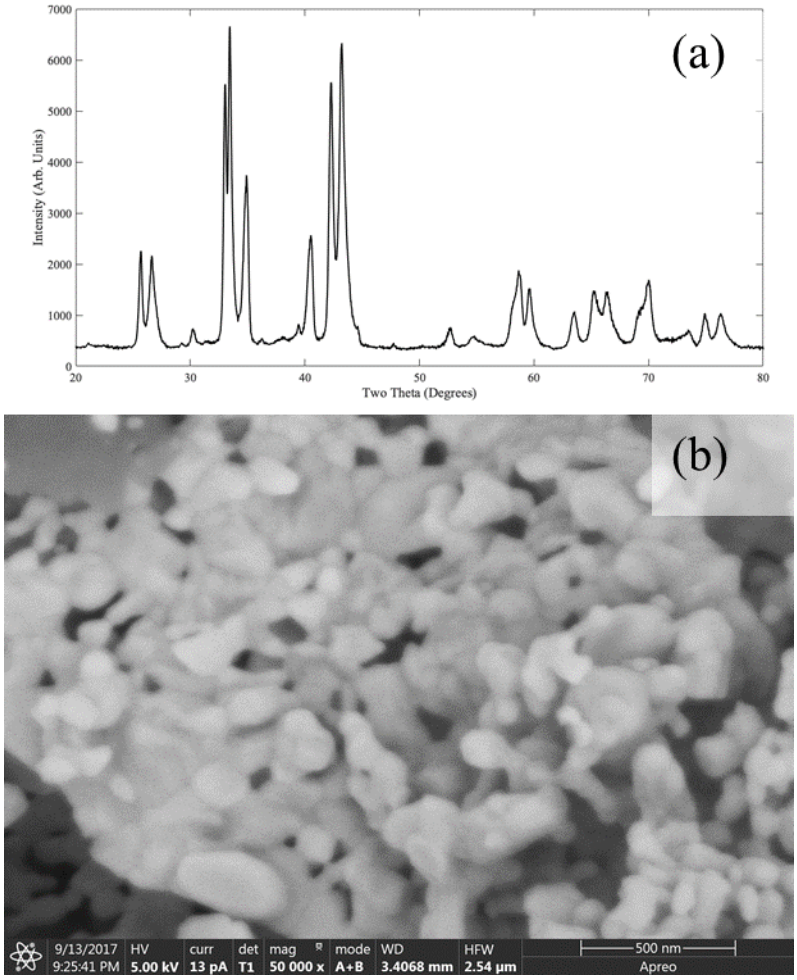

Figure 4.1 (a) XRD of $(Hf_{0.2}Zr_{0.2}Ti_{0.2}Ta_{0.2}Nb_{0.2})B_2$ powder, showing multiple phases and (b) SEM image of diboride powder post synthesis.

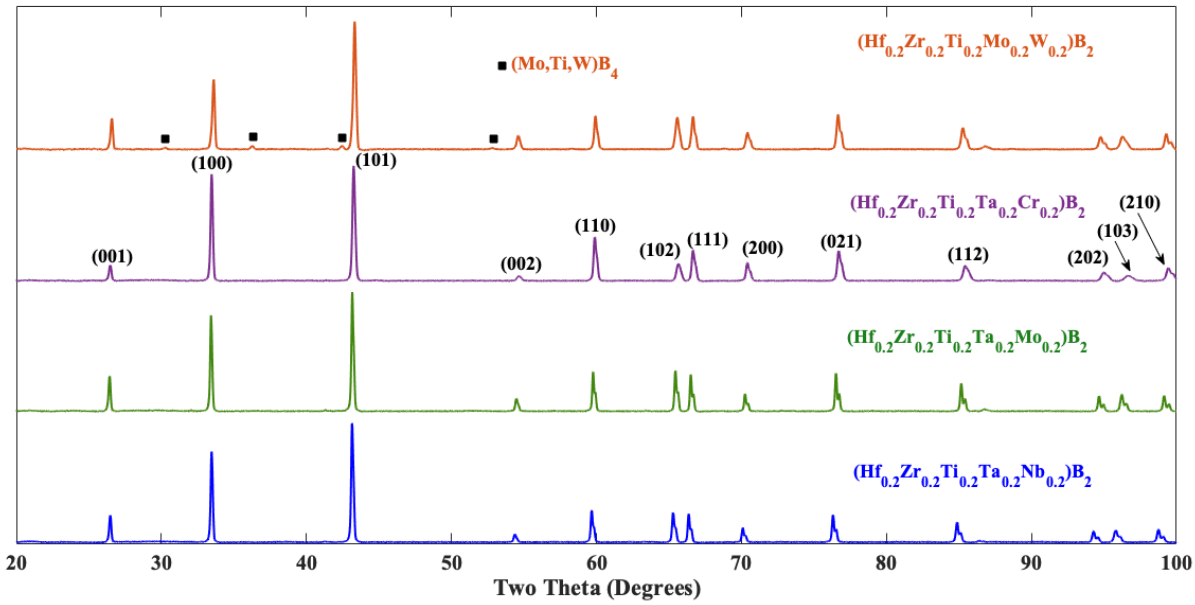

Figure 4.2 XRD patterns of the four high entropy diboride specimens with three of them, $(Hf_{0.2}Zr_{0.2}Ti_{0.2}Ta_{0.2}Nb_{0.2})B_2$, $(Hf_{0.2}Zr_{0.2}Ti_{0.2}Ta_{0.2}Mo_{0.2})B_2$, and $(Hf_{0.2}Zr_{0.2}Ti_{0.2}Ta_{0.2}Cr_{0.2})B_2$ showing a single phase. $(Hf_{0.2}Zr_{0.2}Ti_{0.2}Mo_{0.2}W_{0.2})B_2$ shows a minor $(Mo,Ti,W)B_4$ secondary phase.

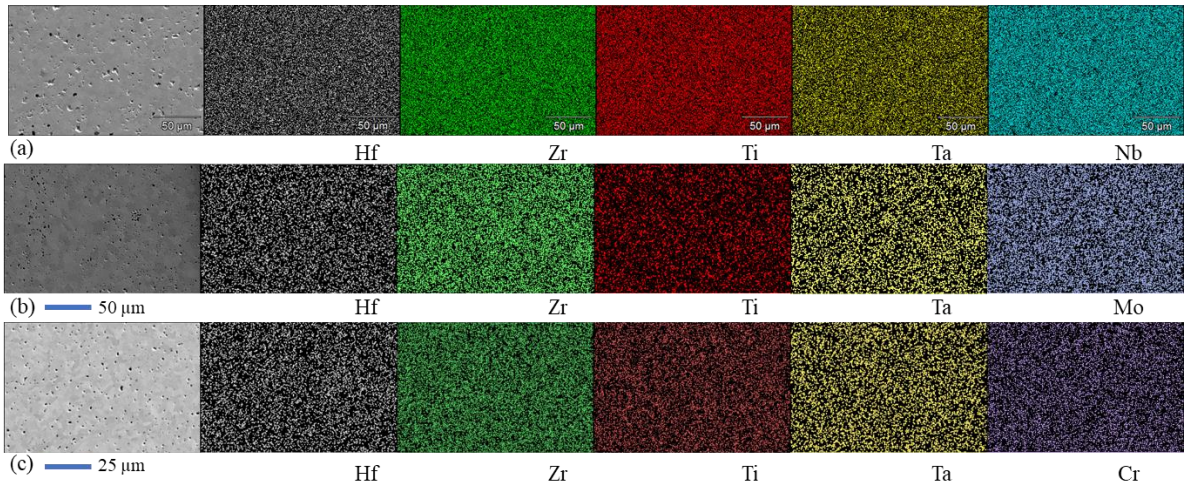

Figure 4.3 Cross-section SEM images and the corresponding EDS composition maps of the single phase diborides, (a) $(Hf_{0.2}Zr_{0.2}Ti_{0.2}Ta_{0.2}Nb_{0.2})B_2$, (b) $(Hf_{0.2}Zr_{0.2}Ti_{0.2}Ta_{0.2}Mo_{0.2})B_2$, (c) $(Hf_{0.2}Zr_{0.2}Ti_{0.2}Ta_{0.2}Cr_{0.2})B_2$

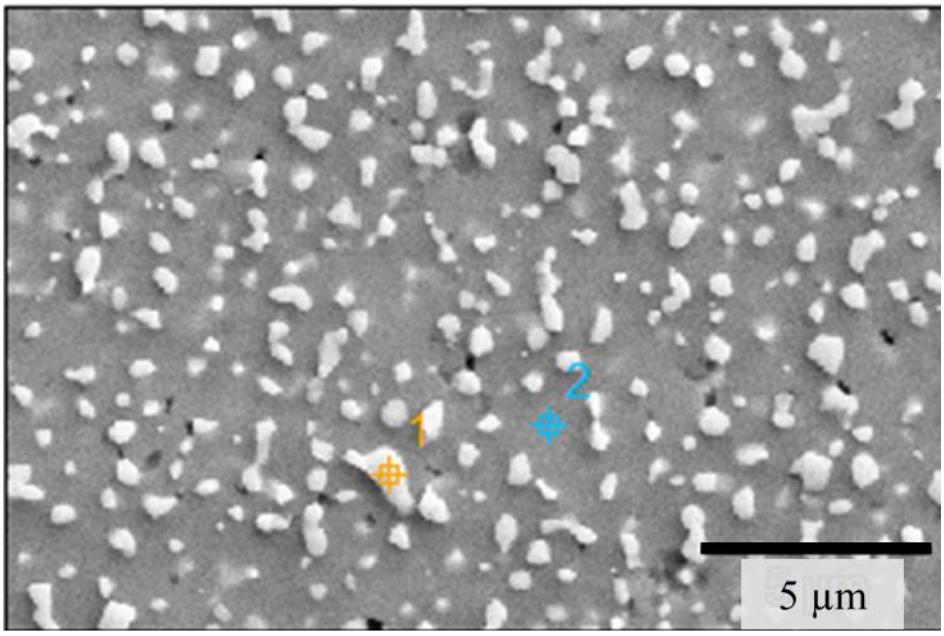

	Hf	Zr	Ti	Mo	W	Ir
Point 1	4.9	0.0	10.0	22.3	60.7	2.2
Point 2	25.4	17.9	25.1	7.6	20.2	3.9

Figure 4.4 Point EDS ($Hf_{0.2}Zr_{0.2}Ti_{0.2}Mo_{0.2}W_{0.2})B_2$ showing a tungsten-molybdenum rich secondary phase, confirmed to be a tetraboride structure of the CrB type via XRD. The iridium values are due to the conductive coating on the sample.

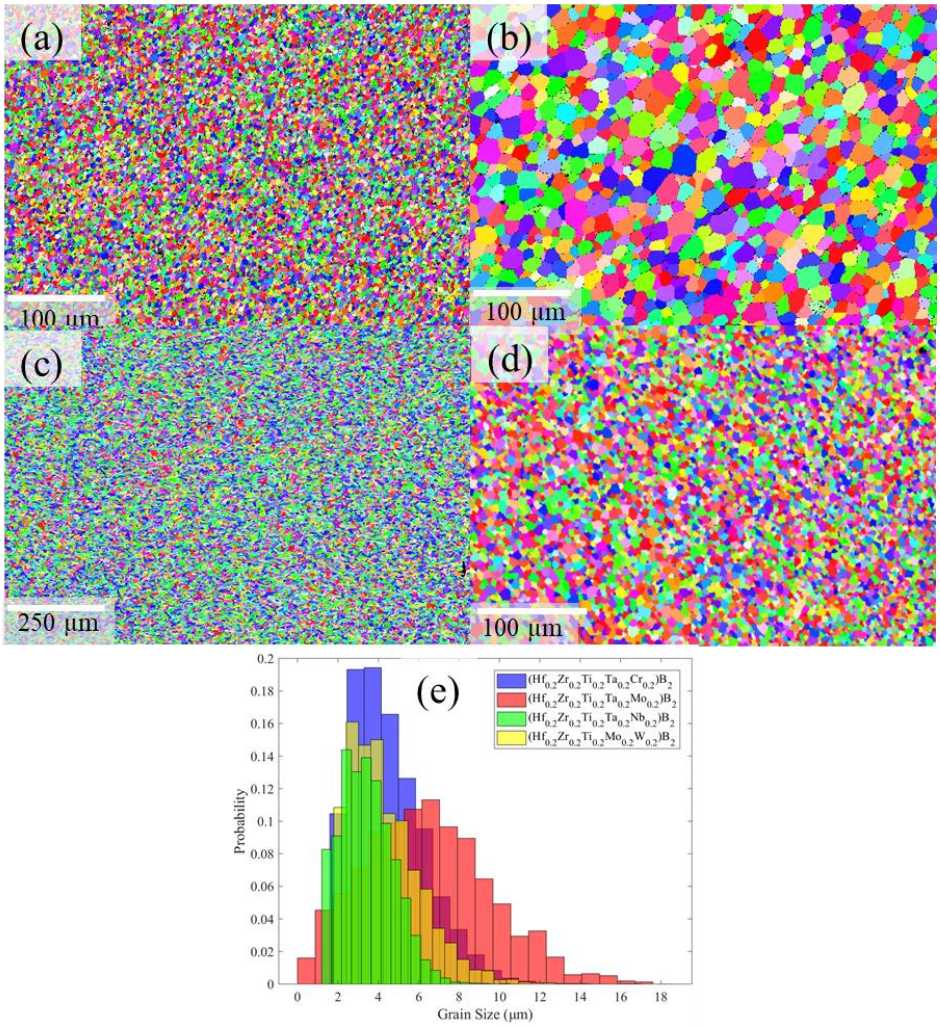

Figure 4.5 EBSD maps of (a) $(Hf_{0.2}Zr_{0.2}Ti_{0.2}Ta_{0.2}Nb_{0.2})B_2$, (b) $(Hf_{0.2}Zr_{0.2}Ti_{0.2}Ta_{0.2}Mo_{0.2})B_2$, (c) $(Hf_{0.2}Zr_{0.2}Ti_{0.2}Ta_{0.2}Cr_{0.2})B_2$, (c) $(Hf_{0.2}Zr_{0.2}Ti_{0.2}Mo_{0.2}W_{0.2})B_2$, and (e) the probability distributions of each composition with respect to grain size.

Table 4.1 All High Entropy Diborides (HEBs) fabricated, along with lattice parameters, grain size, Vicker's hardness, and excess boron carbide needed for single phase samples.

Compositions	**Lattice Parameter**		**Vicker's Hardness [GPa]**	**Grain Size [μm]**	**Excess B_4C Needed [wt%]**
	a [Å]	c [Å]			
$(Hf_{0.2}Zr_{0.2}Ti_{0.2}Ta_{0.2}Nb_{0.2})B_2$	3.097	3.372	20.5 ± 1.0	20.5 ± 1.0	3.4 ± 1.3
$(Hf_{0.2}Zr_{0.2}Ti_{0.2}Ta_{0.2}Mo_{0.2})B_2$	3.092	3.366	24.9 ± 1.0	24.9 ± 1.0	6.8 ± 4.0
$(Hf_{0.2}Zr_{0.2}Ti_{0.2}Ta_{0.2}Cr_{0.2})B_2$	3.086	3.356	24.9 ± 1.0	24.9 ± 1.0	4.5 ± 1.9
$(Hf_{0.2}Zr_{0.2}Ti_{0.2}Mo_{0.2}W_{0.2})B_2$	3.084	3.357	29.4 ± 1.7	4.3 ± 1.8	10

References

[1] D.B. Miracle, O.N. Senkov, A critical review of high entropy alloys and related concepts, Acta Mater. 122 (2017) 448–511. doi:10.1016/j.actamat.2016.08.081.

[2] J.-W. Yeh, S.-K. Chen, S.-J. Lin, J.-Y. Gan, T.-S. Chin, T.-T. Shun, C.-H. Tsau, S.-Y. Chang, Nanostructured High-Entropy Alloys with Multiple Principal Elements: Novel Alloy Design Concepts and Outcomes, Adv. Eng. Mater. 6 (2004) 299–303. doi:10.1002/adem.200300567.

[3] J.-W. Yeh, S.-J. Lin, T.-S. Chin, J.-Y. Gan, S.-K. Chen, T.-T. Shun, C.-H. Tsau, S.-Y. Chou, Formation of simple crystal structures in Cu-Co-Ni-Cr-Al-Fe-Ti-V alloys with multiprincipal metallic elements, Metall. Mater. Trans. A. 35 (2004) 2533–2536. doi:10.1007/s11661-006-0234-4.

[4] R.-Z. Zhang, F. Gucci, H. Zhu, K. Chen, M.J. Reece, Data-Driven Design of Ecofriendly Thermoelectric High-Entropy Sulfides, Inorg. Chem. 57 (2018) 13027–13033. doi:10.1021/acs.inorgchem.8b02379.

[5] J. Gild, J. Braun, K. Kaufmann, E. Marin, T. Harrington, P. Hopkins, K. Vecchio, J. Luo, A high-entropy silicide: (Mo0.2Nb0.2Ta0.2Ti0.2W0.2)Si2, J. Materiomics. (2019). doi:10.1016/j.jmat.2019.03.002.

[6] T.J. Harrington, J. Gild, P. Sarker, C. Toher, C.M. Rost, O.F. Dippo, C. McElfresh, K. Kaufmann, E. Marin, L. Borowski, P.E. Hopkins, J. Luo, S. Curtarolo, D.W. Brenner, K.S. Vecchio, Phase stability and mechanical properties of novel high entropy transition metal carbides, Acta Mater. 166 (2019) 271–280. doi:10.1016/j.actamat.2018.12.054.

[7] J. Gild, M. Samiee, J.L. Braun, T. Harrington, H. Vega, P.E. Hopkins, K. Vecchio, J. Luo, High-entropy fluorite oxides, J. Eur. Ceram. Soc. 38 (2018) 3578–3584. doi:10.1016/j.jeurceramsoc.2018.04.010.

[8] S. Jiang, T. Hu, J. Gild, N. Zhou, J. Nie, M. Qin, T. Harrington, K. Vecchio, J. Luo, A new class of high-entropy perovskite oxides, Scr. Mater. 142 (2017) 116–120. doi:10.1016/j.scriptamat.2017.08.040.

[9] J. Gild, Y. Zhang, T. Harrington, S. Jiang, T. Hu, M.C. Quinn, W.M. Mellor, N. Zhou, K. Vecchio, J. Luo, High-Entropy Metal Diborides: A New Class of High-Entropy Materials and a New Type of Ultrahigh Temperature Ceramics, Sci. Rep. 6 (2016) 37946. doi:10.1038/srep37946.

[10] D.A. Vinnik, E.A. Trofimov, V.E. Zhivulin, O.V. Zaitseva, S.A. Gudkova, A.Yu. Starikov, D.A. Zherebtsov, A.A. Kirsanova, M. Häßner, R. Niewa, High-entropy oxide phases with magnetoplumbite structure, Ceram. Int. (2019). doi:10.1016/j.ceramint.2019.03.221.

[11] Q.-W. Xing, S.-Q. Xia, X.-H. Yan, Y. Zhang, Mechanical properties and thermal stability of (NbTiAlSiZr)Nx high-entropy ceramic films at high temperatures, J. Mater. Res. 33 (2018) 3347–3354. doi:10.1557/jmr.2018.337.

[12] J. Dąbrowa, M. Stygar, A. Mikuła, A. Knapik, K. Mroczka, W. Tejchman, M. Danielewski, M. Martin, Synthesis and microstructure of the (Co,Cr,Fe,Mn,Ni)3O4 high entropy oxide characterized by spinel structure, Mater. Lett. 216 (2018) 32–36. doi:10.1016/j.matlet.2017.12.148.

[13] A. Sarkar, R. Djenadic, D. Wang, C. Hein, R. Kautenburger, O. Clemens, H. Hahn, Rare earth and transition metal based entropy stabilised perovskite type oxides, J. Eur. Ceram. Soc. (2017). doi:10.1016/j.jeurceramsoc.2017.12.058.

[14] C.M. Rost, E. Sachet, T. Borman, A. Moballegh, E.C. Dickey, D. Hou, J.L. Jones, S. Curtarolo, J.-P. Maria, Entropy-stabilized oxides, Nat. Commun. 6 (2015) 8485. doi:10.1038/ncomms9485.

[15] T. Jin, X. Sang, R.R. Unocic, R.T. Kinch, X. Liu, J. Hu, H. Liu, S. Dai, Mechanochemical-Assisted Synthesis of High-Entropy Metal Nitride via a Soft Urea Strategy, Adv. Mater. 30 (2018) 1707512. doi:10.1002/adma.201707512.

[16] X. Ren, Z. Tian, J. Zhang, J. Wang, Equiatomic quaternary (Y1/4Ho1/4Er1/4Yb1/4)2SiO5 silicate: A perspective multifunctional thermal and environmental barrier coating material, Scr. Mater. 168 (2019) 47–50. doi:10.1016/j.scriptamat.2019.04.018.

[17] J. Gild, K. Kaufmann, K. Vecchio, J. Luo, Reactive flash spark plasma sintering of high-entropy ultrahigh temperature ceramics, Scr. Mater. 170 (2019) 106–110. doi:10.1016/j.scriptamat.2019.05.039.

[18] G. Tallarita, R. Licheri, S. Garroni, R. Orrù, G. Cao, Novel processing route for the fabrication of bulk high-entropy metal diborides, Scr. Mater. 158 (2019) 100–104. doi:10.1016/j.scriptamat.2018.08.039.

[19] W.-M. Guo, D.-W. Tan, L.-Y. Zeng, Hao-Li, H.-T. Lin, C.-Y. Wang, Synthesis of fine ZrB2 powders by solid solution of TaB2 and their densification and mechanical properties, Ceram. Int. 44 (2018) 4473–4477. doi:10.1016/j.ceramint.2017.11.155.

[20] G.S. An, J.S. Han, J.U. Hur, S.-C. Choi, Synthesis of sub-micro sized high purity zirconium diboride powder through carbothermal and borothermal reduction method, Ceram. Int. 43 (2017) 5896–5900. doi:10.1016/j.ceramint.2017.01.068.

[21] W.-M. Guo, Z.-G. Yang, G.-J. Zhang, Synthesis of submicrometer HfB2 powder and its densification, Mater. Lett. 83 (2012) 52–55. doi:10.1016/j.matlet.2012.06.012.

[22] D.-W. Ni, G.-J. Zhang, Y.-M. Kan, P.-L. Wang, Synthesis of Monodispersed Fine Hafnium Diboride Powders Using Carbo/Borothermal Reduction of Hafnium Dioxide, J. Am. Ceram. Soc.

91 (2008) 2709–2712. doi:10.1111/j.1551-2916.2008.02466.x.

[23] V. Moradi, L. Nikzad, I. Mobasherpour, M. Razavi, Low temperature synthesis of Titanium diboride by carbothermal method, Ceram. Int. (2018). doi:10.1016/j.ceramint.2018.07.177.

[24] G. Junfeng, Z. Ji, S. Shi-Kuan, W. Hao, Y. Shu-Yang, W. Weimin, Z. Jinyong, F. Zhengyi, Dense and pure high-entropy metal diboride ceramics sintered from self-synthesized powders via boro/carbothermal reduction approach, Sci. CHINA Mater. (n.d.). doi:10.1007/s40843-019-9469-4.

[25] Y. Zhang, W.-M. Guo, Z.-B. Jiang, Q.-Q. Zhu, S.-K. Sun, Y. You, K. Plucknett, H.-T. Lin, Dense high-entropy boride ceramics with ultra-high hardness, Scr. Mater. 164 (2019) 135–139. doi:10.1016/j.scriptamat.2019.01.021.

[26] G.-J. Zhang, W.-M. Guo, D.-W. Ni, Y.-M. Kan, Ultrahigh temperature ceramics (UHTCs) based on ZrB 2 and HfB 2 systems: Powder synthesis, densification and mechanical properties, J. Phys. Conf. Ser. 176 (2009) 012041. doi:10.1088/1742-6596/176/1/012041.

[27] D. Ghosh, G. Subhash, Chapter 3.3 - Recent Progress in Zr(Hf)B2 Based Ultrahigh Temperature Ceramics, in: S. Somiya (Ed.), Handb. Adv. Ceram. Second Ed., Academic Press, Oxford, 2013: pp. 267–299. http://www.sciencedirect.com/science/article/pii/B9780123854698000162 (accessed October 30, 2015).

[28] Y. Zhang, Z.-B. Jiang, S.-K. Sun, W.-M. Guo, Q.-S. Chen, J.-X. Qiu, K. Plucknett, H.-T. Lin, Microstructure and mechanical properties of high-entropy borides derived from boro/carbothermal reduction, J. Eur. Ceram. Soc. (2019). doi:10.1016/j.jeurceramsoc.2019.05.017.

[29] Y. Pan, X. Wang, S. Li, Y. Li, M. Wen, DFT prediction of a novel molybdenum tetraboride superhard material, RSC Adv. 8 (2018) 18008–18015. doi:10.1039/C8RA02324G.

[30] R. Mohammadi, C.L. Turner, M. Xie, M.T. Yeung, A.T. Lech, S.H. Tolbert, R.B. Kaner, Enhancing the Hardness of Superhard Transition-Metal Borides: Molybdenum-Doped Tungsten Tetraboride, Chem. Mater. 28 (2016) 632–637. doi:10.1021/acs.chemmater.5b04410.

[31] W.G. Fahrenholtz, G.E. Hilmas, I.G. Talmy, J.A. Zaykoski, Refractory Diborides of Zirconium and Hafnium, J. Am. Ceram. Soc. 90 (2007) 1347–1364. doi:10.1111/j.1551-2916.2007.01583.x.

[32] E.W. Neuman, G.E. Hilmas, W.G. Fahrenholtz, Processing, microstructure, and mechanical properties of zirconium diboride-boron carbide ceramics, Ceram. Int. 43 (2017) 6942–6948. doi:10.1016/j.ceramint.2017.02.117.

[33] T.S.R.Ch. Murthy, J.K. Sonber, C. Subramanian, R.K. Fotedar, M.R. Gonal, A.K. Suri, Effect of CrB2 addition on densification, properties and oxidation resistance of TiB2, Int. J.

Refract. Met. Hard Mater. 27 (2009) 976–984. doi:10.1016/j.ijrmhm.2009.06.004.

[34] B. Mahesh, K. Sairam, J.K. Sonber, T.S.R.Ch. Murthy, G.V.S. Nageswara Rao, T. Srinivasa Rao, J.K. Chakravartty, Sinterability studies of monolithic chromium diboride (CrB2) by spark plasma sintering, Int. J. Refract. Met. Hard Mater. 52 (2015) 66–69. doi:10.1016/j.ijrmhm.2015.04.035.

[35] J.B. Levine, S.H. Tolbert, R.B. Kaner, Advancements in the Search for Superhard Ultra-Incompressible Metal Borides, Adv. Funct. Mater. 19 (2009) 3519–3533. doi:10.1002/adfm.200901257.

[36] Q. Gu, G. Krauss, W. Steurer, Transition Metal Borides: Superhard versus Ultra-incompressible, Adv. Mater. 20 (2008) 3620–3626. doi:10.1002/adma.200703025.

Chapter 5. High-Entropy Fluorite Oxides

5.1 Introduction

High-entropy alloys (HEAs), also known as complex concentrated alloys (CCAs) or multi-principal element alloys, typically consist of five or more principal elements in amounts ranging from 5 to 35 at. % [1,2]. The configurational entropy can reach a significant amount once five or more principal components are present in the system; it reaches a maximum value of $\Delta S_{mix} = R\ln N$ per mole for a N-component system, where R is the gas constant, for an equimolar composition. HEAs/CCAs, with intrinsically high lattice strain, are generally observed to possess lower thermal conductivity and higher hardness than their individual constituents [1,3]. HEAs/CCAs also exhibit a variety of other superior or promising properties [1,3].

Since the initial publications of HEAs/CCAs in 2004 by Yeh *et al.* [[4] and Cantor *et al.* [5], studies of high-entropy metallic alloys have attracted great attention in the metallurgy community. In 2015, an entropy-stabilized oxide of the rocksalt crystal structure, $(Mg_{0.2}Zn_{0.2}Cu_{0.2}Co_{0.2}Ni_{0.2})O$, was fabricated by Rost *et al.* [6], extending HEAs from metals to ceramics with ionic bonds. Further studies of this entropy-stabilized rocksalt oxide showed that doping aliovalent cations can lead to excellent lithium conductivity and enhanced dielectric constants [7,8]. It should be noted that prior studies have also fabricated high-entropy nitride and carbide films via reactive sputtering techniques [9,10]. More recently, high-entropy ultra-high temperature ceramics (HE-UHTCs), *e.g.*, $(Hf_{0.2}Zr_{0.2}Ta_{0.2}Nb_{0.2}Ti_{0.2})B_2$ and five other single-phase five-component metal diborides, and high-entropy functional ceramics, *e.g.*, $Sr(Zr_{0.2}Sn_{0.2}Ti_{0.2}Hf_{0.2}Mn_{0.2})O_3$ and five other single-phase high-entropy perovskite oxides (HEPOs), have also been successfully synthesized [11,12]. Recent research efforts have been

reported towards making multicomponent rare earth oxides [13], (Ti, Ta, Nb)C_xN_{1-x} cermets [14], and high-entropy thermoelectric materials [15].

Fluorite oxides are utilized for a variety of applications including solid ionic conductors, high temperature coatings, and catalysts [16–20]. The most widely-used fluorite oxides are based on zirconia (ZrO_2), hafnia (HfO_2), or ceria (CeO_2), and they are often doped with yttria (Y_2O_3) and/or various other oxide dopants (including rare earth oxides as well as MgO, CaO, and other oxides). This class of oxide materials often possess high oxygen conductivities, low thermal conductivities, high hardness, and high melting temperatures. In particular, rare earth doped zirconia and ceria are of great technological interest because of their high ionic or mixed conductivities as well as low thermal conductivities [16,17,19–21].

Specifically, high-entropy materials are of interest for their low thermal conductivity due to the possible scattering of phonons by multiple components and strained lattices. In this work, we examine the synthesis, phase stability (including the formation of high-entropy solid solutions), and selected properties of high-entropy fluorite oxides (HEFOs) consisting of solid solutions with equal molar fractions of HfO_2, ZrO_2, and CeO_2 as the base materials, as well as the additions of the oxides of Y, Yb, Ca, Ti, La, Mg, and Gd as fluorite phase stabilizers. We successfully synthesized eight single-phase, high-entropy, fluorite oxide solid solutions, namely, $(Hf_{0.25}Zr_{0.25}Ce_{0.25}Y_{0.25})O_{2-\delta}$, $(Hf_{0.25}Zr_{0.25}Ce_{0.25})(Y_{0.125}Yb_{0.125})O_{2-\delta}$, $(Hf_{0.2}Zr_{0.2}Ce_{0.2})(Y_{0.2}Yb_{0.2})O_{2-\delta}$, $(Hf_{0.25}Zr_{0.25}Ce_{0.25})(Y_{0.125}Ca_{0.125})O_{2-\delta}$, $(Hf_{0.25}Zr_{0.25}Ce_{0.25})(Y_{0.125}Gd_{0.125})O_{2-\delta}$, $(Hf_{0.2}Zr_{0.2}Ce_{0.2})(Y_{0.2}Gd_{0.2})O_{2-\delta}$, $(Hf_{0.25}Zr_{0.25}Ce_{0.25})(Yb_{0.125}Gd_{0.125})O_{2-\delta}$, and $(Hf_{0.2}Zr_{0.2}Ce_{0.2})(Yb_{0.2}Gd_{0.2})O_{2-\delta}$. The thermal and electrical conductivities, as well as hardness, of these materials are measured and compared with 8 mol. Y_2O_3-stabilized ZrO_2 (8YSZ) as a reference fluorite oxide. Notably, these single-phase HEFOs possess lower thermal

conductivities than that of 8YSZ, due to high phonon scattering by the multiple cations and strained lattices.

5.2 Synthesis and Fabrication

To synthesize high-entropy fluorite oxides, powders of HfO_2, ZrO_2, CeO_2, TiO_2, Y_2O_3, Yb_2O_3, La_2O_3, Gd_2O_3, CaO, and MgO (≥99% purity; purchased from Alfa Aesar, MA, USA) were used as the starting materials. Appropriate amounts of five powders were weighted (calculated on a metals basis) and mixed to fabricate each composition of the targeted stoichiometry, listed Table 1.

We have examined 12 compositions. Each composition consists of an equal molar fraction of HfO_2, ZrO_2, and CeO_2 (either 25% or 20% on a metal basis) as the base material and includes one stabilizer (for Specimen HEFO1 with 25% Y_2O_3 as the only four-cation system) or two stabilizers of equal cationic fraction of 12.5% or 20%. In general, the five-cation compositions examined have the stoichiometry $(Hf_{0.25}Zr_{0.25}Ce_{0.25})(\alpha_{0.125}\beta_{0.125})O_{2-\delta}$ (Variant A) or $(Hf_{0.2}Zr_{0.2}Ce_{0.2})(\alpha_{0.2}\beta_{0.2})O_{2-\delta}$ (Variant B), where α and β represent two stabilizers. In general, we would not examine Variant B if Variant A did not form a single-phase HEFO. In addition to the four-cation composition HEFO1: $(Hf_{0.25}Zr_{0.25}Ce_{0.25}Y_{0.25})O_{2-\delta}$, 11 five-cation compositions (HEFO2A, HEFO3A, HEFO4A, HEFO4B, HEFO5A, HEFO5B, HEFO6A, HEFO7A, HEFO7B, HEFO8A, and HEFO8B) were examined in this study, where "A" or "B" refers to the Variant defined above. In addition, we also fabricated 8YSZ, Y_2O_3, and Yb_2O_3 as the reference materials. All compositions fabricated are listed in Table 1.

The raw powders were mixed via high-energy ball milling (HEBM) utilizing a SPEX 8000D mill (SpexCertPrep, NJ, USA) for 24 hours in a silicon nitride jar with silicon nitride media. High-purity isopropyl alcohol was used to create a slurry for grinding to prevent caking of the powders in the milling containers. The HEBM was done in 30-minute intervals, interrupted by 10-minute cooling pauses to avoid overheating. The powders were then densified into 20-mm diameter disks via spark plasma sintering (SPS, Thermal Technologies, CA, USA) at 1800˚C for 5 minutes under a uniaxial pressure of 50 MPa with a heating ramping rate of 100˚C/min. The chamber was initially pumped down to vacuum of at least 10^{-2} Torr prior to the SPS experiments and flowed/flushed with argon gas at 700˚C to allow for off-gassing. The graphite die was lined with 125 μm thick graphite paper to prevent reaction of the specimen with the die. After SPS, the specimens were annealed in open air at 1500˚C for 12 hours for decarburization. Most samples were subsequently annealed for 24 hours at 1500˚C for homogenization and air-quenched or furnace cooled to room temperature for characterization and measurements. The samples fabricated for measuring thermal and electrical conductivity as well as hardness testing were furnace cooled (with the power shut down; instead of quenching to prevent microcracking), where the initial cooling rate was approximately 50˚C/min at 1500˚C.

5.3 Characterization

All specimens were characterized by X-ray diffraction (XRD) utilizing a Rigaku diffractometer with Cu Kα radiation.

Scanning electron microscopy (SEM) images and the corresponding energy dispersive X-ray (EDX) spectroscopy composition maps were collected from specimens of all compositions. The specimens were coated with carbon prior to analysis to prevent charging. The measurements were performed at an e-beam voltage of 20 kV to examine the higher energy peaks of Hf, Ce,

and Gd for minimal convolution of the peaks. Due to the overlap between the Hf M_α and Si K_α peaks, the amount of Si contamination in the sample is unknown.

Densities were calculated from the measured mass and geometric parameters of the pellets. The relative densities were calculated utilizing theoretical densities computed utilizing an ideal stoichiometry and the lattice parameter measured by XRD.

5.3.1 Thermal Conductivity

Thermal conductivities were measured using time-domain thermoreflectance [22,23]. A ~90 nm Al film (measured using picosecond acoustics) is thermally evaporated onto each sample to act as a transducer to convert the optical energy to thermal energy [24]. Using a Ti:Sapphire laser emitting a train of subpicosecond pulses at a central wavelength of 800 nm and a repetition rate of 80 MHz, the output is divided into a pump and probe path. The pump, which is modulated at a frequency of 9.8 MHz, was used to heat the sample, while the probe was utilized to monitor the change in reflectivity at the sample surface. A lock-in amplifier was used to isolate these reflectivity changes at the pump modulation frequency. The pump and probe beams were focused with a 5X objective lens to 35 μm and 15 μm $1/e^2$ diameters, respectively. Utilizing a multilayer, radially symmetric heat diffusion model, we extracted the thermal conductivity and Al/HEFO thermal boundary conductance by adjusting these parameters to obtain the best fit to the ratio of in-phase to out-of-phase voltage obtained by the lock-in amplifier [22,25]. The heat capacity of the Al film from a prior report [26] was used. The Al thermal conductivity was obtained from 4-point probe resistivity measurements and applying the Wiedemann–Franz law. Fundamentally, we measured the thermal diffusivity of the HEFO to obtain the thermal conductivity. We utilized a rule of mixtures based on the constituent oxides to obtain an estimate of heat capacity for each sample, typically ~3 J cm^{-3} K^{-1}. Uncertainties for the extracted thermal

conductivities included those from the repeatability over several spots on the sample, the uncertainty in Al thickness, and the uncertainty in HEFO heat capacity.

5.3.2 Electrical Conductivity

Electrical conductivities were measured for compositions HEFO1, HEFO4A, HEFO4B, HEFO5A, and HEFO7B, as well as the 8YSZ reference, with electrochemical impedance spectroscopy (EIS) using an impedance analyzer (Solartron 1255B) in the frequency range of 1MHz to 1Hz between 650 and 850˚C at 25˚C intervals with Pt electrodes on both sides of the pellets in zero grade dry air. Platinum pastes were applied to both faces of the samples and subsequently cured at 1000˚C for 10 minutes prior to conductivity measurements. Total conductivity was determined by fitting Nyquist plots using the Z-View software (Scribner, Inc.). Activation energies for the total conductivities were determined from the Arrhenius plots.

5.3.3 Hardness

Vicker's hardness measurements were performed on all single-phase high-entropy oxides as well as 8YSZ, pure Y_2O_3, and pure Yb_2O_3 samples (made by the identical HEBM and SPS fabrication procedure) as benchmarks. Hardness measurements were performed with a Vickers' diamond indenter at 200 kgf/mm^2 with a hold time of 15 seconds. The indentations were examined for conformation with the standard ASTM C1327. The indentations averaged 20–25 μm in width during the testing. Twenty-five measurements were performed at different locations of each specimen; the mean and standard deviation are reported.

5.4 Results and Discussion

5.4.1 Phase Formation and Compositional Uniformity

After SPS and subsequent 1000˚C annealing in air, a cubic (fluorite-structured), single-phase, solid solution was observed to form in eight different compositions: HEFO1: $(Hf_{0.25}Zr_{0.25}Ce_{0.25}Y_{0.25})O_{2-\delta}$, HEFO4A: $(Hf_{0.25}Zr_{0.25}Ce_{0.25})(Y_{0.125}Yb_{0.125})O_{2-\delta}$, HEFO4B: $(Hf_{0.2}Zr_{0.2}Ce_{0.2})(Y_{0.2}Yb_{0.2})O_{2-\delta}$, HEFO5A: $(Hf_{0.25}Zr_{0.25}Ce_{0.25})(Y_{0.125}Ca_{0.125})O_{2-\delta}$, HEFO7A: $(Hf_{0.25}Zr_{0.25}Ce_{0.25})(Y_{0.125}Gd_{0.125})O_{2-\delta}$, HEFO7B: $(Hf_{0.2}Zr_{0.2}Ce_{0.2})(Y_{0.2}Gd_{0.2})O_{2-\delta}$, HEFO8A: $(Hf_{0.25}Zr_{0.25}Ce_{0.25})(Yb_{0.125}Gd_{0.125})O_{2-\delta}$, and HEFO8B: $(Hf_{0.2}Zr_{0.2}Ce_{0.2})(Yb_{0.2}Gd_{0.2})O_{2-\delta}$ according to the XRD analysis (Fig. 1).

Four other compositions have secondary phases, which were identified using XRD to be $Y_2Ti_2O_7$ in HEFO2A: $(Hf_{0.25}Zr_{0.25}Ce_{0.25})(Y_{0.125}Ti_{0.125})O_{2-\delta}$, MgO in HEFO3A: $(Hf_{0.25}Zr_{0.25}Ce_{0.25})(Y_{0.125}Mg_{0.125})O_{2-\delta}$, $CaHfO_3$ in HEFO5B: $(Hf_{0.2}Zr_{0.2}Ce_{0.2})(Y_{0.2}Ca_{0.2})O_{2-\delta}$, and $La_2(Hf/Zr)_2O_7$ in HEFO6A: $(Hf_{0.25}Zr_{0.25}Ce_{0.25})(Y_{0.125}La_{0.125})O_{2-\delta}$, respectively (Fig. 2). Yet, the major phase is still a cubic fluorite solid-solution phase in each of these four cases.

Furthermore, EDX elemental maps (as seen in figures 8-19) verified compositional uniformity in the eight specimens of HEFO1, HEFO4A, HEFO4B, HEFO5A, HEFO7A, HEFO7B, HEFO8A, and HEFO8B that XRD suggested the formation of single-phase solid solutions, as well as the presence of the secondary phases in four other compositions (HEFO2A, HEFO3A, HEFO5B, and HEFO6A). Fig. 3 shows three selected (representative) elemental maps of HEFO4B: $(Hf_{0.2}Zr_{0.2}Ce_{0.2})(Y_{0.2}Yb_{0.2})O_{2-\delta}$ and HEFO7B: $(Hf_{0.2}Zr_{0.2}Ce_{0.2})(Y_{0.2}Gd_{0.2})O_{2-\delta}$, where single solid-solution phases formed, and HEFO5B: $(Hf_{0.2}Zr_{0.2}Ce_{0.2})(Y_{0.2}Ca_{0.2})O_{2-\delta}$, where a $CaHfO_3$ secondary phase formed.

The eight single-phase solutions all have high configurational entropies contributed from the cation sublattices, *i.e.*, 1.39*R*/mole (*i.e.*, 1.39*R* per mole of $(Hf_{0.25}Zr_{0.25}Ce_{0.25}Y_{0.25})O_{2-\delta}$) for

HEFO1, 1.56*R*/mole for HEFO4A, HEFO5A, HEFO7A, and HEFO8A, and 1.61*R*/mole for HEFO4B, HEFO7B, and HEFO8B. In this regard, this term “high entropy” is adopted here because of its historical significance and only implies that these HEFOs have relatively higher configurational entropies per mole of metal cations, in comparison with conventional fluorite oxides such as YSZ.

It is also important to note that here we only count the configurational entropy contribution from the cation (metal ions) sublattice and normalize it to per mole of the oxide chemical formula (that contains one mole of metal cations). There is an additional configurational entropy contribution from the anion sublattice due to the oxygen vacancies, which is much smaller.

5.4.2 Sintered Densities

The relative densities of sintered specimens for all single-phase materials were calculated based on the measured densities and theoretical densities computed from XRD lattice parameters and listed in Table 1. The sintered samples achieved over ~95% of their respective theoretical densities after the SPS and 1500˚C annealing.

5.4.3 Thermal Conductivity

The thermal conductivities of YSZ have been extensively studied due to its use as a thermal barrier coating at high temperatures. The conductivity is observed to be dependent upon the porosity, fabrication method, and doping level. The thermal conductivity of our 8YSZ specimen, fabricated using the same methods as our HEFOs, was measured to be 2.02 ± 0.17 W/m-K, which is in good agreement with literature for fully-dense, polycrystalline 8YSZ [27].

The measured thermal conductivities of eight single-phase HEFOs are all lower than that of 8YSZ (Fig. 4). Specifically, HEFO5A: $(Hf_{0.25}Zr_{0.25}Ce_{0.25})(Y_{0.125}Ca_{01.25})\,O_{2-\delta}$ (with 98.5% relative density) possesses the lowest thermal conductivity of 1.1 ± 0.2 W/m-K, followed by HEFO4B and HEFO7A. The reduced thermal conductivities in HEFOs are likely related to increased phonon scattering in the system due to multiple metal cations as well as high amounts of lattice strains [28].

Both grain sizes and porosity can affect thermal conductivity, in addition to the intrinsic effects. On one hand, significant phonon scattering at the grain boundaries is not expected to be a major factor due to the large grain size of 1-3 μm of the HEFOs. Overall, we can conclude that high-entropy effects do appear to reduce thermal conductivities in general.

5.4.4 Ionic Conductivity

The measured electrical conductivities of HEFOs and the 8YSZ reference in zero-grade dry air between 650˚C and 850˚C are shown in Fig. 5. HEFOs generally have significantly lower conductivities than 8YSZ. Arrhenius plots [$\ln(\sigma T)$ *vs.* $1000/T$] of the electrical conductivities were used to find the activation energies. Since the platinum electrode is not blocking (for electrons and holes), the measured conductivities include both electronic and (oxygen) ionic contributions. All the HEFOs examined possess similar activation energies of 1.14-1.29 eV and nearly identical conductivity values.

The conductivities of the 8YSZ specimen are approximately an order of magnitude higher than the HEPOs. This is not surprising, as an optimal amount of doping into zirconia and ceria based ceramics exists (*e.g.*, ~ 8 mol. % Y_2O_3 in YSZ) [29,30] and our HEFOs have much higher doping levels (*e.g.*, equivalent to ~14 mol. % in HEFO1 or HEFO4A, and ~25 mol. % in

HEFO4B). In addition, partial substitution of CaO (a dopant used in HEFO5A) into the YSZ lattice is observed to depress the overall conductivity at lower temperatures [31].

Another factor that can affect ionic conductivity of fluorite oxides is the grain size [32]. Our HEFOs generally have smaller grain sizes than the 8YSZ reference, which can also contribute to lower overall conductivities. Electron backscattering diffraction (EBSD) was used to determine the grain size distributions in both the 8YSZ reference sample and HEFO4B: $(Hf_{0.2}Zr_{0.2}Ce_{0.2})(Yb_{0.2}Gd_{0.2})O_{2-\delta}$ as examples. The average grain size of HEFO4B is 4.71 ± 0.73 μm, while that of the 8YSZ is 12.78 ± 4.02 μm, as is shown in Fig. 6. The smaller grain sizes in HEFOs may be due to "sluggish kinetics" of grain growth of high-entropy materials, and they can reduce the overall electrical conductivities due to the well-known high grain boundary resistance in fluorite oxides.

5.4.5 Hardness

The measured Vicker's hardness values of eight single-phase HEFO specimens are in the range of 12.3 to 13.6 GPa, which are comparable with that of an 8YSZ specimen fabricated via the identical procedure (13 ± 0.5 GPa), as shown in Fig. 7 and Table 1. The reported hardness of doped zirconia and ceria based ceramics varies from 6 to 13.5 GPa, with ceria based ceramics leaning towards lower values [19,33–35]. Pure Y_2O_3 and Yb_2O_3 were also fabricated utilizing the identical procedure for testing to benchmark, which possess significantly lower hardness values of 6.9 ± 0.3 GPa and 5.7 ± 0.3 GPa, respectively. XRD characterization verified that the pure Y_2O_3 and Yb_2O_3, as well as 8YSZ, all showed single cubic phases. HEFO8A: $(Hf_{0.25}Zr_{0.25}Ce_{0.25})(Yb_{0.125}Gd_{0.125})O_{2-\delta}$ and HEFO8B: $(Hf_{0.2}Zr_{0.2}Ce_{0.2})(Yb_{0.2}Gd_{0.2})O_{2-\delta}$ are slightly softer in comparison with other HEFOs. In summary, the eight HEFOs all possess hardness

values (with a mean of 13.25 GPa and a standard deviation of 0.5 GPa) comparable to that of 8YSZ (13 GPa for our specimen fabricated using the same procedure, similar to that reported in Refs [36,37]), despite higher contents of the softer components of Y_2O_3 and Yb_2O_3.

5.5 Conclusion

Eight single-phase HEFOs or high-entropy fluorite oxides were fabricated via high-energy ball milling, spark plasma sintering, and annealing. The high-entropy fluorite oxides exhibit hardness values comparable to that of the 8YSZ reference (despite high contents of softer components such as Y_2O_3 and Yb_2O_3) and possess lower electrical conductivities. Notably, these HEFOs shows promising potential as low thermal conductivity materials, which are likely a result of the high phonon scattering due to the multiple cations and strained lattices.

Chapter 5, in part, is a reprint of the material “High-Entropy Fluorite Oxides” as it appears in *Journal of the European Ceramic Society*, J. Gild, M. Samiee, J.L. Braun, T. Harrington, H. Vega, P.E. Hopkins, K. Vecchio, J. Luo, Journal of the European Ceramic Society. 38 (2018) 3578–3584. The dissertation author was the primary investigator and wrote the first draft of manuscript.

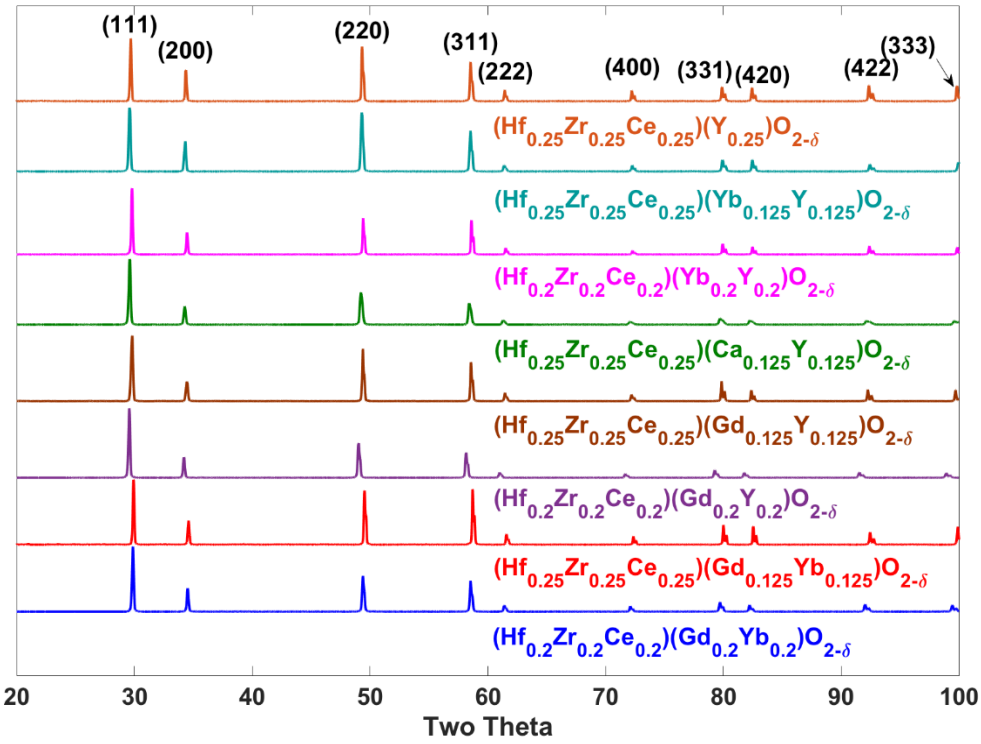

Figure 5.1 XRD patterns of HEFO1: $(Hf_{0.25}Zr_{0.25}Ce_{0.25}Y_{0.25})O_{2-\delta}$, HEFO4A: $(Hf_{0.25}Zr_{0.25}Ce_{0.25})(Y_{0.125}Yb_{0.125})O_{2-\delta}$, HEFO4B: $(Hf_{0.2}Zr_{0.2}Ce_{0.2})(Y_{0.2}Yb_{0.2})O_{2-\delta}$, HEFO5A: $(Hf_{0.25}Zr_{0.25}Ce_{0.25})(Y_{0.125}Ca_{0.125})O_{2-\delta}$, HEFO7A: $(Hf_{0.25}Zr_{0.25}Ce_{0.25})(Y_{0.125}Gd_{0.125})O_{2-\delta}$, HEFO7B: $(Hf_{0.2}Zr_{0.2}Ce_{0.2})(Y_{0.2}Gd_{0.2})O_{2-\delta}$, HEFO8A: $(Hf_{0.25}Zr_{0.25}Ce_{0.25})(Yb_{0.125}Gd_{0.125})O_{2-\delta}$ and HEFO8B: $(Hf_{0.2}Zr_{0.2}Ce_{0.2})(Yb_{0.2}Gd_{0.2})O_{2-\delta}$, all of which exhibit single solid-solution phases of the fluorite structure.

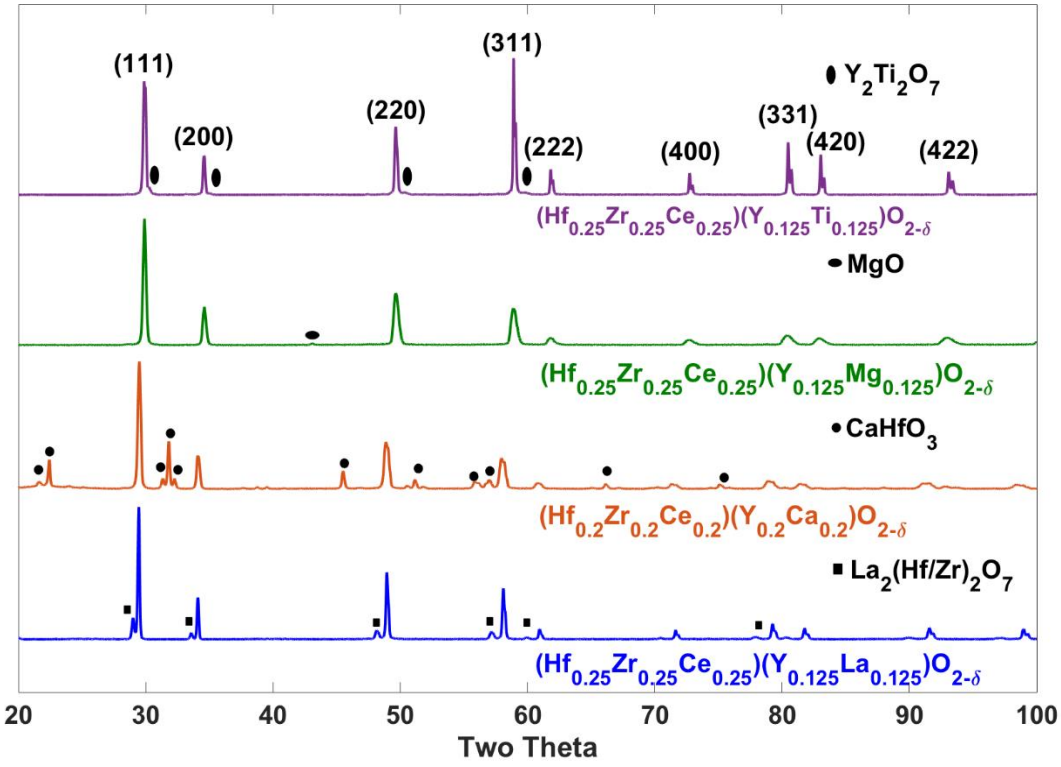

Figure 5.2 XRD patterns of HEFO2A: $(Hf_{0.25}Zr_{0.25}Ce_{0.25})(Y_{0.125}Ti_{0.125})O_{2-\delta}$, HEFO3A: $(Hf_{0.25}Zr_{0.25}Ce_{0.25})(Y_{0.125}Mg_{0.125})O_{2-\delta}$, HEFO5B: $(Hf_{0.2}Zr_{0.2}Ce_{0.2})(Y_{0.2}Ca_{0.2})O_{2-\delta}$, HEFO6A: $(Hf_{0.25}Zr_{0.25}Ce_{0.25})(Y_{0.125}La_{0.125})O_{2-\delta}$, all of which possess secondary phases. In all four cases, the primary phases are still solid-solution phases of the fluorite structure.

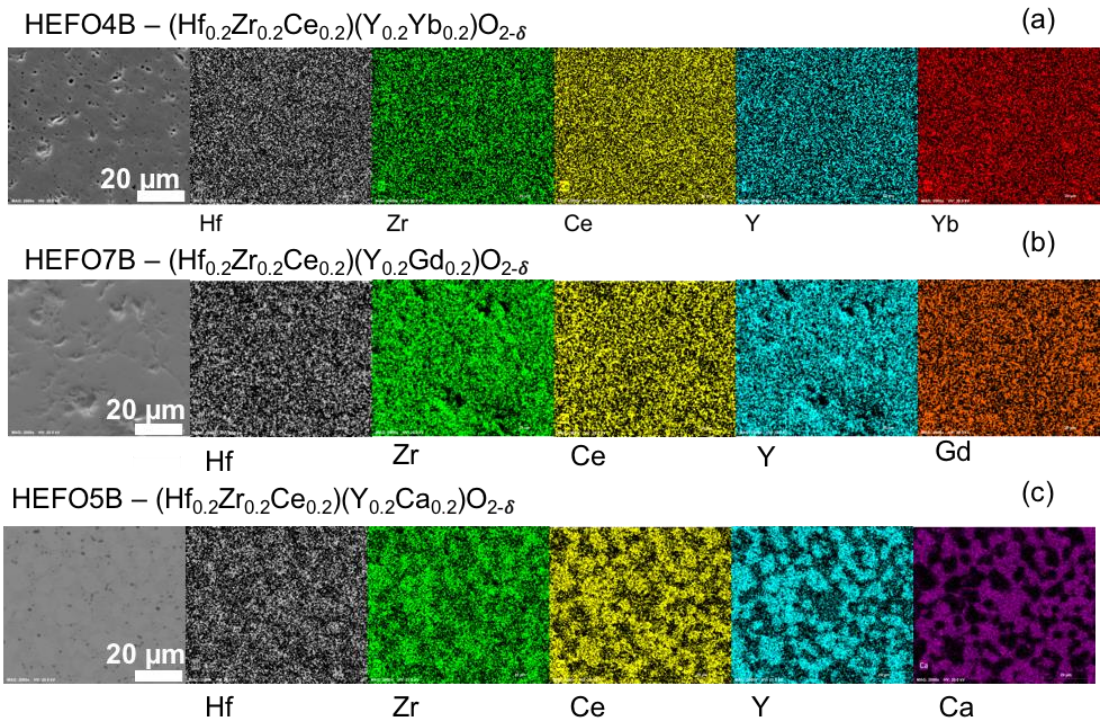

Figure 5.3 Cross-sectional SEM images and the corresponding EDS compositional maps of three selected specimens: **(a, b)** HEFO4B: $(Hf_{0.2}Zr_{0.2}Ce_{0.2})(Y_{0.2}Yb_{0.2})O_{2-\delta}$ and HEFO7B: $(Hf_{0.2}Zr_{0.2}Ce_{0.2})(Y_{0.2}Gd_{0.2})O_{2-\delta}$ that exhibit single solid-solution phases with homogeneous compositions and **(c)** HEFO5B: $(Hf_{0.2}Zr_{0.2}Ce_{0.2})(Y_{0.2}Ca_{0.2})O_{2-\delta}$ with a $CaHfO_3$ secondary phase. SEM images and the corresponding EDS compositional maps, along with XRD patterns, of all 12 specimens are documented in the Data Statement.

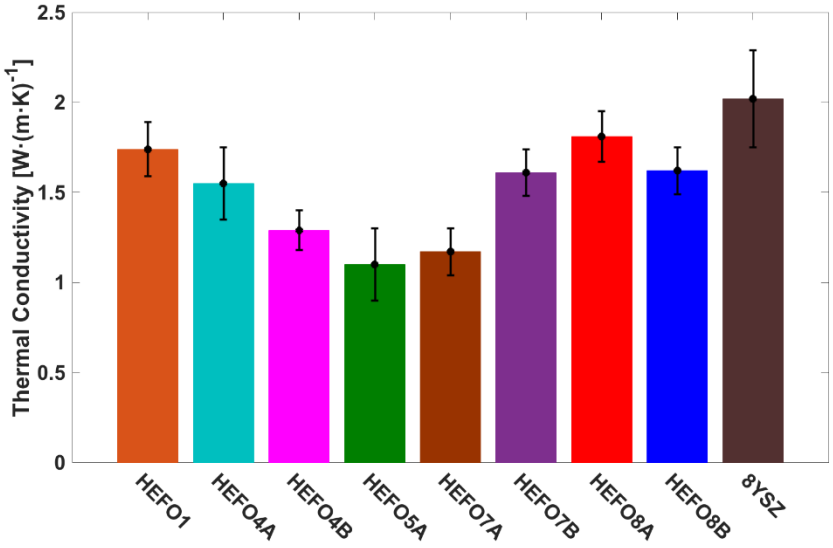

Figure 5.4 Thermal conductivities of the eight single-phase HEFOs, along with 8YSZ, measured by TDTR. All HEFOs possess lower thermal conductivities than the fully-dense 8YSZ; three of them, *i.e.*, HEFO4B: $(Hf_{0.2}Zr_{0.2}Ce_{0.2})(Y_{0.2}Yb_{0.2})O_{2-\delta}$, HEFO5A:$(Hf_{0.25}Zr_{0.25}Ce_{0.25})(Y_{0.125}Ca_{0.125})O_{2-\delta}$, and HEFO7A: $(Hf_{0.25}Zr_{0.25}Ce_{0.25})(Y_{0.125}Gd_{0.125})O_{2-\delta}$, show significantly lower thermal conductivities. All specimens were fabricated by the identical process of SPS and subsequent 1500˚C annealing in air.

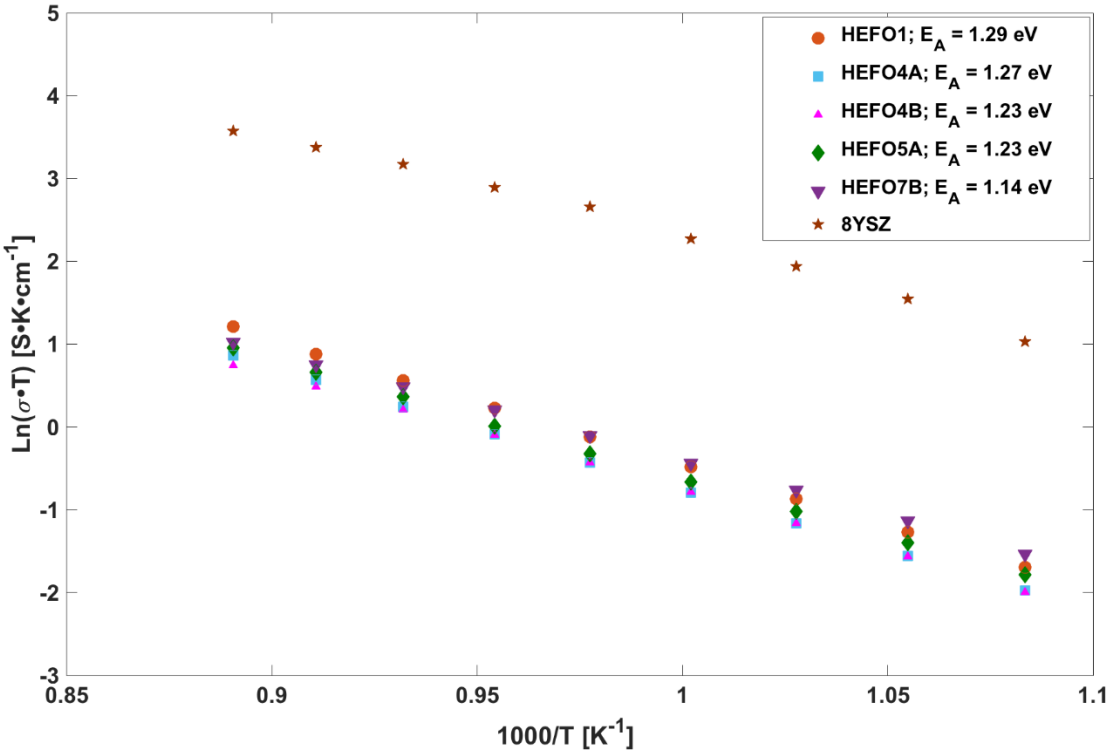

Figure 5.5 Arrhenius plots of measured conductivities for five single-phase HEFO, along with 8YSZ, from 650˚C to 850˚C (measured in zero grade dry air).

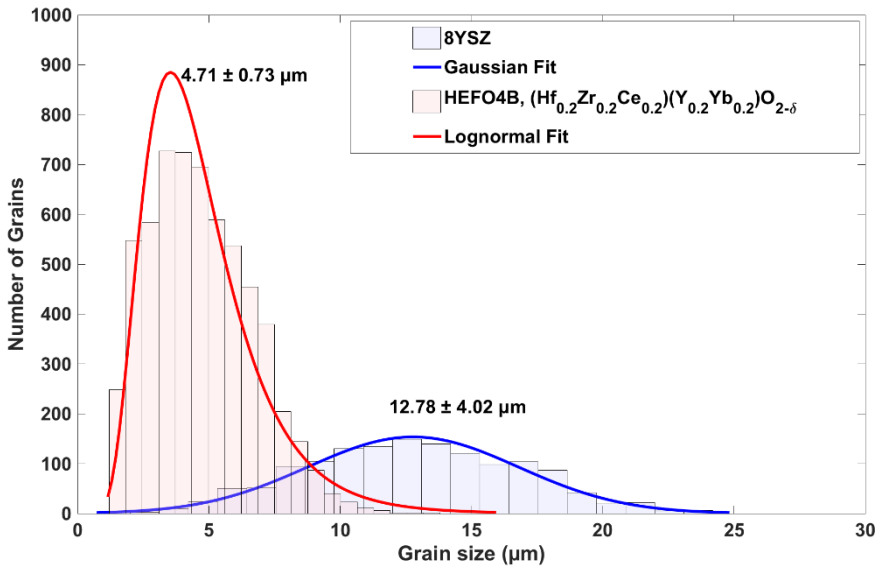

Figure 5.6. Grain size distributions of HEFO4B: $(Hf_{0.2}Zr_{0.2}Ce_{0.2})(Y_{0.2}Yb_{0.2})O_{2-\delta}$ and 8YSZ. Both specimens were fabricated by the identical process of SPS and subsequent 1500˚C annealing in air.

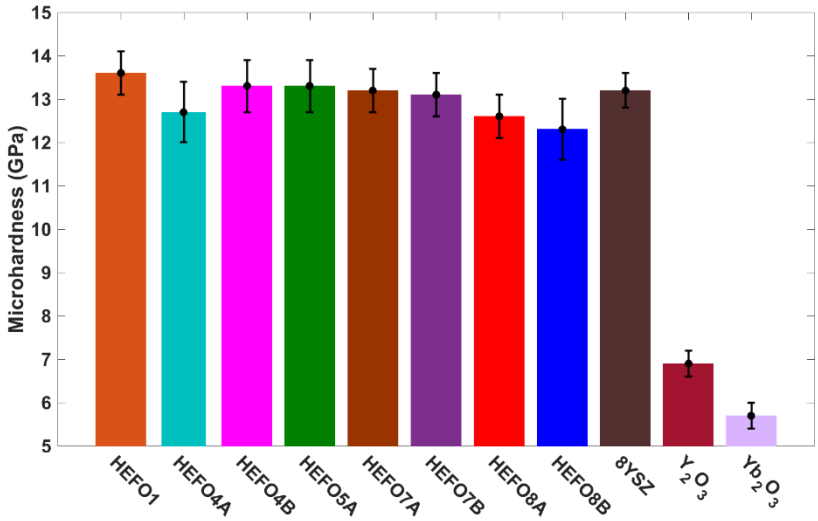

Figure 5.7 Measured hardness of eight single-phase HEFO along with 8YSZ, Y_2O_3 and Yb_2O_3 for comparison.

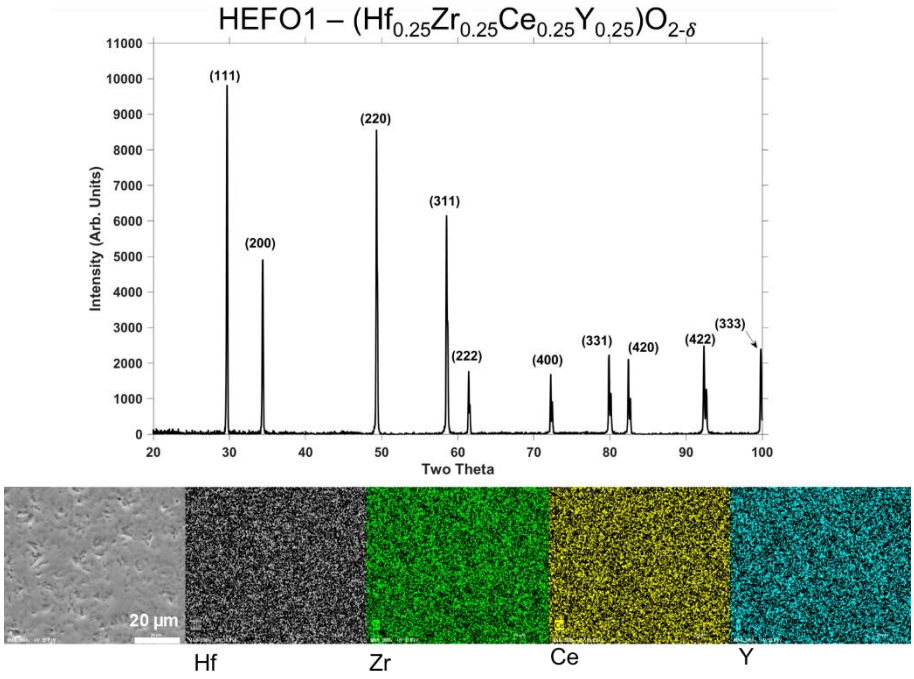

Figure 5.8 HEFO1: $(Hf_{0.25}Zr_{0.25}Ce_{0.25})(Y_{0.25})O_{2-\delta}$: **(a)** XRD patterns showing phase evolution during the HEBM-SPS fabrication process. **(b)** Cross-sectional SEM image and the corresponding EDX compositional maps of the specimen after SPS

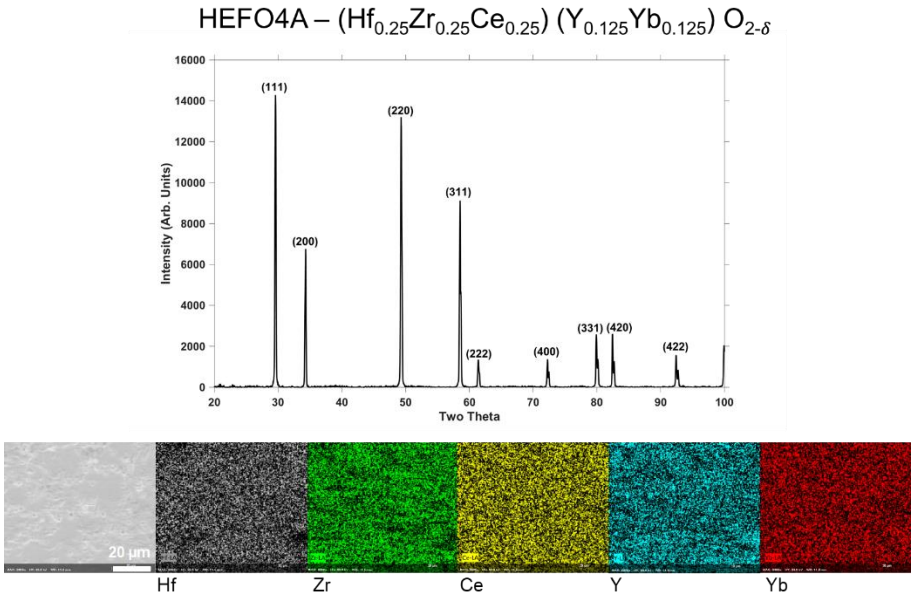

Figure 5.9 HEFO4A: $(Hf_{0.25}Zr_{0.25}Ce_{0.25})(Y_{0.125}Y_{0.125})O_{2-\delta}$: **(a)** XRD patterns showing phase evolution during the HEBM-SPS fabrication process. **(b)** Cross-sectional SEM image and the corresponding EDX compositional maps of the specimen after SPS

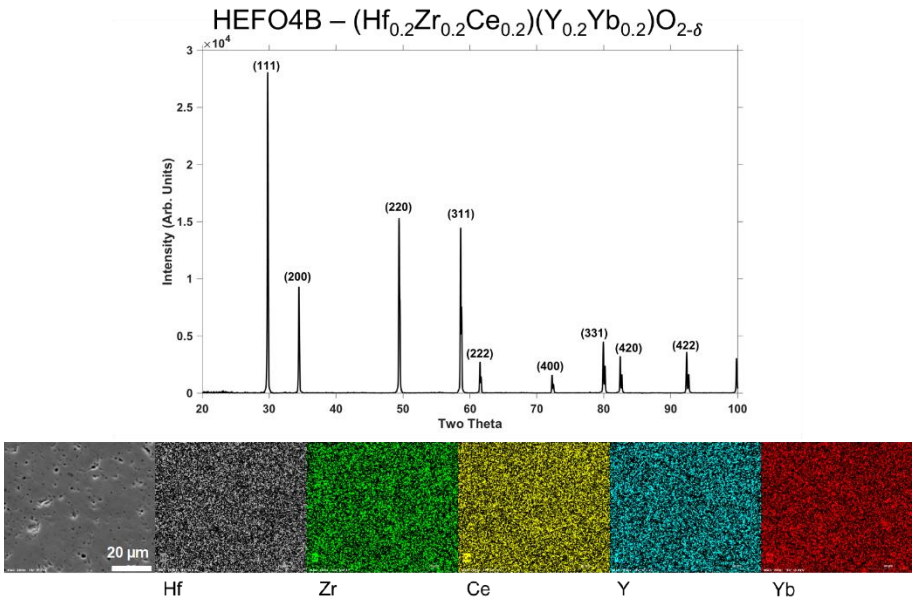

Figure 5.10 HEFO4B: $(Hf_{0.25}Zr_{0.25}Ce_{0.25})(Y_{0.125}Y_{0.125})O_{2-\delta}$: (a) XRD patterns showing phase evolution during the HEBM-SPS fabrication process. (b) Cross-sectional SEM image and the corresponding EDX compositional maps of the specimen after SPS

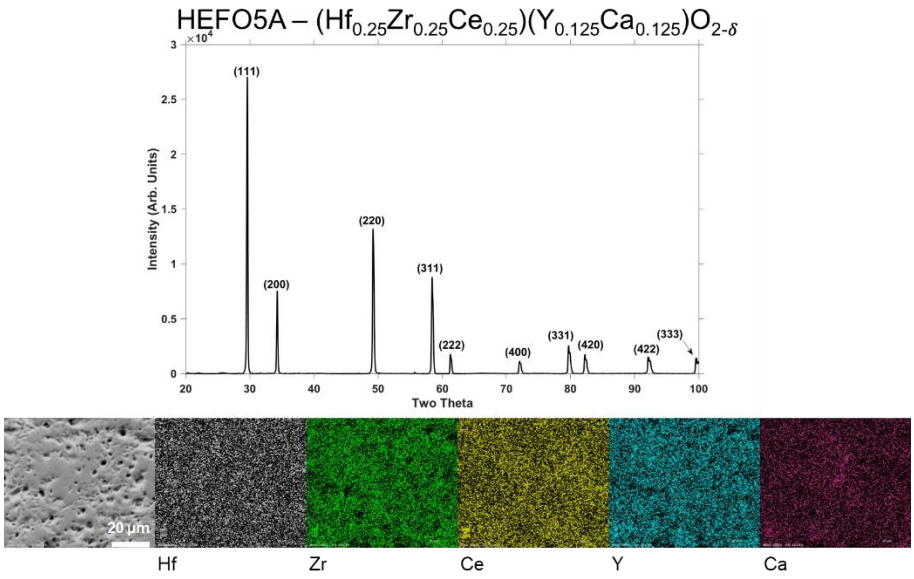

Figure 5.11 HEFO5A: $(Hf_{0.25}Zr_{0.25}Ce_{0.25})(Y_{0.125}Ca_{0.125})O_{2-\delta}$: **(a)** XRD patterns showing phase evolution during the HEBM-SPS fabrication process. **(b)** Cross-sectional SEM image and the corresponding EDX compositional maps of the specimen after SPS

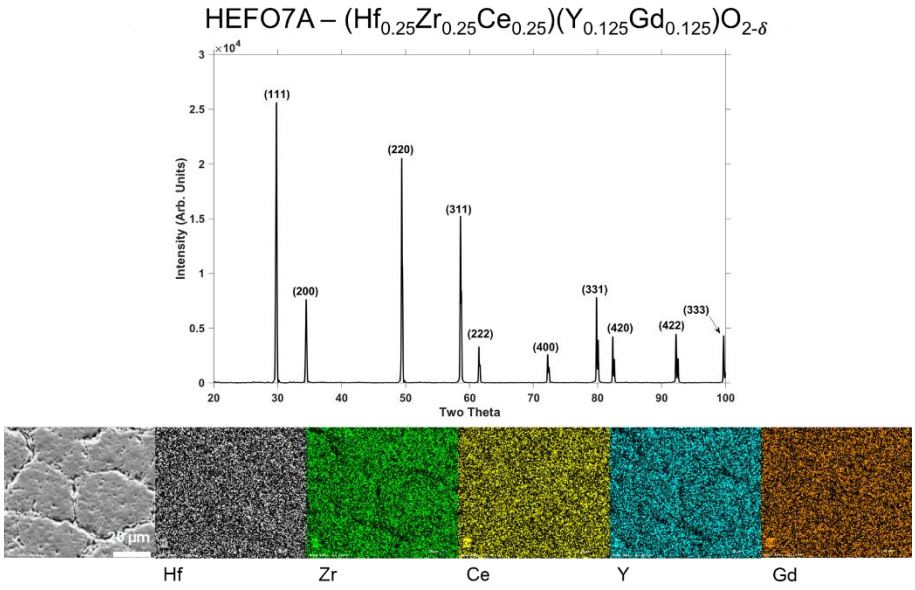

Figure 5.12 HEFO7A: $(Hf_{0.25}Zr_{0.25}Ce_{0.25})(Y_{0.125}Gd_{0.125})O_{2-\delta}$: **(a)** XRD patterns showing phase evolution during the HEBM-SPS fabrication process. **(b)** Cross-sectional SEM image and the corresponding EDX compositional maps of the specimen after SPS

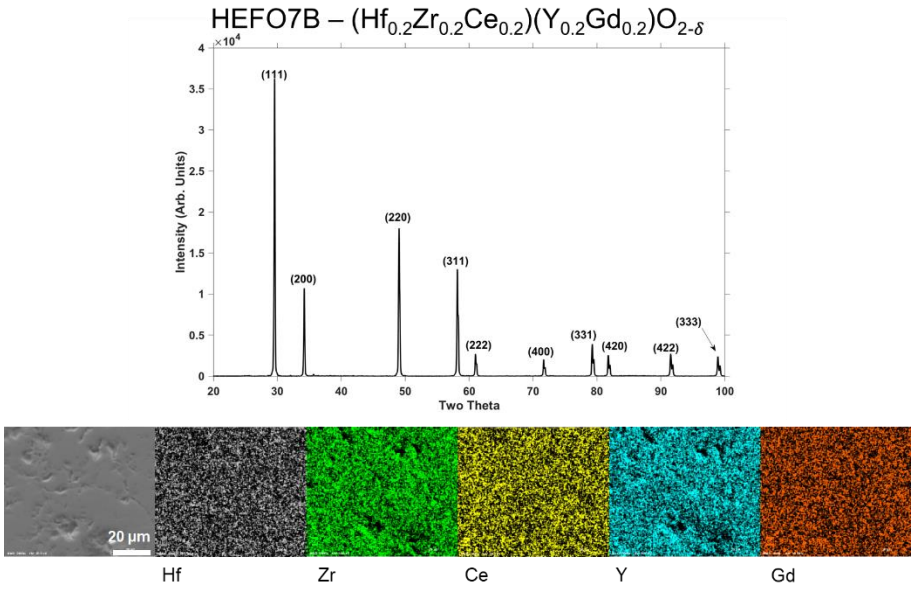

Figure 5.13 HEFO7B: $(Hf_{0.2}Zr_{0.2}Ce_{0.2})(Y_{0.2}Gd_{0.2})O_{2-\delta}$: **(a)** XRD patterns showing phase evolution during the HEBM-SPS fabrication process. **(b)** Cross-sectional SEM image and the corresponding EDX compositional maps of the specimen after SPS

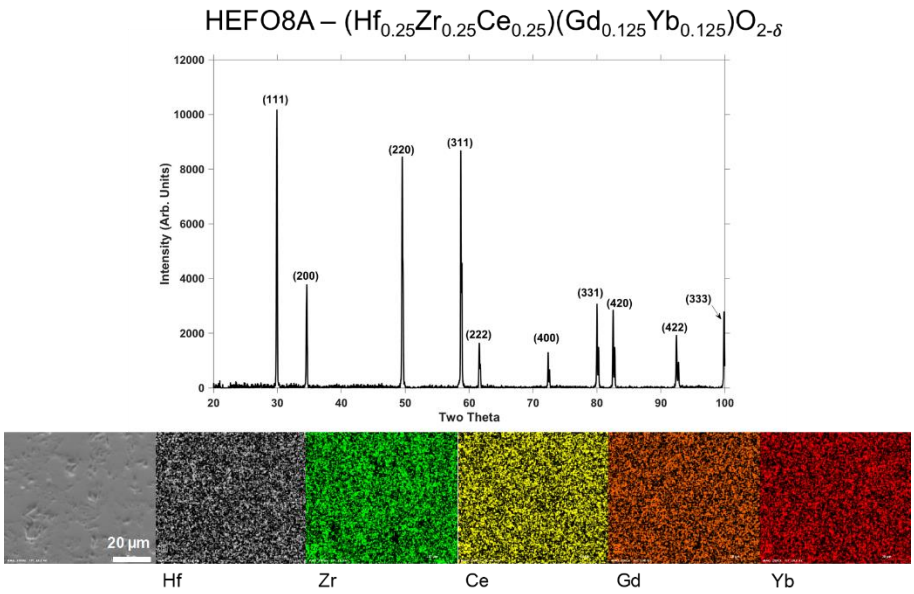

Figure 5.14 HEFO8A: $(Hf_{0.25}Zr_{0.25}Ce_{0.25})(Yb_{0.125}Gd_{0.125})O_{2-\delta}$: **(a)** XRD patterns showing phase evolution during the HEBM-SPS fabrication process. **(b)** Cross-sectional SEM image and the corresponding EDX compositional maps of the specimen after SPS

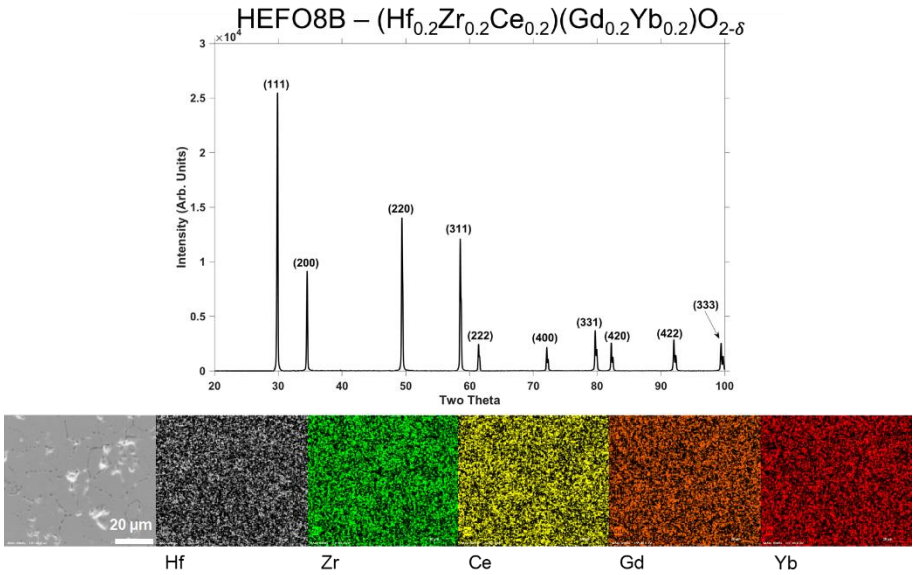

Figure 5.15 HEFO8B: $(Hf_{0.2}Zr_{0.2}Ce_{0.2})(Yb_{0.2}Gd_{0.2})O_{2-\delta}$: **(a)** XRD patterns showing phase evolution during the HEBM-SPS fabrication process. **(b)** Cross-sectional SEM image and the corresponding EDX compositional maps of the specimen after SPS

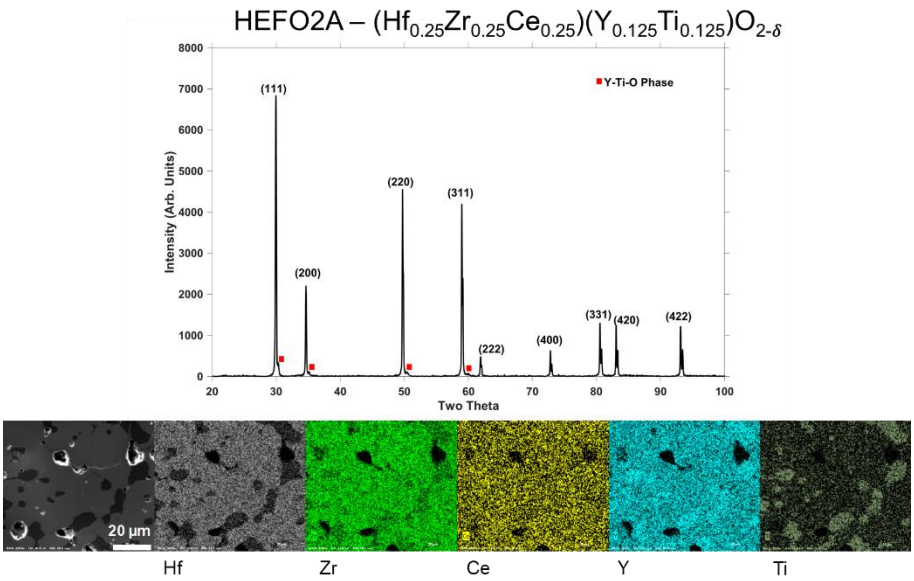

Figure 5.16 HEFO2A: $(Hf_{0.25}Zr_{0.25}Ce_{0.25})(Y_{0.125}Ti_{0.125})O_{2-\delta}$: **(a)** XRD patterns showing phase evolution during the HEBM-SPS fabrication process. **(b)** Cross-sectional SEM image and the corresponding EDX compositional maps of the specimen after SPS

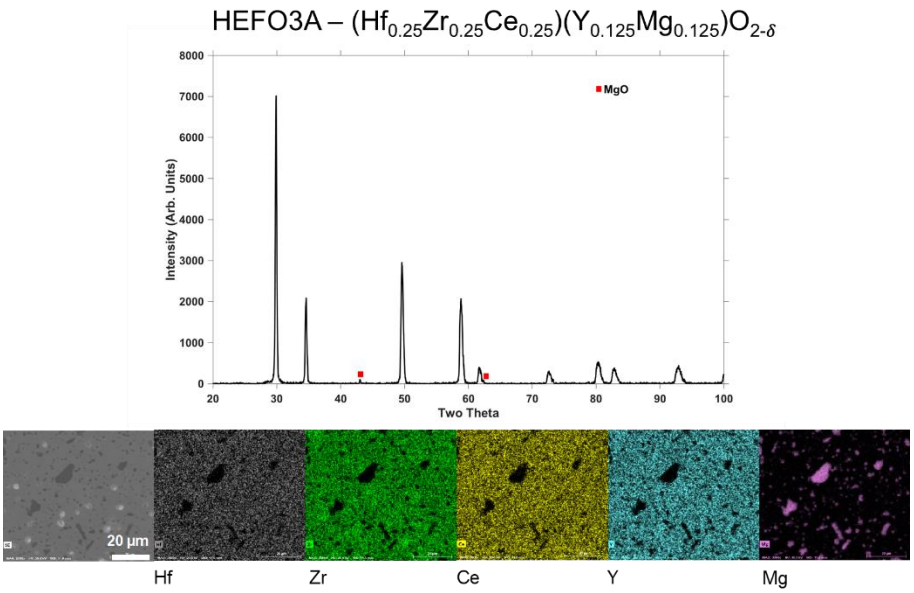

Figure 5.17 HEFO3A: $(Hf_{0.25}Zr_{0.25}Ce_{0.25})(Y_{0.125}Mg_{0.125})O_{2-\delta}$: **(a)** XRD patterns showing phase evolution during the HEBM-SPS fabrication process. **(b)** Cross-sectional SEM image and the corresponding EDX compositional maps of the specimen after SPS

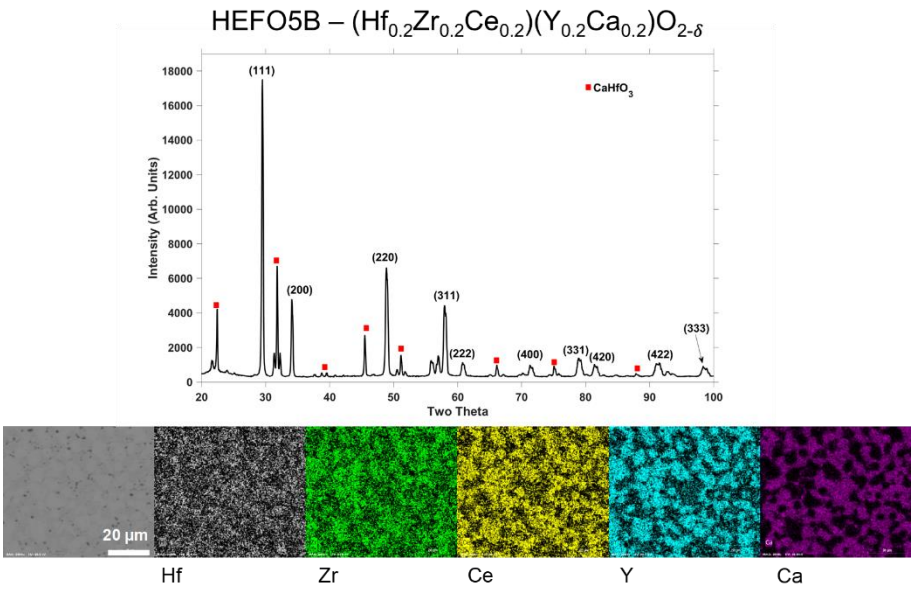

Figure 5.18 HEFO5B: $(Hf_{0.2}Zr_{0.2}Ce_{0.2})(Y_{0.2}Ca_{0.2})O_{2-\delta}$: **(a)** XRD patterns showing phase evolution during the HEBM-SPS fabrication process. **(b)** Cross-sectional SEM image and the corresponding EDX compositional maps of the specimen after SPS

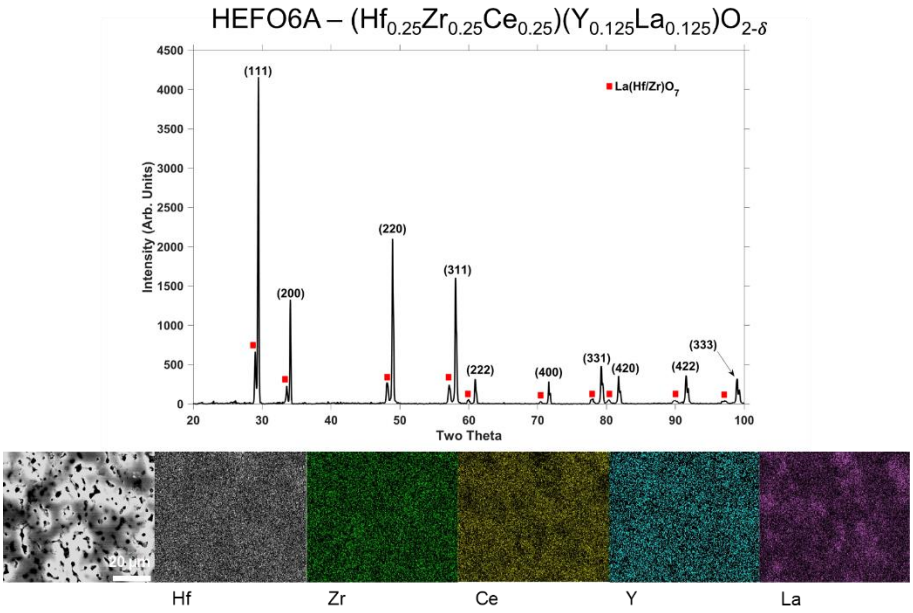

Figure 5.19 HEFO6A: $(Hf_{0.25}Zr_{0.25}Ce_{0.25})(Y_{0.125}La_{0.125})O_{2-\delta}$: **(a)** XRD patterns showing phase evolution during the HEBM-SPS fabrication process. **(b)** Cross-sectional SEM image and the corresponding EDX compositional maps of the specimen after SPS

Table 5.1 All High Entropy Fluorite Oxides (HEFOs) fabricated, along with lattice parameters, densities, thermal conductivities, and Vicker's hardness values.

	Composition	Single Phase ?	Lattice Parameter (Å)	Theoretical Density (g/cm^3)	Relative Density (Annealed)	Thermal Conductivity (W/m·K)	Hardness (GPa)
HEFO1	$(Hf_{0.25}Zr_{0.25}Ce_{0.25})(Y_{0.25})O_{2-\delta}$	Y	5.24	7.22	97.6	1.74 ± 0.15	13.6 ± 0.5
HEFO2A	$(Hf_{0.25}Zr_{0.25}Ce_{0.25})(Y_{0.125}Ti_{0.125})O_{2-\delta}$	N	-	-	-	-	-
HEFO3A	$(Hf_{0.25}Zr_{0.25}Ce_{0.25})(Y_{0.125}Mg_{0.125})O_{2-\delta}$	N	-	-	-	-	-
HEFO4A	$(Hf_{0.25}Zr_{0.25}Ce_{0.25})(Y_{0.125}Yb_{0.125})O_{2-\delta}$	Y	5.23	7.68	100	1.55 ± 0.20	12.7 ± 0.7
HEFO4B	$(Hf_{0.2}Zr_{0.2}Ce_{0.2})(Y_{0.2}Yb_{0.2})O_{2-\delta}$	Y	5.24	7.88	99.3	1.29 ± 0.11	13.3 ± 0.6
HEFO5A	$(Hf_{0.25}Zr_{0.25}Ce_{0.25})(Y_{0.125}Ca_{0.125})O_{2-\delta}$	Y	5.25	7.48	98.3	1.1 ± 0.2	13.3 ± 0.6
HEFO5B	$(Hf_{0.2}Zr_{0.2}Ce_{0.2})(Y_{0.2}Ca_{0.2})O_{2-\delta}$	N	-	-	-	-	-
HEFO6A	$(Hf_{0.25}Zr_{0.25}Ce_{0.25})(Y_{0.125}La_{0.125})O_{2-\delta}$	N	-	-	-	-	-
HEFO7A	$(Hf_{0.25}Zr_{0.25}Ce_{0.25})(Y_{0.125}Gd_{0.125})O_{2-\delta}$	Y	5.25	9.22	96.0	1.17 ± 0.13	13.2 ± 0.5
HEFO7B	$(Hf_{0.2}Zr_{0.2}Ce_{0.2})(Y_{0.2}Gd_{0.2})O_{2-\delta}$	Y	5.28	9.87	99.0	1.61 ± 0.13	13.1 ± 0.5
HEFO8A	$(Hf_{0.25}Zr_{0.25}Ce_{0.25})(Yb_{0.125}Gd_{0.125})O_{2-\delta}$	Y	5.25	10.19	98.7	1.81 ± 0.14	12.6 ± 0.5
HEFO8B	$(Hf_{0.2}Zr_{0.2}Ce_{0.2})(Yb_{0.2}Gd_{0.2})O_{2-\delta}$	Y	5.27	11.52	98.7	1.62 ± 0.13	12.3 ± 0.7
8YSZ		Y		6.10	98.8	2.02 ± 0.17	13.2 ± 0.4
Y_2O_3		Y		5.01	99.8	-	6.9 ± 0.3
Yb_2O_3		Y		9.17	94.3	-	5.7 ± 0.3

References

[1] D.B. Miracle, O.N. Senkov, Acta Mater. 122 (2017) 448–511.

[2] J.-W. Yeh, S.-K. Chen, S.-J. Lin, J.-Y. Gan, T.-S. Chin, T.-T. Shun, C.-H. Tsau, S.-Y. Chang, Adv. Eng. Mater. 6 (2004) 299–303.

[3] O.N. Senkov, G.B. Wilks, D.B. Miracle, C.P. Chuang, P.K. Liaw, Intermetallics 18 (2010) 1758–1765.

[4] J.-W. Yeh, S.-J. Lin, T.-S. Chin, J.-Y. Gan, S.-K. Chen, T.-T. Shun, C.-H. Tsau, S.-Y. Chou, Metall. Mater. Trans. A 35 (2004) 2533–2536.

[5] B. Cantor, I.T.H. Chang, P. Knight, A.J.B. Vincent, Mater. Sci. Eng. A 375–377 (2004) 213–218.

[6] C.M. Rost, E. Sachet, T. Borman, A. Moballegh, E.C. Dickey, D. Hou, J.L. Jones, S. Curtarolo, J.-P. Maria, Nat. Commun. 6 (2015) 8485.

[7] D. Bérardan, S. Franger, D. Dragoe, A.K. Meena, N. Dragoe, Phys. Status Solidi RRL – Rapid Res. Lett. 10 (2016) 328–333.

[8] D. Bérardan, S. Franger, A.K. Meena, N. Dragoe, J. Mater. Chem. A 4 (2016) 9536–9541.

[9] V. Braic, A. Vladescu, M. Balaceanu, C.R. Luculescu, M. Braic, Surf. Coat. Technol. 211 (2012) 117–121.

[10] M.-H. Hsieh, M.-H. Tsai, W.-J. Shen, J.-W. Yeh, Surf. Coat. Technol. 221 (2013) 118–123.

[11] J. Gild, Y. Zhang, T. Harrington, S. Jiang, T. Hu, M.C. Quinn, W.M. Mellor, N. Zhou, K. Vecchio, J. Luo, Sci. Rep. 6 (2016) 37946.

[12] S. Jiang, T. Hu, J. Gild, N. Zhou, J. Nie, M. Qin, T. Harrington, K. Vecchio, J. Luo, Scr. Mater. 142 (2017) 116–120.

[13] R. Djenadic, A. Sarkar, O. Clemens, C. Loho, M. Botros, V.S.K. Chakravadhanula, C. Kübel, S.S. Bhattacharya, A.S. Gandhi, H. Hahn, Mater. Res. Lett. 5 (2017) 102–109.

[14] A.G. de la Obra, M.A. Avilés, Y. Torres, E. Chicardi, F.J. Gotor, Int. J. Refract. Met. Hard Mater. 63 (2017) 17–25.

[15] R. Liu, H. Chen, K. Zhao, Y. Qin, B. Jiang, T. Zhang, G. Sha, X. Shi, C. Uher, W. Zhang, L. Chen, Adv. Mater. 29 (2017) n/a-n/a.

[16] X.Q. Cao, R. Vassen, D. Stoever, J. Eur. Ceram. Soc. 24 (2004) 1–10.

[17] S.J. Skinner, J.A. Kilner, Mater. Today 6 (2003) 30–37.

[18] M.N. Tsampas, F.M. Sapountzi, P. Vernoux, Catal. Sci. Technol. 5 (2015) 4884–4900.

[19] Y.-P. Fu, S.-H. Chen, J.-J. Huang, Int. J. Hydrog. Energy 35 (2010) 745–752.

[20] N.M. Sammes, Z. Cai, Solid State Ion. 100 (1997) 39–44.

[21] J. Cho, J. Park, J. An, J. Eur. Ceram. Soc. 37 (2017) 3131–3136.

[22] D.G. Cahill, Rev. Sci. Instrum. 75 (2004) 5119–5122.

[23] A.J. Schmidt, Annu. Rev. Heat Transf. 16 (2013) 159–181.

[24] C. Thomsen, H.J. Maris, J. Tauc, Thin Solid Films 154 (1987) 217–223.

[25] J.L. Braun, P.E. Hopkins, J. Appl. Phys. 121 (2017) 175107.

[26] Y.S. Touloukian, E.H. Buyco, Specific Heat: Metallic Elements and Alloys, IFI/Plenum, New York, 1970.

[27] K.W. Schlichting, N.P. Padture, P.G. Klemens, J. Mater. Sci. 36 (2001) 3003–3010.

[28] A. Giri, J.L. Braun, C.M. Rost, P.E. Hopkins, Scr. Mater. 138 (2017) 134–138.

[29] S.M. Haile, Acta Mater. 51 (2003) 5981–6000.

[30] J.A. Kilner, Solid State Ion. 129 (2000) 13–23.

[31] J. Gong, Y. Li, Z. Tang, Z. Zhang, J. Mater. Sci. 35 (2000) 3547–3551.

[32] X.J. Chen, K.A. Khor, S.H. Chan, L.G. Yu, Mater. Sci. Eng. A 335 (2002) 246–252.

[33] I. Abraham, G. Gritzner, J. Mater. Sci. Lett. 12 (1993) 995–997.

[34] S. Sameshima, T. Ichikawa, M. Kawaminami, Y. Hirata, Mater. Chem. Phys. 61 (1999) 31–35.

[35] T. Sakuma, Y.-I. Yoshizawa, H. Suto, J. Mater. Sci. 20 (1985) 2399–2407.

[36] P. Dahl, I. Kaus, Z. Zhao, M. Johnsson, M. Nygren, K. Wiik, T. Grande, M.-A. Einarsrud, Ceram. Int. 33 (2007) 1603–1610.

[37] M. Mazaheri, M. Valefi, Z.R. Hesabi, S.K. Sadrnezhaad, Ceram. Int. 35 (2009) 13–20.

Chapter 6: A High-Entropy Silicide: $(Mo_{0.2}Nb_{0.2}Ta_{0.2}Ti_{0.2}W_{0.2})Si_2$

6.1 Introduction

Research on high-entropy alloys (HEAs), also known as multiple principal element alloys (MPEAs) or complex concentrated alloys (CCAs), has attracted considerable interest in the last ~15 years due to their unique properties and large compositional space for engineering. [1–8] A majority of the metallic HEAs adopt the simple face-centered cubic (FCC) or body-centered cubic (BCC) crystal structures, and a few hexagonal close packed (HCP) HEAs have also been made. [1–8]

Only in the last ~3.5 years have the ceramic counterparts to the metallic HEAs, or "high-entropy ceramics," been successfully fabricated in bulk forms. In 2015, Rost *et al.* reported an entropy-stabilized oxide, $(Mg_{0.2}Ni_{0.2}Co_{0.2}Cu_{0.2}Zn_{0.2})O$, of a rocksalt structure (with a FCC Bravais lattice). [9] In 2016, high-entropy metal diborides, *e.g.* $(Hf_{0.2}Zr_{0.2}Ta_{0.2}Nb_{0.2}Ti_{0.2})B_2$, were reported as a new class of ultra-high temperature ceramics (UHTCs) and the first high-entropy borides (as well as the first non-oxide high-entropy ceramics made in the bulk form). [10] Subsequently, the research on high-entropy ceramics has made rapid progresses and attracted increasing attention. First, the high-entropy (entropy-stabilized) rocksalt oxides have been studied extensively due to their great potentials as functional materials with low thermal conductivities and colossal dielectric constants, as well as their potential applications in lithium-ion batteries. [11–16] Second, high-entropy metal diborides have also been studied by many groups as a new class of promising structural ceramics with increased hardness; this line of work has further stimulated the subsequent development of high-entropy metal carbides as another

class of UHTCs with increased hardness by various groups worldwide. Third, several other classes of high-entropy ceramics have also been reported, including perovskite, spinel, defective fluorite-structured, and rare earth oxides, as well as high-entropy nitrides. It is worth noting that the high-entropy oxides, carbides, and nitrides discovered to date all have cubic crystal structures with high symmetries. [17–38] The only exception is the high-entropy metal diborides, which have a hexagonal (AlB_2) crystal structure, yet with a rather high symmetry (P6/mmm). [10]

As an increasing number of high-entropy oxides, borides, carbides, and nitrides have been discovered, this study first reports the synthesis and characterization of a high-entropy silicide: $(Mo_{0.2}Nb_{0.2}Ta_{0.2}Ti_{0.2}W_{0.2})Si_2$, for the first time to our knowledge. [19,21–38] Moreover, this $(Mo_{0.2}Nb_{0.2}Ta_{0.2}Ti_{0.2}W_{0.2})Si_2$ possesses a $CrSi_2$-type hexagonal C40 structure with the ABC stacking sequence (Fig. 1); it represents a more complex crystal structure (with a lower $P6_{222}$ symmetry) in comparison with those reported in prior studies, thereby extending the state of the art for the discovery of new high-entropy materials.

In general, refractory disilicides, particularly $MoSi_2$, are of great interest for high-temperature applications. [39–45] In this study, we have also examined the properties of this new high-entropy $(Mo_{0.2}Nb_{0.2}Ta_{0.2}Ti_{0.2}W_{0.2})Si_2$, showing high hardness (16.7 ± 1.9 GPa nanohardness and 11.6 ± 10.5 Gpa Vickers hardness) and much reduced thermal conductivity (6.9 ± 1.1 W m^{-1} K^{-1}).

6.2 Experimental Procedure

Powders of $MoSi_2$, $NbSi_2$, $TaSi_2$, $TiSi_2$, Wsi_2, and $ZrSi_2$ (99% purity, ≥45 μm; Alfa Aesar) were utilized as starting materials. The raw powders were mixed via high-energy ball milling (HEBM) utilizing a SPEX 8000D mill for 6 hr in a silicon nitride jar with silicon nitride

media. Heptane was used to create a slurry for grinding to prevent caking of the powders and to minimize oxidation in the milling containers. The HEBM was done in 30-minute intervals, interrupted by 10-minute resting pauses to avoid overheating. The powders were then densified into 20-mm diameter disks via spark plasma sintering (SPS, Thermal Technologies, CA, USA) at 1650 °C for 10 min under a uniaxial pressure of 50 MPa; then the pressure was immediately reduced to 10 MPa at a rate of 40 MPa/min at 1650 °C to minimize creep. The chamber was initially pumped down to vacuum of at least 20 mTorr and backfilled with argon for three times prior to the SPS experiments to minimize oxidation and a vacuum was maintained throughout the sintering process. The graphite die was lined with 125 μm thick graphite paper to prevent reaction of the specimen with the die.

The silicide was characterized by X-ray diffraction (XRD) utilizing a Rigaku diffractometer with Cu Kα radiation. Scanning electron microscopy (SEM) was carried out, and the corresponding energy dispersive X-ray (EDX) spectroscopy compositional maps and electron backscatter diffraction (EBSD) maps were collected. The EDX measurements were performed at an e-beam voltage of 20 kV to examine the higher energy peaks of Hf, Ta, and W for minimal convolution of the peaks.

Hardness and modulus measurements were conducted via nano-indentation on a KLA-tencor G200 Nanoindenter (KLA-tencor, CA, USA). Nanohardness measurements were performed according to ISO 14577 under a load of 100 mN. In order to produce more statistically relevant data, the KLA-tencor Express Test software module was employed to enable very large datasets to be generated. Vicker's hardness measurements were performed with a Vickers' diamond indenter at 200 kgf/mm^2 with a hold time of 15 seconds. The indentations were examined for conformation with the ASTM C1327. The indentations averaged 15–20 μm in

width during the testing. Thirty measurements were performed at different locations of the specimen; the mean and standard deviation are reported. The Vickers indentation test was also carried out following the ASTM standard for measuring the microhardness.

Thermal conductivities were measured using time-domain thermoreflectance. [46] A thin Al transducer (84 ± 4 nm) is thermally evaporated onto the sample. Using a Ti:Sapphire laser emitting a train of <200 fs pulses at a central wavelength of 800 nm and a repetition rate of 80 MHz, the output is divided into a pump and probe path. The pump is modulated at 8.4 MHz to heat the sample, while the probe is used to measure the resulting change in temperature as a function of delay time out to 5.5 ns after pump absorption. The pump and probe $1/e^2$ diameters are 15 and 9 μm, respectively. The volumetric heat capacity was taken to be 2.5 ± 3 J cm^{-3} K^{-1} based on the rule of mixtures average of constituent heat capacities. [47]

6.3 Results and Discussion

The XRD pattern shown in Fig. 2 suggests that the $(Mo_{0.2}Nb_{0.2}Ta_{0.2}Ti_{0.2}W_{0.2})Si_2$ specimen made by SPS possesses a hexagonal structure with the space group $P6_{222}$, or the $CrSi_2$ prototype structure. All peaks, except for one very minor peak, in the XRD pattern (Fig. 2) can be indexed to the hexagonal C40 structure with the ABC stacking sequence, as schematically illustrated in Fig. 1. SEM and EDX maps (Fig. 3) further demonstrated that this five-cation $(Mo_{0.2}Nb_{0.2}Ta_{0.2}Ti_{0.2}W_{0.2})Si_2$ specimen indeed formed a homogenous high-entropy solid solution. This hexagonal C40 structure was further confirmed by EBSD of a polished sample surface (Fig. 4). Lattice parameters of this $(Mo_{0.2}Nb_{0.2}Ta_{0.2}Ti_{0.2}W_{0.2})Si_2$ specimen were determined from the XRD to be: a = 4.711 Å and c = 6.522 Å.

The formation of a hexagonal C40 crystal structure (with the ABC stacking sequence, as shown in Fig. 1) for this high-entropy $(Mo_{0.2}Nb_{0.2}Ta_{0.2}Ti_{0.2}W_{0.2})Si_2$ specimen is noteworthy and interesting since only two of the five constituent disilicides, $NbSi_2$ and $TaSi_2$, form this hexagonal structure at high temperatures. [44,48] $TiSi_2$ possesses an orthorhombic structure (with the ABCD stacking sequence). [49] Both $MoSi_2$ and Wsi_2 normally form tetragonal structures (with the AB stacking sequence), though the hexagonal phases were observed at lower temperatures (below 900˚C and 550˚C, respectively) in thin films. [48,50]

This $(Mo_{0.2}Nb_{0.2}Ta_{0.2}Ti_{0.2}W_{0.2})Si_2$ represents a new high-entropy ceramic made, with a new, and perhaps the lowest, symmetry among all high-entropy metals and ceramics reported. To date, all except for two high-entropy metals and ceramics reported have cubic symmetries (of simple FCC and BCC, rocksalt, fluorite, 127erovskite, and spinel structures).[1–9,19,21–31,33–35,37,38,51] The two other classes of non-cubic high-entropy materials reported are the metallic HCP HEAs (with the space group of $P6_3/mmc$) and high-entropy metal diborides (with the space group of P6/mmm). [8,10,20] This high-entropy $(Mo_{0.2}Nb_{0.2}Ta_{0.2}Ti_{0.2}W_{0.2})Si_2$ has a lower symmetry of $P6_{222}$, with a more complex ABC stacking sequence (Fig. 1).

It should be noted that a secondary TiO phase is also present, producing a minor XRD peak as indicated in Fig. 2. We assume that TiO formed because $TiSi_2$ possesses a melting point of ~1500 ˚C, below our SPS temperature; thus, it is likely that $TiSi_2$ promoted the formation a (transient) liquid phase that assisted sintering but captured surface oxides. [52] $TiSi_2$ has been utilized for liquid assisted sintering of diborides in a similar manner. [53–55] The secondary oxide phases seen in the SEM image (the dark phase in the first panel of SEM image in Fig. 3) are likely SiO_2-based glass, which did not show up in XRD (since the amount of TiO identified

by XRD, as shown in Fig. 2, is small). ImageJ analysis of the SEM image was performed to estimate the high-entropy silicide phase to be approximately 89 vol. %.

EBSD was utilized to measure the grain size and examine the texture of the sintered $(Mo_{0.2}Nb_{0.2}Ta_{0.2}Ti_{0.2}W_{0.2})Si_2$ specimen. An average grain size of 5.4 ± 3.3 μm was found from a measurement of over 5000 grains. No significant texturing was evident in the sample. Two EBSD maps at low and high magnifications, an inverse pole figure, and the measured grain size distribution are shown in Fig. 4.

Nanoindentation hardness measurements of this (hexagonal) high-entropy $(Mo_{0.2}Nb_{0.2}Ta_{0.2}Ti_{0.2}W_{0.2})Si_2$ following the ISO 14577 standard using a load of 100 mN produced a value of 16.7 ± 1.9 Gpa with a large number of indents. It also measured an elastic modulus of 421 ± 19 Gpa, in agreement with the measurements taken by Nakamura et al. for $MoSi_2$ and Wsi_2. [56] Moreover, we have conducted Vickers indentation test and measured a microhardness value of 11.6 ± 0.5 Gpa from our high-entropy $(Mo_{0.2}Nb_{0.2}Ta_{0.2}Ti_{0.2}W_{0.2})Si_2$ specimen. These measured hardness values are comparable to those reported for $MoSi_2$ in literature, with Newman et al. reporting up to 17.5 ± 2.0 Gpa in nanoindentation and Vickers hardness in other prior studies varying from approximately 9 to 14 Gpa. [57–61] The microhardness value of our high-entropy $(Mo_{0.2}Nb_{0.2}Ta_{0.2}Ti_{0.2}W_{0.2})Si_2$ specimen is compared with five individual constituent metal disilicides in Table 1. Notably, the Vickers hardness of this high-entropy $(Mo_{0.2}Nb_{0.2}Ta_{0.2}Ti_{0.2}W_{0.2})Si_2$ specimen is higher than the average of the microhardness values of the five individual metal disilicides reported in the literature (which was calculated to be 9.32 Gpa by taking and median value for $MoSi_2$).

A significantly reduced thermal conductivity was measured for this (hexagonal) high-entropy $(Mo_{0.2}Nb_{0.2}Ta_{0.2}Ti_{0.2}W_{0.2})Si_2$, in comparison with other metal disilicides. [61,62] Fitting

a multilayer heat diffusion model to experimental ratio data, the best-fit thermal conductivity was determined to be 6.9 ± 1.1 W m^{-1} K^{-1}. [63] In comparison, the thermal conductivity of the (tetragonal) $MoSi_2$ has been measured to be 65 W m^{-1} K^{-1}. [61] The thermal conductivities of (hexagonal) $NbSi_2$, (hexagonal) $TaSi_2$, (orthorhombic) $TiSi_2$, and (tetragonal) Wsi_2, respectively were measured by Neshpor to be 19.1 W m^{-1} K^{-1}, 21.9 W m^{-1} K^{-1}, 45.9 W m^{-1} K^{-1}, 46.6 W m^{-1} K^{-1}, respectively; these reported values from literature are listed in Table 1 to be compared with our measured thermal conductivity of the high-entropy $(Mo_{0.2}Nb_{0.2}Ta_{0.2}Ti_{0.2}W_{0.2})Si_2$. [62] While it is possible that the presence of oxide contamination and porosity reduces the thermal conductivity of our specimen, the measured value of 6.9 ± 1.1 W m^{-1} K^{-1} is significantly lower than reported values of any of the five constituent disilicides. Noting that $NbSi_2$ and $TaSi_2$, which have the same hexagonal crystal and lowest thermal conductivities of 19.1 W m^{-1} K^{-1} and 21.9 W m^{-1} K^{-1}, respectively, among the five individual disilicides, are perhaps the best benchmarks for comparison. [62] Still, the measured thermal conductivity of this high-entropy $(Mo_{0.2}Nb_{0.2}Ta_{0.2}Ti_{0.2}W_{0.2})Si_2$ is substantial lower (~1/3), presumably due to the high phonon scattering from the five different cations with different masses and a highly distorted lattice. A prior modeling study has demonstrated that >10X reduction in thermal conductivity can be achieved in high-entropy ceramics, and similar levels of thermal conductivity reduction was indeed observed in entropy-stabilized oxides. [12,13]

We also attempted to fabricate a $(Mo_{0.2}Nb_{0.2}Ta_{0.2}W_{0.2}Zr_{0.2})Si_2$ specimen via the same procedure, but it did not form a single high-entropy phase. The measured XRD pattern and EDX elemental maps of this $(Mo_{0.2}Nb_{0.2}Ta_{0.2}W_{0.2}Zr_{0.2})Si_2$ specimen are shown in Fig. 5. While a primary hexagonal C40 phase did form, additional Ta-Zr-Si and Nb-Zr-Si rich secondary phases were observed.

6.4 Conclusions

A high-entropy metal disilicide, $(Mo_{0.2}Nb_{0.2}Ta_{0.2}Ti_{0.2}W_{0.2})Si_2$, was successfully synthesized. It possesses a hexagonal structure with a space group of $P6_{222}$, representing a new high-entropy material family (a high-entropy silicide) and a new non-cubic high-entropy crystal structure made. Characterization by XRD, EDX, and EBSD confirm the presence of a single high-entropy solid-solution phase, albeit some oxide contaminations.

This high-entropy $(Mo_{0.2}Nb_{0.2}Ta_{0.2}Ti_{0.2}W_{0.2})Si_2$ exhibits high nanohardness of 16.7 ± 1.9 Gpa and Vickers hardness of 11.6 ± 10.5 Gpa. The measured thermal conductivity of $(Mo_{0.2}Nb_{0.2}Ta_{0.2}Ti_{0.2}W_{0.2})Si_2$ is 6.9 ± 1.1 W m^{-1} K^{-1}, which is approximately one order of magnitude lower than that of the widely-used tetragonal $MoSi_2$ and ~1/3 of those reported for the hexagonal $NbSi_2$ and $TaSi_2$ with the same crystal structure. [61,62] The significant reduction in the thermal conductivity can be explained from the high phonon scattering in the high-entropy ceramic.

Chapter 6, in full, is a reprint of the material "A high-entropy silicide: $(Mo_{0.2}Nb_{0.2}Ta_{0.2}Ti_{0.2}W_{0.2})Si_2$" as it appears in *Journal of Materiomics*, J. Gild, J. Braun, K. Kaufmann, E. Marin, T. Harrington, P. Hopkins, K. Vecchio, J. Luo, Journal of Materiomics. (2019). The dissertation author was the primary investigator and wrote the first draft of manuscript.

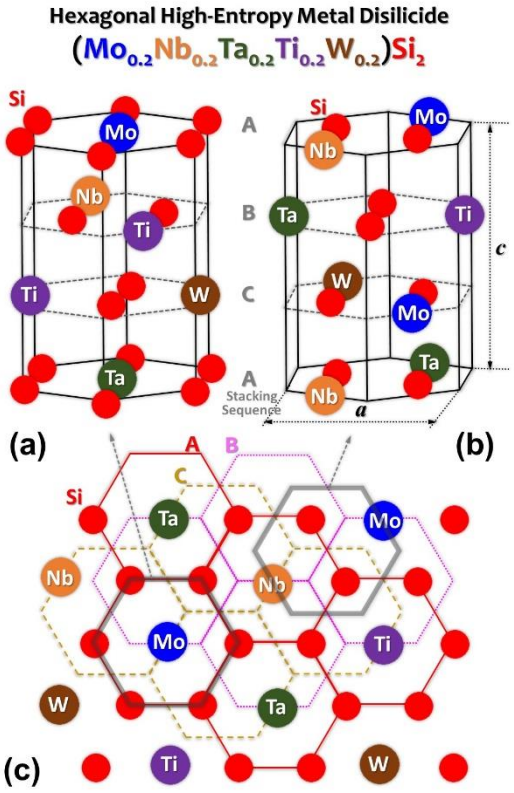

Figure 6.1 Schematic illustration of the atomic structure of the hexagonal high-entropy disilicide with the ABC stacking sequences (*i.e.* the $CrSi_2$ prototype structure). Here, **(a)** and **(b)** are two alternative views of hexagonal cells (but not the unit cells) and **(c)** is an in-plane view, where the positions of both Si and metal atoms are shown for layer A while only the hexagonal Si nets are shown for layers B and C for clarity. The lattice parameters (*a* and *c*) are labeled. Noting that *a* is not the edge of the hexagonal cells shown in (a) and (b), but the distance between two metal cations within the layer.

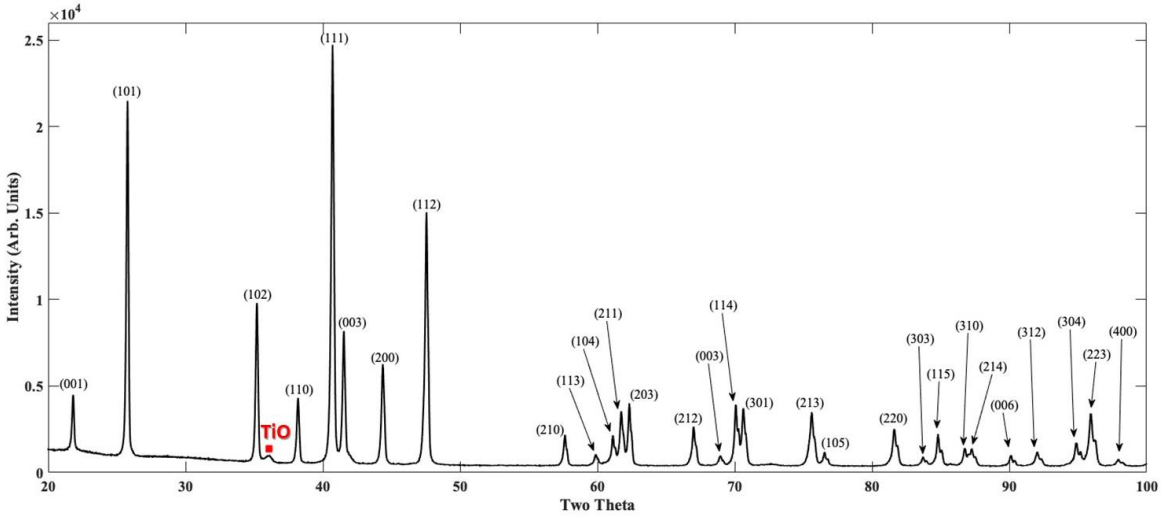

Figure 6.2 XRD pattern of the $(Mo_{0.2}Nb_{0.2}Ta_{0.2}Ti_{0.2}W_{0.2})Si_2$ specimen. Except one minor peak from a secondary hexagonal TiO phase (labeled by the red solid square), all other XRD peaks are indexed to a hexagonal C40 structure (or the $CrSi_2$ prototype structure with the $P6_{222}$ space group and the D_6 point group) with the lattice parameters a = 4.711 Å and c = 6.522 Å.

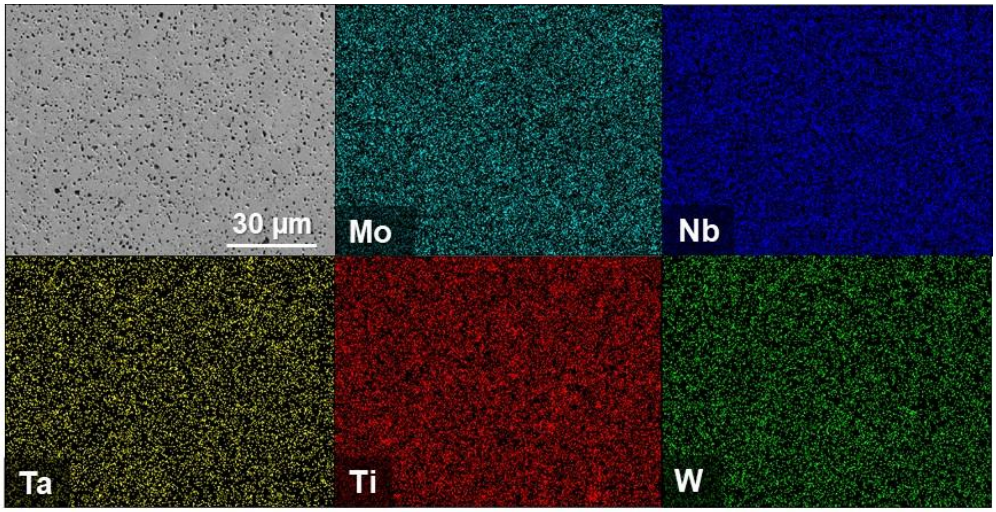

Figure 6.3 SEM micrograph and the corresponding EDX elemental maps of the $(Mo_{0.2}Nb_{0.2}Ta_{0.2}Ti_{0.2}W_{0.2})Si_2$ specimen.

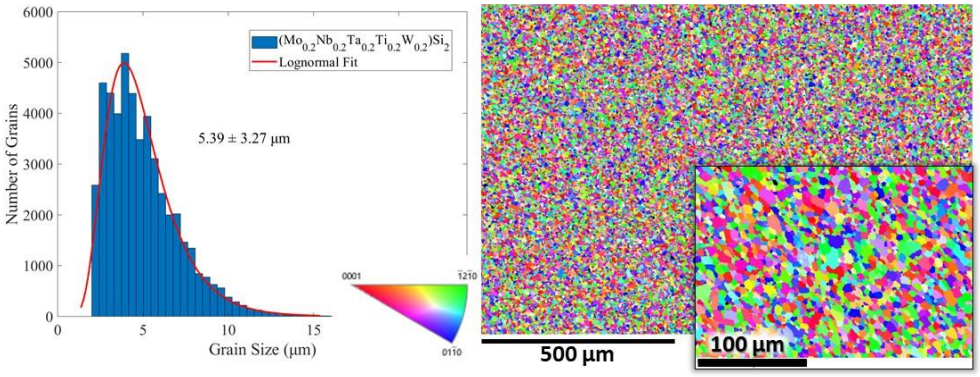

Figure 6.4 EBSD map of >1 mm^2 area of the high-entropy $(Mo_{0.2}Nb_{0.2}Ta_{0.2}Ti_{0.2}W_{0.2})Si_2$ surface, showing a rather uniform microstructure. No significant texture was observed. The measured grain size distribution is given, which fits a lognormal curve. The inset on the right-bottom corner is an additional EBSD map taken at a higher magnification.

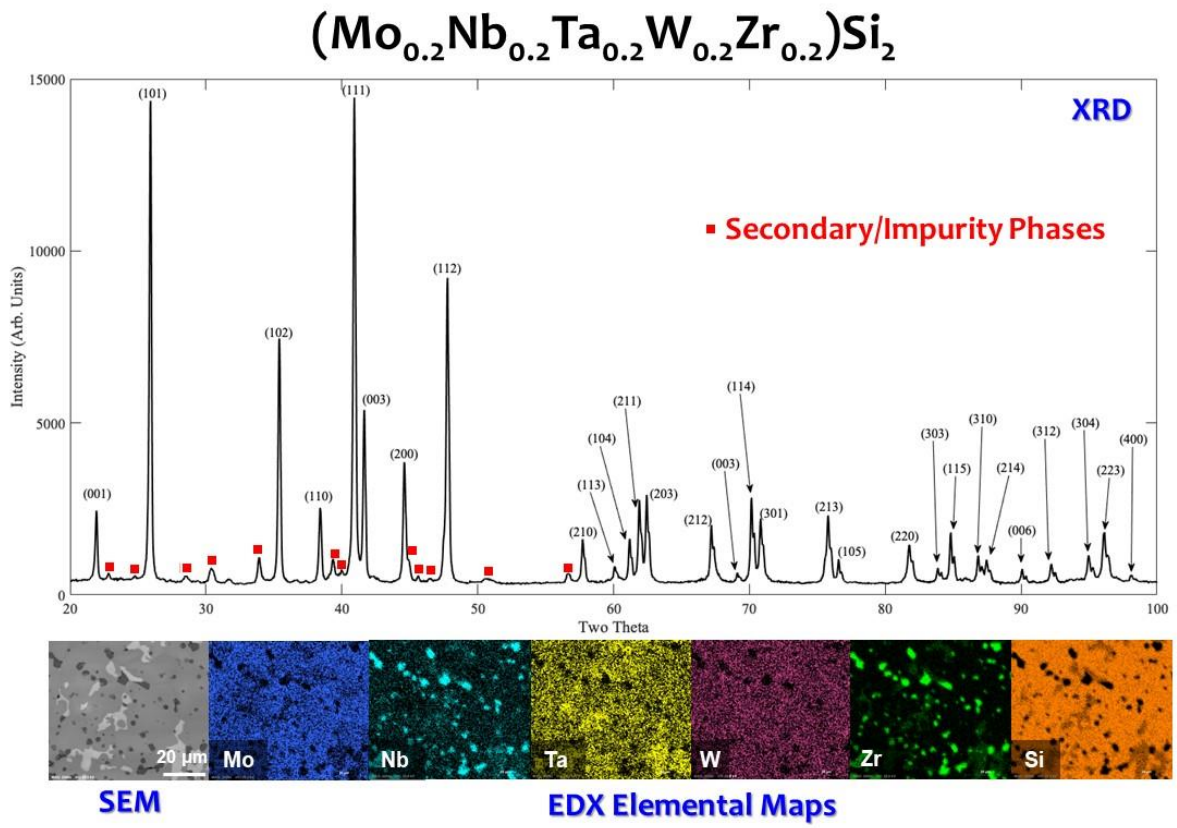

Figure 6.5 XRD pattern, SEM micrograph, and the corresponding EDX elemental maps of the $(Mo_{0.2}Nb_{0.2}Ta_{0.2}W_{0.2}Zr_{0.2})Si_2$ specimen. In addition to a primary hexagonal C40 phase, Ta-Zr-Si and Nb-Zr-Si rich secondary phases were observed.

Table 6.1 Comparison of the properties of the high-entropy $(Mo_{0.2}Nb_{0.2}Ta_{0.2}Ti_{0.2}W_{0.2})Si_2$ with five individual constituent metal disilicides.

Compound	**Crystal Structure**	**Vickers Hardness (Gpa)**	**Young's Modulus (Gpa)**	**Thermal Conductivity [W m^{-1} K^{-1}]**	**References**
$MoSi_2$	Tetragonal	9-14	414	65	[53,54,57]
$NbSi_2$	Hexagonal	5.4	330	19.1	[59,61,62]
$TaSi_2$	Hexagonal	13	338	21.9	[59,62,63]
$TiSi_2$	Orthorhombic	8.5	256	45.9	[59,62,64]
Wsi_2	Tetragonal	8.2	438	46.6	[53,59,62,65]
Rule-of-mixture average of five metal disilicides		9.32	355	40	
$(Mo_{0.2}Nb_{0.2}Ta_{0.2}Ti_{0.2}W_{0.2})Si_2$	Hexagonal	11.6 ± 0.5	421 ± 19	6.9 ± 1.1	This Study

References

[1] M.-H. Tsai, J.-W. Yeh, Mater. Res. Lett. 2 (2014) 107–123.

[2] Y. Zhang, T.T. Zuo, Z. Tang, M.C. Gao, K.A. Dahmen, P.K. Liaw, Z.P. Lu, Prog. Mater. Sci. 61 (2014) 1–93.

[3] B.S. Murty, J.-W. Yeh, S. Ranganathan, High-Entropy Alloys, BH, Butterworth-Heinemann,
an imprint of Elsevier, Amsterdam Boston Heidelberg, 2014.

[4] J.-W. Yeh, S.-K. Chen, S.-J. Lin, J.-Y. Gan, T.-S. Chin, T.-T. Shun, C.-H. Tsau, S.-Y. Chang, Adv. Eng. Mater. 6 (2004) 299–303.

[5] J.-W. Yeh, S.-J. Lin, T.-S. Chin, J.-Y. Gan, S.-K. Chen, T.-T. Shun, C.-H. Tsau, S.-Y. Chou,
Metall. Mater. Trans. A 35 (2004) 2533–2536.

[6] O.N. Senkov, D.B. Miracle, K.J. Chaput, J.-P. Couzinie, J. Mater. Res. 33 (2018) 3092–3128.

[7] B. Cantor, I.T.H. Chang, P. Knight, A.J.B. Vincent, Mater. Sci. Eng. A 375–377 (2004) 213–
218.

[8] D.B. Miracle, O.N. Senkov, Acta Mater. 122 (2017) 448–511.

[9] C.M. Rost, E. Sachet, T. Borman, A. Moballegh, E.C. Dickey, D. Hou, J.L. Jones, S. Curtarolo, J.-P. Maria, Nat. Commun. 6 (2015) 8485.

[10] J. Gild, Y. Zhang, T. Harrington, S. Jiang, T. Hu, M.C. Quinn, W.M. Mellor, N. Zhou, K. Vecchio, J. Luo, Sci. Rep. 6 (2016) 37946.

[11] A. Giri, J.L. Braun, P.E. Hopkins, J. Appl. Phys. 123 (2018) 015106.

[12] J.L. Braun, C.M. Rost, M. Lim, A. Giri, D.H. Olson, G.N. Kotsonis, G. Stan, D.W. Brenner, J.-P. Maria, P.E. Hopkins, Adv. Mater. 0 (n.d.) 1805004.

[13] A. Giri, J.L. Braun, C.M. Rost, P.E. Hopkins, Scr. Mater. 138 (2017) 134–138.

[14] D. Bérardan, S. Franger, D. Dragoe, A.K. Meena, N. Dragoe, Phys. Status Solidi RRL – Rapid Res. Lett. 10 (2016) 328–333.

[15] A. Sarkar, C. Loho, L. Velasco, T. Thomas, S.S. Bhattacharya, H. Hahn, R. Djenadic, Dalton Trans. 46 (2017) 12167–12176.

[16] D. Bérardan, S. Franger, A.K. Meena, N. Dragoe, J. Mater. Chem. A 4 (2016) 9536–9541.

[17] G. Tallarita, R. Licheri, S. Garroni, R. Orrù, G. Cao, Scr. Mater. 158 (2019) 100–104.

[18] A. Mansouri Tehrani, J. Brgoch, J. Solid State Chem. 271 (2019) 47–58.

[19] T.J. Harrington, J. Gild, P. Sarker, C. Toher, C.M. Rost, O.F. Dippo, C. McElfresh, K. Kaufmann, E. Marin, L. Borowski, P.E. Hopkins, J. Luo, S. Curtarolo, D.W. Brenner, K.S. Vecchio, Acta Mater. 166 (2019) 271–280.

[20] P.H. Mayrhofer, A. Kirnbauer, Ph. Ertelthaler, C.M. Koller, Scr. Mater. 149 (2018) 93–97.

[21] J. Zhou, J. Zhang, F. Zhang, B. Niu, L. Lei, W. Wang, Ceram. Int. (2018).

[22] X. Yan, L. Constantin, Y. Lu, J.-F. Silvain, M. Nastasi, B. Cui, J. Am. Ceram. Soc. 101 (2018) 4486–4491.

[23] P. Sarker, T. Harrington, C. Toher, C. Oses, M. Samiee, J.-P. Maria, D.W. Brenner, K.S. Vecchio, S. Curtarolo, Nat. Commun. 9 (2018) 4980.

[24] E. Castle, T. Csanádi, S. Grasso, J. Dusza, M. Reece, Sci. Rep. 8 (2018) 8609.

[25] J. Dusza, P. Švec, V. Girman, R. Sedlák, E.G. Castle, T. Csanádi, A. Kovalčíková, M.J. Reece, J. Eur. Ceram. Soc. (2018) 4303–4307.

[26] D. Demirskyi, H. Borodianska, T.S. Suzuki, Y. Sakka, K. Yoshimi, O. Vasylkiv, Scr. Mater. 164 (2019) 12–16.

[27] Y. Yang, W. Wang, G.-Y. Gan, X.-F. Shi, B.-Y. Tang, Phys. B Condens. Matter 550 (2018) 163–170.

[28] B. Ye, T. Wen, K. Huang, C.-Z. Wang, Y. Chu, J. Am. Ceram. Soc. 0 (n.d.).

[29] L. Feng, W.G. Fahrenholtz, G.E. Hilmas, Y. Zhou, Scr. Mater. 162 (2019) 90–93.

[30] S. Jiang, T. Hu, J. Gild, N. Zhou, J. Nie, M. Qin, T. Harrington, K. Vecchio, J. Luo, Scr. Mater. 142 (2017) 116–120.

[31] Y. Sharma, B.L. Musico, X. Gao, C. Hua, A.F. May, A. Herklotz, A. Rastogi, D. Mandrus, J. Yan, H.N. Lee, M.F. Chisholm, V. Keppens, T.Z. Ward, Phys. Rev. Mater. 2 (2018) 060404.

[32] A. Sarkar, L. Velasco, D. Wang, Q. Wang, G. Talasila, L. de Biasi, C. Kübel, T. Brezesinski, S.S. Bhattacharya, H. Hahn, B. Breitung, Nat. Commun. 9 (2018) 3400.

[33] J. Dąbrowa, M. Stygar, A. Mikuła, A. Knapik, K. Mroczka, W. Tejchman, M. Danielewski, M. Martin, Mater. Lett. 216 (2018) 32–36.

[34] J. Gild, M. Samiee, J.L. Braun, T. Harrington, H. Vega, P.E. Hopkins, K. Vecchio, J. Luo, J. Eur. Ceram. Soc. 38 (2018) 3578–3584.

[35] K. Chen, X. Pei, L. Tang, H. Cheng, Z. Li, C. Li, X. Zhang, L. An, J. Eur. Ceram. Soc. 38 (2018) 4161–4164.

[36] R. Djenadic, A. Sarkar, O. Clemens, C. Loho, M. Botros, V.S.K. Chakravadhanula, C. Kübel, S.S. Bhattacharya, A.S. Gandhi, H. Hahn, Mater. Res. Lett. 5 (2017) 102–109.

[37] T. Jin, X. Sang, R.R. Unocic, R.T. Kinch, X. Liu, J. Hu, H. Liu, S. Dai, Adv. Mater. 30 (2018) 1707512.

[38] V. Braic, A. Vladescu, M. Balaceanu, C.R. Luculescu, M. Braic, Surf. Coat. Technol. 211 (2012) 117–121.

[39] J.J. Petrovic, MRS Bull. 18 (1993) 35–41.

[40] J.J. Petrovic, Mater. Sci. Eng. A 192–193 (1995) 31–37.

[41] J.J. Petrovic, A.K. Vasudevan, MRS Online Proc. Libr. Arch. 322 (1993).

[42] S.V. Raj, Mater. Sci. Eng. A 192 (1995) 583–589.

[43] G.V. Samsonov, V.A. Lavrenko, L.A. Glebov, Sov. Powder Metall. Met. Ceram. 13 (1974) 232–235.

[44] B. Song, P. Feng, J. Wang, Y. Ge, G. Wu, X. Wang, F. Akhtar, Corros. Sci. 85 (2014) 311–317.

[45] Z. Yao, J. Stiglich, T.S. Sudarshan, J. Mater. Eng. Perform. 8 (1999) 291–304.

[46] P. Jiang, X. Qian, R. Yang, J. Appl. Phys. 124 (2018) 161103.

[47] Y.S. Touloukian, T. Makita, Thermophysical Properties of Matter – the TPRC Data Series. Volume 6S. Specific Heat – Nonmetallic Liquids and Gases, THERMOPHYSICAL AND ELECTRONIC PROPERTIES INFORMATION ANALYSIS CENTER LAFAYETTE IN, 1976.

[48] F.M. d'Heurle, C.S. Petersson, M.Y. Tsai, J. Appl. Phys. 51 (1980) 5976–5980.

[49] W. Jeitschko, Acta Crystallogr. Sect. B 33 (1977) 2347–2348.

[50] S.P. Murarka, M.H. Read, C.C. Chang, J. Appl. Phys. 52 (1981) 7450–7452.

[51] A. Sarkar, R. Djenadic, D. Wang, C. Hein, R. Kautenburger, O. Clemens, H. Hahn, J. Eur. Ceram. Soc. (2017).

[52] G. Frommeyer, R. Rosenkranz, in: O.N. Senkov, D.B. Miracle, S.A. Firstov (Eds.), Met. Mater. High Struct. Effic., Springer Netherlands, 2004, pp. 287–308.

[53] G.B. Raju, B. Basu, J. Am. Ceram. Soc. 90 (2007) 3415–3423.

[54] J.K. Sonber, T.S.R.Ch. Murthy, C. Subramanian, S. Kumar, R.K. Fotedar, A.K. Suri, Int. J. Refract. Met. Hard Mater. 28 (2010) 201–210.

[55] J.K. Sonber, T.S.R.Ch. Murthy, C. Subramanian, S. Kumar, R.K. Fotedar, A.K. Suri, Int. J. Refract. Met. Hard Mater. 29 (2011) 21–30.

[56] M. Nakamura, S. Matsumoto, T. Hirano, J. Mater. Sci. 25 (1990) 3309–3313.

[57] A. Newman, T. Jewett, S. Sampath, C. Berndt, H. Herman, J. Mater. Res. 13 (1998) 2662–2671.

[58] M.S. Haji-Mahmood, L.S. Chumbley, Nanostructured Mater. 7 (1996) 95–112.

[59] R.B. Schwarz, S.R. Srinivasan, J.J. Petrovic, C.J. Maggiore, Mater. Sci. Eng. A 155 (1992) 75–83.

[60] R.K. Wade, J.J. Petrovic, J. Am. Ceram. Soc. 75 (1992) 3160–3162.

[61] A.K. Vasudévan, J.J. Petrovic, Mater. Sci. Eng. A 155 (1992) 1–17.

[62] V.S. Neshpor, J. Eng. Phys. 15 (1968) 750–752.

[63] D.G. Cahill, Rev. Sci. Instrum. 75 (2004) 5119–5122.

Chapter 7. Summary and Future Work

In this work, the synthesis and formation of a large variety of high entropy ceramics via multiple fabrication and densification methods is investigated.

In the second chapter, the fabrication of high entropy diborides via mechanical alloying and subsequent densification via spark plasma sintering is investigated. Six five-component high entropy diborides were found to be stable in a single phase – $(Hf_{0.2}Zr_{0.2}Ti_{0.2}Ta_{0.2}Nb_{0.2})B_2$, $(Hf_{0.2}Zr_{0.2}Ti_{0.2}Ta_{0.2}Mo_{0.2})B_2$, $(Hf_{0.2}Zr_{0.2}Ti_{0.2}Mo_{0.2}Nb_{0.2})B_2$, $(Hf_{0.2}Mo_{0.2}Ti_{0.2}Ta_{0.2}Nb_{0.2})B_2$, $(Mo_{0.2}Zr_{0.2}Ti_{0.2}Ta_{0.2}Nb_{0.2})B_2$, and $(Hf_{0.2}Zr_{0.2}Ti_{0.2}Ta_{0.2}Cr_{0.2})B_2$ with an AlB_2 hexagonal crystal lattice were successfully formed. $(Hf_{0.2}Zr_{0.2}Ti_{0.2}Mo_{0.2}W_{0.2})B_2$ was attempted but formed a dual phase microstructure with a predominant AlB_2 structure and a secondary $(Ti_{1.6}W_{2.4})B_4$ lattice of the CrB type forming as well. The formation of a homogenous single phase structure was confirmed via both traditional electron dispersive spectroscopy but also transmission electron microscopy. Despite the inclusion of $(Hf/Zr)O_2$ in the microstructure and a maximum of 93% density, the high entropy diborides showed superior hardness compared to any constituent diboride fabricated via the same manner and superior oxidation results to them all with the exception of HfB_2.

In the third chapter, the fabrication of high entropy diborides and carbides along with graphite via flash spark plasma sintering was explored. $(Hf_{0.2}Zr_{0.2}Ti_{0.2}Ta_{0.2}Nb_{0.2})B_2$ and $(Hf_{0.2}Zr_{0.2}Ti_{0.2}Ta_{0.2}Nb_{0.2})C$ were sintered to high density in 90 seconds under 30% power (≈1000A) output of a spark plasma sintering device under 5 MPa of pressure. The minimal amount of time necessary was surprising considering the very high melting temperature of these

compounds and the theoretical sluggish diffusion of high entropy materials. The presence of a carbon sintering aid, likely for the removal of surface oxides, was found to be vital for the homogenization of the high entropy diborides regardless of the amount of power applied.

In the fourth chapter, the fabrication of high entropy diboride powder via the reduction of metal oxides with boron carbide and graphite and subsequent densification via spark plasma sintering is examined. Four compositions, $(Hf_{0.2}Zr_{0.2}Ti_{0.2}Ta_{0.2}Nb_{0.2})B_2$, $(Hf_{0.2}Zr_{0.2}Ti_{0.2}Ta_{0.2}Mo_{0.2})B_2$, $(Hf_{0.2}Zr_{0.2}Ti_{0.2}Ta_{0.2}Cr_{0.2})B_2$, and $(Hf_{0.2}Mo_{0.2}Ti_{0.2}Mo_{0.2}W_{0.2})B_2$ were synthesized with first three forming a single homogeneous phase with the AlB_2 structure with fully density (>99%). The fourth composition, $(Hf_{0.2}Mo_{0.2}Ti_{0.2}Mo_{0.2}W_{0.2})B_2$, achieved a similar density but with the presence of a secondary Mo-W rich tetraboride orthorhombic phase of the CrB type. The lab synthesized powder derived samples showed superior hardness compared to the samples previously sintered with commercial powder (as discussed in chapter 2). The single phase compositions showed reduced thermal conductivity compared to constituent diborides, consistent with what is commonly observed in high entropy materials.

In the fifth chapter, eleven five-component fluorite high entropy oxides from seven oxide components were fabricated. Eight of the compositions, namely $(Hf_{0.25}Zr_{0.25}Ce_{0.25}Y_{0.25})O_{2-\delta}$, $(Hf_{0.25}Zr_{0.25}Ce_{0.25})(Y_{0.125}Yb_{0.125})O_{2-\delta}$, $(Hf_{0.2}Zr_{0.2}Ce_{0.2})(Y_{0.2}Yb_{0.2})O_{2-\delta}$, $(Hf_{0.25}Zr_{0.25}Ce_{0.25})(Y_{0.125}Ca_{0.125})O_{2-\delta}$, $(Hf_{0.25}Zr_{0.25}Ce_{0.25})(Y_{0.125}Gd_{0.125})O_{2-\delta}$, $(Hf_{0.2}Zr_{0.2}Ce_{0.2})(Y_{0.2}Gd_{0.2})O_{2-\delta}$, $(Hf_{0.25}Zr_{0.25}Ce_{0.25})(Yb_{0.125}Gd_{0.125})O_{2-\delta}$, $(Hf_{0.2}Zr_{0.2}Ce_{0.2})(Yb_{0.2}Gd_{0.2})O_{2-\delta}$ formed a single, homogenous, fluorite structure. All of the compositions can be fabricated to high densities by high energy ball milling of the powder, spark plasma sintering, and annealing in open air post SPS. The samples show increased hardness compared to constituent materials as well as reduced thermal and ionic conductivities compared

to 8YSZ. The high entropy materials possess significantly smaller grain sizes than 8YSZ as well, possibly suggesting sluggish diffusion.

In the sixth chapter, two high entropy disilicide compositions were examined - $(Mo_{0.2}Nb_{0.2}Ta_{0.2}Ti_{0.2}W_{0.2})Si_2$, $(Mo_{0.2}Nb_{0.2}Ta_{0.2}W_{0.2}Zr_{0.2})Si_2$. $(Mo_{0.2}Nb_{0.2}Ta_{0.2}Ti_{0.2}W_{0.2})Si_2$ homogenized into a single phase hexagonal C40 structure while $(Mo_{0.2}Nb_{0.2}Ta_{0.2}W_{0.2}Zr_{0.2})Si_2$ formed secondary Ta-Zr-Si and Nb-Zr-Si rich laves phases which led to low temperature melting. $(Mo_{0.2}Nb_{0.2}Ta_{0.2}Ti_{0.2}W_{0.2})Si_2$ showed superior nano and Vickers hardness compared to the rule of mixtures for its constituent disilicides and thermal conductivity an order of magnitude lower than $MoSi_2$. It is noteworthy that only two of the five constituent disilicides, $NbSi_2$ and $TaSi_2$ form this structure at high temperatures, suggesting at least partial entropic stabilization.

High entropy ceramics is still a burgeoning new field with a great deal of potential new research. Future work into both the mechanical properties for structural materials such as refractory diboride and carbides will be needed for their full implementation as well as chemical properties such as oxidation resistance. Research into the fundamental reasons behind lowered thermal conductivity, increased hardness, and other commonplace properties of these high entropy materials is ripe for investigation as well.

References:

[1] D.B. Miracle, O.N. Senkov, Acta Mater. 122 (2017) 448–511.

[2] M.-H. Tsai, J.-W. Yeh, Mater. Res. Lett. 2 (2014) 107–123.

[3] B. Cantor, I.T.H. Chang, P. Knight, A.J.B. Vincent, Mater. Sci. Eng. A 375–377 (2004) 213–218.

[4] X. Yang, S.Y. Chen, J.D. Cotton, Y. Zhang, JOM 66 (2014) 2009–2020.

[5] V.H. Hammond, M.A. Atwater, K.A. Darling, H.Q. Nguyen, L.J. Kecskes, JOM 66 (2014) 2021–2029.

[6] C.-M. Lin, C.-C. Juan, C.-H. Chang, C.-W. Tsai, J.-W. Yeh, J. Alloys Compd. 624 (2015) 100–107.

[7] A. Takeuchi, K. Amiya, T. Wada, K. Yubuta, W. Zhang, JOM 66 (2014) 1984–1992.

[8] O.N. Senkov, G.B. Wilks, D.B. Miracle, C.P. Chuang, P.K. Liaw, Intermetallics 18 (2010) 1758–1765.

[9] O.N. Senkov, J.M. Scott, S.V. Senkova, D.B. Miracle, C.F. Woodward, J. Alloys Compd. 509 (2011) 6043–6048.

[10] O.N. Senkov, S.V. Senkova, D.B. Miracle, C. Woodward, Mater. Sci. Eng. A 565 (2013) 51–62.

[11] É. Fazakas, V. Zadorozhnyy, L.K. Varga, A. Inoue, D.V. Louzguine-Luzgin, F. Tian, L. Vitos, Int. J. Refract. Met. Hard Mater. 47 (2014) 131–138.

[12] C.M. Rost, E. Sachet, T. Borman, A. Moballegh, E.C. Dickey, D. Hou, J.L. Jones, S. Curtarolo, J.-P. Maria, Nat. Commun. 6 (2015) 8485.

[13] D. Bérardan, S. Franger, D. Dragoe, A.K. Meena, N. Dragoe, Phys. Status Solidi RRL – Rapid Res. Lett. 10 (2016) 328–333.

[14] D. Bérardan, S. Franger, A.K. Meena, N. Dragoe, J. Mater. Chem. A 4 (2016) 9536–9541.

[15] N. Qiu, H. Chen, Z. Yang, S. Sun, Y. Wang, Y. Cui, J. Alloys Compd. 777 (2019) 767–774.

[16] W.G. Fahrenholtz, G.E. Hilmas, I.G. Talmy, J.A. Zaykoski, J. Am. Ceram. Soc. 90 (2007) 1347–1364.

[17] A.M. Prokhorov, N.P. Lyakishev, G.S. Burkhanov, V.A. Dement'ev, Inorg. Mater. 32 (2015) 1195–1201.

[18] S.-H. Jung, H.-C. Oh, J.-H. Kim, S.-C. Choi, S.-H. Lee, H.-D. Kim, J. Alloys Compd. 548 (2013) 173–179.

[19] E. Neuman, W. Fahrenholtz, G. Hilmas, Int. J. Appl. Ceram. Technol. 14 (2017) 636–643.

[20] F. Monteverde, L. Silvestroni, Mater. Des. 109 (2016) 396–407.

[21] F. Monteverde, J. Mater. Sci. 43 (2007) 1002–1007.

[22] F. Monteverde, J. Alloys Compd. 428 (2007) 197–205.

[23] E. Zapata-Solvas, D.D. Jayaseelan, H.T. Lin, P. Brown, W.E. Lee, J. Eur. Ceram. Soc. 33 (2013) 1373–1386.

[24] M. Zhang, H. Wang, H. Wang, T. Cui, Y. Ma, J. Phys. Chem. C 114 (2010) 6722–6725.

[25] M. Khoeini, A. Nemati, M. Zakeri, M. Tamizifar, H. Samadi, Ceram. Int. 41 (2015) 11456–11463.

[26] D. Liu, Y. Chu, S. Jing, B. Ye, X. Zhou, J. Am. Ceram. Soc. 101 (2018).

[27] W.-M. Guo, D.-W. Tan, L.-Y. Zeng, Hao-Li, H.-T. Lin, C.-Y. Wang, Ceram. Int. 44 (2018) 4473–4477.

[28] G.S. An, J.S. Han, J.U. Hur, S.-C. Choi, Ceram. Int. 43 (2017) 5896–5900.

[29] D.-W. Ni, G.-J. Zhang, Y.-M. Kan, P.-L. Wang, J. Am. Ceram. Soc. 91 (2008) 2709–2712.

[30] W.-M. Guo, Z.-G. Yang, G.-J. Zhang, Mater. Lett. 83 (2012) 52–55.

[31] R. Licheri, C. Musa, R. Orrù, G. Cao, D. Sciti, L. Silvestroni, J. Alloys Compd. 663 (2016) 351–359.

[32] A.M. Locci, R. Licheri, R. Orrù, G. Cao, Ceram. Int. 35 (2009) 397–400.

[33] X.Q. Cao, R. Vassen, D. Stoever, J. Eur. Ceram. Soc. 24 (2004) 1–10.

[34] J. Cho, J. Park, J. An, J. Eur. Ceram. Soc. 37 (2017) 3131–3136.

[35] Z.-G. Liu, J.-H. Ouyang, Y. Zhou, Mater. Lett. 62 (2008) 3524–3526.

[36] J.A. Kilner, Solid State Ion. 129 (2000) 13–23.

[37] Y.-P. Fu, S.-H. Chen, J.-J. Huang, Int. J. Hydrog. Energy 35 (2010) 745–752.

[38] N.M. Sammes, Z. Cai, Solid State Ion. 100 (1997) 39–44.

[39] S.J. Skinner, J.A. Kilner, Mater. Today 6 (2003) 30–37.

[40] J. Gild, M. Samiee, J.L. Braun, T. Harrington, H. Vega, P.E. Hopkins, K. Vecchio, J. Luo, J. Eur. Ceram. Soc. 38 (2018) 3578–3584.

[41] M.D. Novak, C.G. Levi, in: American Society of Mechanical Engineers, 2007, pp. 261–267.

[42] T.M. Butler, M.L. Weaver, J. Alloys Compd. 674 (2016) 229–244.

[43] T.M. Butler, K.J. Chaput, J. Alloys Compd. 787 (2019) 606–617.

[44] T.M. Butler, K.J. Chaput, J.R. Dietrich, O.N. Senkov, J. Alloys Compd. 729 (2017) 1004–1019.

[45] J. Gild, Y. Zhang, T. Harrington, S. Jiang, T. Hu, M.C. Quinn, W.M. Mellor, N. Zhou, K. Vecchio, J. Luo, Sci. Rep. 6 (2016) 37946.

[46] J. Gild, J. Braun, K. Kaufmann, E. Marin, T. Harrington, P. Hopkins, K. Vecchio, J. Luo, J. Materiomics (2019).

[47] S. Jiang, T. Hu, J. Gild, N. Zhou, J. Nie, M. Qin, T. Harrington, K. Vecchio, J. Luo, Scr. Mater. 142 (2017) 116–120.

[48] T.J. Harrington, J. Gild, P. Sarker, C. Toher, C.M. Rost, O.F. Dippo, C. McElfresh, K. Kaufmann, E. Marin, L. Borowski, P.E. Hopkins, J. Luo, S. Curtarolo, D.W. Brenner, K.S. Vecchio, Acta Mater. 166 (2019) 271–280.

[49] D.A. Vinnik, E.A. Trofimov, V.E. Zhivulin, O.V. Zaitseva, S.A. Gudkova, A.Yu. Starikov, D.A. Zherebtsov, A.A. Kirsanova, M. Häßner, R. Niewa, Ceram. Int. (2019).

[50] J. Dąbrowa, M. Stygar, A. Mikuła, A. Knapik, K. Mroczka, W. Tejchman, M. Danielewski, M. Martin, Mater. Lett. 216 (2018) 32–36.

[51] A. Sarkar, L. Velasco, D. Wang, Q. Wang, G. Talasila, L. de Biasi, C. Kübel, T. Brezesinski, S.S. Bhattacharya, H. Hahn, B. Breitung, Nat. Commun. 9 (2018) 3400.

[52] A. Sarkar, R. Djenadic, D. Wang, C. Hein, R. Kautenburger, O. Clemens, H. Hahn, J. Eur. Ceram. Soc. (2017).

[53] R. Djenadic, A. Sarkar, O. Clemens, C. Loho, M. Botros, V.S.K. Chakravadhanula, C. Kübel, S.S. Bhattacharya, A.S. Gandhi, H. Hahn, Mater. Res. Lett. 5 (2017) 102–109.

[54] T. Jin, X. Sang, R.R. Unocic, R.T. Kinch, X. Liu, J. Hu, H. Liu, S. Dai, Adv. Mater. 30

(2018) 1707512.

[55] X. Ren, Z. Tian, J. Zhang, J. Wang, Scr. Mater. 168 (2019) 47–50.